AMBIENT TURBULENCE INTENSITY EFFECTS ON THE
CHARACTERISTICS OF WAKE DEVELOPMENT OF A MODEL WIND
TURBINE AND A MATCHED POROUS DISC

A THESIS SUBMITTED TO
THE GRADUATE SCHOOL OF NATURAL AND APPLIED SCIENCES
OF
MIDDLE EAST TECHNICAL UNIVERSITY

BY

BUĞRAHAN ÖZTÜRK

IN PARTIAL FULFILLMENT OF THE REQUIREMENTS
FOR
THE DEGREE OF MASTER OF SCIENCE
IN
AEROSPACE ENGINEERING

SEPTEMBER 2022

Approval of the thesis:

AMBIENT TURBULENCE INTENSITY EFFECTS ON THE CHARACTERISTICS OF WAKE DEVELOPMENT OF A MODEL WIND TURBINE AND A MATCHED POROUS DISC

submitted by **BUĞRAHAN ÖZTÜRK** in partial fulfillment of the requirements for the degree of **Master of Science** in **Aerospace Engineering, Middle East Technical University** by,

Prof. Dr. Halil Kalıpçılar
Dean, Graduate School of **Natural and Applied Sciences** _____

Prof. Dr. Serkan Özgen
Head of the Department, **Aerospace Eng.** _____

Prof. Dr. Oğuz Uzol
Supervisor, **Aerospace Eng., METU** _____

Examining Committee Members:

Asst. Prof. Dr. Mustafa Perçin
Aerospace Eng., METU _____

Prof. Dr. Oğuz Uzol
Aerospace Eng., METU _____

Prof. Dr. İsmail Aydın
Aerospace Eng., METU _____

Assoc. Prof. Dr. Elif Oğuz
Civil Eng., METU _____

Asist. Prof. Dr. Onur Baş
Mechanical Eng., TEDU _____

Date: 01.09.2022

I hereby declare that all information in this document has been obtained and presented in accordance with academic rules and ethical conduct. I also declare that, as required by these rules and conduct, I have fully cited and referenced all material and results that are not original to this work.

Name Last name : Buğrahan Öztürk

Signature :

ABSTRACT

AMBIENT TURBULENCE INTENSITY EFFECTS ON THE CHARACTERISTICS OF WAKE DEVELOPMENT OF A MODEL WIND TURBINE AND A MATCHED POROUS DISC

Öztürk, Buğrahan
Master of Science, Aerospace Engineering
Supervisor : Prof. Dr. Oğuz Uzol

September 2022, 148 pages

This thesis study aims to observe the ambient turbulence intensity effects on the wake development of a model wind turbine and a matched porous disc. Comprehensive wind tunnel experiments are conducted in the wake of the model wind turbine and the porous disc up to 7 diameters downstream through two-dimensional two-component particle velocimetry. The wakes of the model wind turbine and the porous disc are investigated in terms of the mean flow field, turbulence, wake decay, and wake spreading characteristics. Three inflow conditions, namely uniform flow, passive grid flow, and boundary layer flow, are simulated in the test section of the wind tunnel. Furthermore, Proper Otrhagonal Decomposition analysis are carried out to examine the coherent structures of the wake of the both models, whose superposition form the mean wake flow. By comparing uniform inflow with low turbulence intensity and passive grid flow conditions, the findings demonstrate that even when operating at similar, high or low, freestream turbulence intensity levels, the wind turbine's mean wake flow field (both near and far wake) significantly differs from that of the porous disc. In addition,

although the thrust coefficient is the same, the wake of the wind turbine recovers considerably faster than the wake of the porous disc. However, the findings further reveal that the characteristics of the porous disc at high freestream turbulence intensity and the characteristics of the model wind turbine at low freestream turbulence are extremely similar in the far-wake region. This shows that when employing porous discs to replicate wind turbines in wind tunnel research, care should be taken in selecting the ambient turbulence intensity level. Further wake measurements are performed under boundary layer inflow conditions by immersing both models into the boundary layer resulting in different ambient turbulence intensity levels and inflow velocity profiles. Results reveal that the far-wake characteristics of the model wind turbine and the porous disc cease to be comparable as both models are immersed in the boundary layer.

Keywords: Wake, wind turbine, turbulence, porous disc

ÖZ

BİR MODEL RÜZGAR TÜRBİNİ VE UYUMLU BİR GÖZENEKLİ DİSKİN İZ BÖLGESİ GELİŞİMİNİN ÖZELLİKLERİ ÜZERİNE ETKİLERİ

Öztürk, Buğrahan
Yüksek Lisans, Havacılık ve Uzay Mühendisliği
Tez Yöneticisi: Prof. Dr. Oğuz Uzol

Eylül 2022, 148 Sayfa

Bu tez çalışmasının amacı, bir model rüzgar türbini ve uyumlu bir gözenekli diskin iz gelişimi üzerindeki ortam türbülans yoğunluğunun etkilerini gözlemlemektir. Kapsamlı rüzgar tüneli deneyleri, model rüzgar türbini ve gözenekli diskin ardından, iki boyutlu iki bileşenli parçacık hızı ile akış yönünde 7 çapa kadar gerçekleştirilir. Model rüzgar türbini ve gözenekli diskin izleri, ortalama akış alanı, türbülans, iz azalması ve iz yayılma özellikleri açısından incelenmiştir. Rüzgar tünelinin test bölümünde, düzgün akış, pasif şebeke akışı ve sınır tabaka akışı olmak üzere üç giriş koşulu simüle edilmiştir. Tek tip içeri akış ve pasif şebeke akışı koşullarını karşılaştırarak, bulgular, benzer, yüksek veya düşük serbest akış türbülans seviyelerinde çalışırken bile, rüzgar türbininin ortalama iz akış alanının (hem yakın hem de uzak iz) gözenekli olandan önemli ölçüde farklı olduğunu göstermektedir. disc. Ek olarak, itme katsayısı aynı olduğunda, rüzgar türbininin izi, gözenekli discin izinden çok daha hızlı iyileşir. Bununla birlikte, bulgular ayrıca yüksek serbest akış türbülans yoğunluğunda gözenekli diskin özellikleri ile düşük serbest akış türbülansında model rüzgar türbininin özelliklerinin uzak uyanıklık bölgesinde son derece benzer olduğunu ortaya koymaktadır. Bu, rüzgar tüneli araştırmalarında rüzgar türbinlerini kopyalamak için gözenekli diskler kullanılırken, ortam türbülans

yoğunluk seviyesinin seçiminde dikkatli olunması gerektiğini göstermektedir. Daha fazla iz ölçümleri, farklı ortam türbülans yoğunluk seviyeleri ve içeri akış hızı profilleri ile sonuçlanan her iki modelin de sınır tabakasına daldırılmasıyla sınır tabakası içeri akış koşulları altında gerçekleştirilir. Sonuçlar, model rüzgar türbini ve gözenekli diskin uzak uyanıklık özelliklerinin, her iki model de sınır tabakasına daldırıldığı için karşılaştırılabilir olmaktan çıktığını ortaya koymaktadır.

Anahtar Kelimeler: İz bölgesi, rüzgar türbini, türbülans, gözenekli disc

To my parents who made me believe in a better world…

ACKNOWLEDGMENTS

TABLE OF CONTENTS

LIST OF TABLES

LIST OF FIGURES

FIGURES

xx

LIST OF ABBREVIATIONS

ABBREVIATIONS

2D2C PIV	Two-dimensional Two-component Particle Image Velocimetry
ABL	Atmospheric Boundary Layer
AEP	Annual Energy Production
CFD	Computational Fluid Dynamics
FOV	Field of View
HWA	Hotwire Anemometry
IA	Interrogation Area
LES	Large Eddy Simulation
LIDAR	Light Detection and Ranging
Nd: YAG	Neodymium-Doped Yttrium Aluminum Garnet (Nd:$Y_3Al_5O_{12}$)
PIV	Particle Image Velocimetry
POD	Proper Orthogonal Decomposition
RANS	Reynolds Averaged Navier-Stokes
SAR	Satellite Synthetic Aperture Radar
TI	Turbulence Intensity
TKE	Turbulent Kinetic Energy

LIST OF SYMBOLS

SYMBOLS

D	Disc/model wind turbine diameter
h	Spire height (m)
H	Test section height (m)
I_U	Streamwise Turbulence Intensity
$I_{ambient}$	Ambient Turbulence Intensity
I_{wake}	Wake Turbulence Intensity
I_+	Added Turbulence Intensity
k	Turbulent kinetic energy (m^2/s^2)
k^*	Wake growth rate parameter
L	Test section length (m)
N	Number of vector field images
P_{12}	Production of turbulent kinetic energy
$\overline{u'w'}$	Reynolds Averaged Navier-Stokes
U	Satellite Synthetic Aperture Radar
U_∞	Turbulence Intensity
U_{hub}	Turbulent Kinetic Energy
x,y,z	Coordinate system
$\varepsilon_U, \varepsilon_W$	Uncertainty of the mean flow velocity components
$\varepsilon_{\overline{u'^2}}, \varepsilon_{\overline{w'^2}}, \varepsilon_{\overline{u'w'}}$	Uncertainty of the Reynolds stresses
ε_k	Uncertainty of the turbulent kinetic energy
δ	Boundary layer thickness (m)
δ^*	Displacement thickness (m)
θ	Momentum thickness
σ	Standard deviation of the Gaussian velocity profile
ϵ	Initial wake width

Ω Out-of-plane vorticity (s^{-1})

CHAPTER 1

INTRODUCTION

Wind energy has a tremendous potential to consume the gradually increasing demand for energy of the increasing population on the planet and reduce the consequences of energy production using fossil fuels which results in global warming. In this respect, in the last century, rapid growth in wind energy has arisen throughout the world. Since the first wind turbine concept that produces electricity from wind was invested in the United States and the Danish concept which is used to design modern wind turbines proposed in the late 19th century, the wind has become a source of energy production. The total capacity of global onshore and offshore wind farms has reached 743 GW capacity with 93 GW of a new installation by 2020 [1]. Moreover, 557 GW of new capacity is forecasted to be established by 2026 [2].

1.1   Background and Motivation

Wind turbines extract kinetic energy from the freestream flow and induce wakes that are characterized by decreased velocity and higher turbulence intensity. Today, to increase power production and efficiency, wind turbines are accumulated in limited areas in wind farms. Thus, most of the turbines operate in the wake of upwind turbines. As a result, total production of power reduces [3]–[5], and fatigue load on the rotors increases [6], [7] due to unsteady loading for downstream turbines. Thus, it is vital to understand wind turbine wake interactions with the other wind turbines and the ambient in order to improve Annual Energy Production (AEP) and optimize wind farm layout.

Plentiful studies have provided insight into the wake development of wind turbines throughout the years. A vortex sheet originates from the lift distribution on the blades immediate downstream of the wind turbines [8]. Cumulation occurs as a result of the interaction between the vortex structures, resulting in the formation of powerful tip and distinct root vortices behind the rotor [9]. The tip and root vortices rotate in opposite directions due to the conservation of momentum, and tip vortices follow a helical trajectory as they travel within the spinning wake [10]. This tip and root vortex system is unstable, and it breaks down into small-scale turbulent structures due to numerous instability phenomena [8]. In addition, due to the velocity differences, a shear layer forms and separates the wake and the free stream flow, and the shear layer thickens as flow develops. When the shear layer reaches the center of the wake, the period of increasing turbulence ceases, and the turbulence evolution is characterized by turbulence decay in the following area. Due to the formation of the turbulent eddies in the shear layer, turbulence intensity increases especially at the top part of the wake, and the momentum transfer process so-called entrainment occurs when the wake turbulence mixes the free stream velocity with the wake velocity, which is slower. [11]. The rate at which the wake expands as a result of this transfer of momentum is ruled by the ambient turbulence.

The wake downstream of a wind turbine can be split into two downstream regions near-wake and far-wake [12]. Figure 1.1 illustrates a schematic of both regions in the vicinity of the wind turbine.
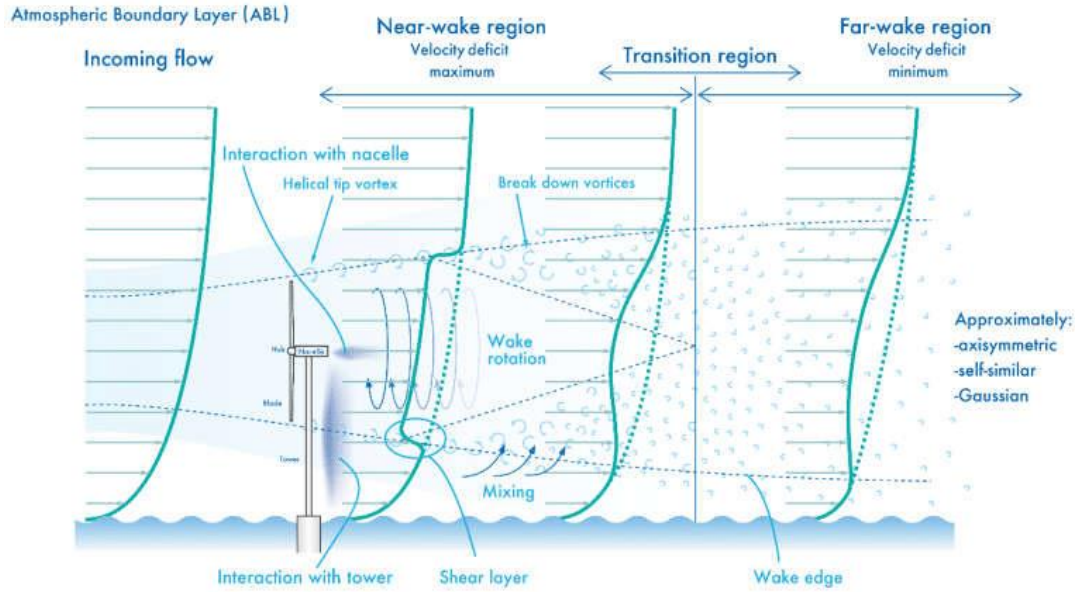
Figure 1.1. Schematic of wake expansion in the vicinity of a wind turbine [13]

The near-wake can be characterized by high-velocity deficit, pressure drop, and increased turbulence intensity [10]. The near-wake starts directly downstream of the turbine and extends to between 2 and 4 diameters distance [14]. In this region, the geometry of the wind turbine, the blade profiles, and the rotation effects have a strong influence on the wake. The tip and root vortex system is the dominant feature of the wake, and it slows down the entrainment process as it keeps stable [15]. Velocity deficit increases up to the downstream position of the wind turbine where wake recovery starts. The recovery rate of the wake is dependent on the ambient turbulence intensity level [16]. Furthermore, turbulence intensity downstream increase sharply and is explained using the notion of added turbulence, in which wake turbulence is defined as a superposition of turbulence induced by the wind turbine and turbulence in the incoming flow [12].

The effect of wind turbine geometry gets reduced in the far-wake region and starts after the breakdown of the tip vortices. In this region, the two fundamental processes that determine flow development occur, namely convection and turbulent diffusion [14]. Turbulence becomes the dominant factor, and turbulence mixing increases;

therefore, wake recovery accelerates [16] and overall turbulence intensity decreases [10]. Far downstream, the velocity deficit becomes axisymmetric and self-similar and can be approximated by the Gaussian shape function.

Porous discs are the experimental counterpart of the actuator disc models employed to reproduce the wake development characteristics of wind turbines in wind tunnel studies [17]–[20]. In addition to the easiness of manufacturing and fewer operating efforts, these non-rotating rotor models provide significant simplifications by not considering exact wind turbine and rotor geometry [21]. However, there are several limitations to using porous discs in experimental studies. First of all, only the far wake characteristics can be reproduced due to the fact that the absence of the rotational motion has crucial effects on the near-wake development as beforementioned. Secondly, exact wake development aspects of the wind turbine should be obtained to design a matching porous disc [17], [21], [22].

Wake development downstream a wind turbine and a porous disc have significant differences. Individual jet flows through porous parts occur and the porous disc functions like a passive turbulence grid. Hence, turbulent mixing immediately starts downstream of the porous disc which corresponds to the near-wake region, where highly turbulent separation occurs since the absence of tip vortices; thus, wake recovery occurs faster [17]–[20]. On the other hand, far wake characteristics can be comparable to that of the wind turbine after the breakdown of the tip vortices [12].

1.2   Literature Survey

This part presents a detailed literature survey of wind turbine wake studies which mainly focus on wind turbine wake and atmospheric boundary layer (ABL) interactions and the effects of the ambient turbulence intensity level on wake development. Furthermore, the following literature survey is categorized as wind turbine wake measurements and analytical wake model studies. The wind turbine

wake measurement part is further divided into subsections of the field measurements, numerical studies, and wind tunnel experiments.

1.2.1   Measurement of Wind Turbine Wake

1.2.1.1   Field Measurements

In recent years, remote sensing technologies have been employed to examine the impacts of inflow conditions on the form and kinetics of the flow surrounding wind turbines and wind farms, also to obtain helpful data for validating analytical models [23]. For instance, Barthelmie et al. [3]–[5] investigated the effects of meteorological conditions on the Vindeby offshore wind farm. Wind shear, diurnal variability, turbulence intensity, atmospheric stability, and wind speed have all been investigated to understand how they affect wake losses, energy production, and turbine loading. These findings are used to develop the knowledge of both the stand-alone wind turbine and wind farm wake development, and wake models.

Fuertes et al. [24] investigated wind turbine wake evaluation of 2.5 MW wind turbines using two nacelle-mounted pulsed scanning Doppler lidars to measure the growth rate of the wake, the expansion of the near and far wake, and the velocity deficit. Results indicate that higher inflow turbulence intensity resulted in shorter near-wake lengths and faster wake recovery. Iungo et al. [25] also used Doppler lidar to obtain both axial and vertical velocity profiles downstream of the 2 MW wind turbine. For both velocity components, flow quantities were analyzed throughout the sample set, and they revealed considerable flow variations in the near-wake region at the turbine top tip height, with a turbulence intensity of roughly 30%. Moreover, Bardal et al. [26] used lidar to investigate the power curve of a 3 MW onshore wind turbine. Results reveal that low shear and turbulence preconditions have the greatest impact, resulting in a 1.2% increase in AEP relative to the average at this site.

Christiansen and Hasager [27] and Hasager et al. [28] used satellite synthetic aperture radar (SAR) data to evaluate the wake impacts from two big offshore wind farms in the North Sea, namely Horns Rev and Nysted. Their results indicate an 8-9 percent velocity deficit downstream of the wind turbine arrays, with a 2 percent wind speed recovery over a distance of 5-20 km when turbulence severity is increased.

1.2.1.2   Numerical Studies

Aside from field experiments, numerical simulations are widely used to understand the aspects of wind turbine wake and became more popular in the near past after significant advances occurred in computer processing. Computational fluid dynamics (CFD) tools tuned by experimental data have been used widely, especially in simulating wind farms. There are two computational fluid dynamics approaches to model a wind turbine in numerical simulations: the direct modeling approach and the generalized actuator disc approach [10]. The direct modeling approach resolves whole rotor geometry by volume grid and simulates the motion of the rotor and boundary layer flow, thus it resolves flow structures accurately in the wind turbine wakes. Numerous direct modeling studies are performed mostly using time or space-filtered equations, RANS and LES respectively [29]. For instance, Sedaghatizadeh et al. [30] and Zhou et al. [6] performed direct modeling simulations using LES, and more studies are performed by Sorensen et al. [9], Regodeseves and Morrosc [31], Cai et al. [32], Miao et al. [33], Wilson et al. [34] and Stergiannis et al. [35] using RANS models. Results reveal that LES has superiority over RANS models accounting for single wind turbine simulations regarding wake velocity deficit predictions, added turbulence, and turbulent kinetic energy production in comparison with experimental results. However, the computational cost of LES simulations is two orders higher than that of RANS simulations [10].

In the generalized actuator disc approach effects of blades are accounted for and distributed over the rotor area. There are three types of actuator disc models based

6

on parametrization techniques, namely the actuator disc model, the actuator line model, and the actuator surface model [36].

Porté-Agel et al. [37] investigated wind turbine wakes within ABL through LES coupled with three numerical rotor models: the actuator disc model with no rotation, the actuator disc model with rotation, and the actuator line model. Results indicate that all three models give accurate results, especially in the far wake, whereas wind turbine models that generate wake flow rotation have superiority in the near-wake region in comparison with experimental results obtained downstream of a miniature three-blade wind turbine.

Lu and Porté-Agel combined LES with the actuator line approach to examine the expansion of the wind turbine wake within the stable boundary layer. Authors claim that three-dimensional LES methods combined with an actuator line model are capable of quantitively simulating wind turbine wakes and their consequences on turbulent fluxes in a wind farm. Furthermore, Wu and Porté-Agel [38]–[40] performed a series of numerical studies to examine the aspects of wind turbine wake through LES coupled with two numerical wind turbine models, namely the standard actuator disc model and actuator disc model with rotation proposed by the authors. For instance, Wu and Porté-Agel [38] simulated the wake behind a wind turbine in a neutral turbulent boundary layer flow and compared the numerical results with an experimental study of the wake properties of a miniature wind turbine. Results show the superiority of actuator disc model with rotation over the standard model in the near-wake region in terms of simulating turbine-induced flow. In addition, simulation results obtained with both models are confirming to experimental results in the far-wake region, and the LES framework is able to simulate wind turbine wake characteristics. Wu and Porté-Agel [39] analyzed turbulent flow interactions in a wind farm with different layouts, namely staggered and aligned. Using an actuator disc with rotation model resulted in an improved prediction of wake characteristics regarding experimental results. Moreover, results reveal that stagger layout in wind farms has advantages in obtaining a more homogenous wind farm wake along the

spanwise direction which accelerates the wake recovery. The same LES framework was further tested by Wu and Porté-Agel [40] to simulate Horns Rev Offshore wind farm with a further enhanced actuator disc model with rotation. Results indicate that wind farm power prediction using the new wind turbine model is more realistic compared to that obtained through the standard actuator disc model. Moreover, Abkar and Porté-Agel [41] investigated atmospheric stability effects on wind turbine wake operating under neutral, convective, and stable conditions with this LES framework. Results demonstrate atmospheric thermal stability influences on wind turbine wake in terms of wake characteristics. In addition, it has been proven that wind turbine rate of wake recovery is higher under convective conditions.

Ivanell et al. [42] employed LES to simulate Horns Rev offshore wind farm through an actuator disc with different angular alignments between -15 to 15 degrees for wind turbine modeling. It is indicated that the main power production predicted from the simulation is in fairly good agreement with the measurements.

Troldborg [43] employed LES and to simulate the Tjaereborg wind turbine wake in four distinct cases with changing tip speed ratios in uniform inflow. Results show good agreement in the near-wake region compared with the field measurements in terms of wake deficit and added turbulence intensity. Results also show that the distance downstream wind turbine where the tip and root vortices are unstable increases as the tip speed ratio increases. Similarly, Troldborg et al. [44] used LES coupled with the actuator line method as a wind turbine model to examine wind turbine wake in a neutrally stratified atmospheric boundary layer. Results show good agreement with field measurements. Troldborg et al. [45] conducted a numerical study to simulate the wind turbine wake of an NREL 5MW wind turbine through three wind turbine models, namely actuator disc, actuator line, and fully-resolved rotor model, under laminar and turbulent inflow conditions. Results reveal that all three models are applicable up to four diameters downstream in uniform inflow, whereas the actuator disc and the actuator line models show discrepancies in terms of wake deficit, added turbulence intensity, and turbulence kinetic energy predictions

further downstream. These differences reduce and predictions of the actuator disc and the actuator line models improve in turbulent inflow.

Cabezon et al. [46] performed a numerical study to compare turbulence models in a simulation of the wake of a wind turbine used in the Sexbierum experiment. They used an actuator disc model in order to model the wind turbine. Wind speed deficit, added turbulence intensity, and shear stress predictions are compared in consideration of the Sexbierum experiment. Results show that although applying corrections on dissipation term improves prediction in the wake of the wind turbine, it is inadequate to get as accurate predictions as LES results.

Calaf et al. [47] conducted a numerical study to evaluate the momentum flux and kinetic energy in the boundary layer in the vertical direction of the fully developed wind turbine array boundary layer. They used LES with the original actuator disc method and assumed that changes in flow quantities in streamwise direction are negligible. The vertical kinetic energy flux has been proven to attribute to the power harvested by wind turbines.

1.2.1.3 Wind Tunnel Studies

Although natural variations in the atmospheric boundary layer and real-scale wind turbine wake development can be observed in field measurements, inflow conditions frequently change during experiments, and due to large measurement volumes, it is very likely to obtain measured data with low spatial and temporal resolution. Moreover, numerical simulations are either too simplified to obtain close results to the real case or computationally over-expensive. Thus, wind tunnel experiments in controlled environments are the reasonable option to understand the wind turbine wake development.

Numerous comprehensive wind tunnel applications have been carried out to examine the airflow around the turbine at different inflow conditions [23]. In controlled

environments, the effects of ambient turbulence intensity level and wind shear on the performance and wake formation of the wind turbines and wind farms are investigated. For instance, Sicot et al. [48] performed wind tunnel experiments to study inflow turbulence level effects on wind turbine aerodynamics in terms of power and thrust. Experiments are conducted in three inflow turbulence levels, namely 4.4%, 9%, and 12%, which are obtained using a passive turbulence grid. Results show that inflow turbulence level does not have a major effect on wind turbine power and thrust.

Chamorro and Porté-Agel [49] conducted wind tunnel experiments to investigate the boundary layer flow effect under two conditions, which are neutral and stably stratified conditions. Model wind turbine wake turbulence statistics are examined via triple-wire that allows measuring velocity and temperature. Results show that turbulence statistics are affected by model wind turbine wake up to 20 diameters distance downstream. In addition, in contrast to turbulence intensity where it is maximum at the tip locations, velocity deficit has an axisymmetric shape. Thus, the Gaussian distribution can be used to approximate the velocity distribution. This velocity distribution downstream decelerates more rapidly in stable stratified cases. Similarly, Zhang et al. [50] experimentally studied convective and neutral boundary layer effects on wind turbine wake. Results show a small velocity deficit and more advanced turbulence intensity at the top-tip level and the lower part of the wake in the convective boundary layer, compared to the neutral case.

Chamorro et al. [51] experimentally investigated the Reynolds number dependence on wind turbine wake characteristics. Cross-wire anemometer is used to obtain velocity components. Experiments are conducted in six Reynolds numbers varying more than one order of magnitude. Results reveal that near-wake characteristics are highly affected by Reynolds number due to stronger effects of the presence of airfoils and rotation, while it is not the case for the far-wake.

Cal et al. [52] conducted experimental studies on the boundary layer of a wind farm modeling with an array of 3x3 model wind turbines. Average velocity and Reynolds shear stress distributions are measured and calculated in horizontal planes via Particle Image Velocimetry (PIV) and compared with momentum theory. Results demonstrate the importance of turbulence on vertical kinetic energy transportation.

Maeda et al. [53] investigated flow characteristics downstream of a model wind turbine, where averaged velocity and turbulence intensity profile of interest, under different ambient turbulence intensity conditions using hot-wire anemometer. They generated two different ambient turbulence intensity levels using two types of passive grids to alter inflow turbulence intensity in the test section. Results demonstrate that wind turbine wake recovers faster in high ambient turbulence levels.

Mikkelsen [11] conducted wind tunnel experiments to examine the influences of inflow turbulence intensity level on the performance and wake development of a model wind turbine. Results show that the power coefficient is 2.4% lower under turbulent inflow conditions. Further results obtained by hot-wire anemometer at the wake of the model wind turbine show that, at $x/D=1$, velocity deficit under both low and high inflow turbulence levels are identical which is associated with the thrust coefficient which is similar in both conditions. However, velocity deficit recovers faster under turbulent inflow conditions further downstream of the model wind turbine. Moreover, it is shown that velocity distribution can be represented by Gaussian distribution in the far wake. A similar study is performed by Al-Abadi et al. [54]. Results show that increasing inflow turbulence increases the performance of the wind turbine since high turbulence helps to dampen the tip vortices and deduce more energy to the wind turbine wake by increasing the wake-surrounding interaction.

Jin [55] investigated the effects of inflow turbulence on wind turbine wake in terms of integral length scale evolution and large-scale motion associated with inflow

conditions. Measurements are conducted using hot-wire anemometer under two inflow conditions generated by an active-grid system integrated into a wind tunnel: low turbulence level (0.2%) and high turbulence level (11.5%). Results demonstrate that wake recovery is accelerated under high turbulence conditions while integral scales grow linearly independent of inflow turbulence level. Talavera and Shu [56] performed a similar experimental study to examine a single wind turbine wake along with an array of two turbines using 2D-PIV. Results show that increasing inflow turbulence increases the performance of the turbines in both single and tandem cases since the reducing impact of the turbulence intensity level on the separation of the blade.

Porous discs, simplified wind turbine models, are experimental tools adapted from the actuator disc concept which started used in wind tunnel studies with a pioneering study by Vermeulen and Builtjes [57]. Authors claim that velocity and turbulence intensity distributions can be simulated similarly to rotor models after a certain downstream location. Further experimental studies using the porous disc approach to characterize model wind turbine wake structures are conducted by Aubrun et al. [17]. They carried out a series of comparative experiments that investigate the wake development properties of a porous disc and a model wind turbine with three blades under two inflow conditions with different turbulence levels, namely decaying isotropic turbulent inflow and neutral atmospheric boundary layer, 4%, and 13%, respectively. Flow properties are measured using hot-wire anemometry at x/D=0.5 and x/D=3. Results show that near-wake structures of the rotor model are not able to be simulated using the porous disc in the near-wake due to the absence of the rotational effects of the blades such as rotational momentum and vortices. However, high-order velocity statistics and pressure distributions of porous disc wake are fairly similar to that of model wind turbines after x/D=3 under turbulent inflow conditions.

Lignarolo et al. [18] performed an experimental study to compare the aspects of a two-bladed model wind turbine and a porous disc with the same diameter and thrust coefficient in the near-wake region. Experiments are conducted under uniform

inflow with low turbulence in order to eliminate wake-induced mixing characteristics that provide easiness for comparing near-wake structures. Higher-order velocity statistics and pressure distribution are measured via S-PIV. Results reveal that both models have similar wake expansion and energy reduction in near-wake so that they have the same total axial force associated with the pressure field. On the other hand, significant differences can be observed at the blade root and tip locations due to rotational effects, thus turbulence intensity level at the model wind turbine near-wake is quite larger (~50%) compared to that of the porous disc. The results further demonstrate that different turbulence mixing phenomena are valid for both cases.

Camp and Cal [19] performed a wind tunnel study to investigate the similarities in terms of mean kinetic energy transport inside the wind farm by examining the wake of the center model in the last row of a 4x3 array via S-PIV. Results demonstrate that porous discs can be adopted to reproduce the far-wake characteristics of wind turbines while significant differences occur in the near-wake due to the absence of the blades.

Neunaber [20] experimentally studied the wake development downstream of the model wind turbine and a matched porous disc and compared the characteristics under different inflow conditions with varying ambient turbulence intensity levels. One and two-point statistics are used to investigate the data and differences in wake development are obtained by means of the evolution of turbulence intensity. Results reveal that inflow conditions have minimal to no influence on the far wake characteristics of both the wind turbine and the porous disc.

Helvig et al. [58] performed wind tunnel experiments to compare the near-wake characteristics of a lab-scale wind turbine and porous discs with different designs and solidities, and the same diameters as the model wind turbine. Results show that, regarding the mean velocity field, vorticity, and turbulence, the porous disc design

which has roughly the same drag coefficient as the wind turbine is able to reproduce the closest near-wake characteristics of the wind turbine.

1.2.2 Analytical Studies

Analytical wake models have extensively used tools due to their simplicity and high efficiency, especially in wind farm layout and control optimization, and are based on wind turbine far-wake characteristics that assume axisymmetrical and self-similar velocity deficit and turbulence intensity [12], [14]. A pioneering analytical wake model is proposed by Jensen [59] in 1983. Jensen assumes that wake velocity deficit with top-hat shape expands linearly and is further improved by Katic [60] regarding wind turbine characteristics. Top-hat shape assumption is also used in another analytical wake model proposed by Frandsen et al. [61] where conservation of mass and momentum are grounded. Frandsen model differs by wake diameter and wakes expansion rate assumptions from the Jensen model. The pioneering Gaussian-shaped wake model is developed by Larsen [62] in 1988 and improved by himself in 2009 [63] in which boundary conditions are obtained experimentally. Larsen models are grounded on the Prandtl turbulent boundary layer equations. Ishihara et al. [64] proposed a wake model that includes turbulence intensity as a variable in analytical wake modeling. In addition, Bastankhah and Porté-Agel [65] developed a Gaussian-shaped wake model based on mass and momentum conservation. Another wake model is proposed by Ishihara and Qian [64] with an improved wake growth rate formulation in which thrust coefficient, as well as ambient turbulence intensity, are utilized. Gao et al. [66] introduced a model which uses a Gaussian wake shape and is based on the Jensen model. The model also contains a novel turbulence intensity model that accounts for ambient and rotor-added turbulence intensity.

In the literature, there are various comparative studies that validate analytical wake models with wind tunnel experiments and field measurements. For instance, Göçmen et al. [67] employed six wake models, namely Jensen, Larsen, DWM, FUGA, LES,

and RANS, which are developed at the Technical University of Denmark. Data from Sexberium on-shore and Lillgrund off-shore wind farms were employed to check the capabilities of the analytical models. Although results show that wake models' performance varies in both wind farms, the Jensen, the Larsen, and FUGA models are in fairly good agreement with measurements both in on-shore and off-shore wind farms. Sorensen et al. [9] compared analytical predictions of three models (Jensen, Larsen, and Eddy Viscosity Model) at Horns Rev 1 offshore wind farm. Results reveal the superiority of the Jensen wake model with a 0.04 wake decay coefficient. Polster [68] performed an experimental study and employed six wake models for single wind turbine and wind turbines in tandem with changing blade pitch angles. Results show that there is not a single analytical wake model that is quite accurate for all cases.

1.3 Thesis Objective and Outline

This thesis study aims to investigate the similarities and differences between the wake development of an isolated model wind turbine and a matched porous disc under different freestream flow conditions, namely uniform flow with low turbulence intensity, passive turbulence grid flow, and boundary layer flow. Effects of ambient turbulence intensity are examined in the wake of both the model wind turbine and the porous disc through mean flow, turbulence, wake decay, and wake spreading characteristics through two-dimensional two-component particle image velocimetry (2D2C PIV) analysis. In addition, Proper Orthogonal Decomposition analysis is performed to investigate and compare the origin of the coherent structures downstream of both models under different inflow conditions.

Measurement facilities and details as well as the model wind turbine and the porous disc are presented in Chapter 3. Results and discussions of the uniform inflow and turbulence grid cases are introduced in Chapter 4. In addition, Chapter 5 presents the

results and discussions of the boundary layer inflow case. The conclusion is presented in Chapter 6.

CHAPTER 2

EXPERIMENTAL SETUP

This chapter presents the experimental setup and measurement details of the present study to compare the wake development characteristics of both models. First, the wind tunnel facility and design details of the model wind turbine and the porous disc are introduced, and then experimental details and setups to conduct wake studies are described.

2.1   Wind Tunnel Facility

The wind tunnel facility utilized for the experiments, which can be seen in figure 2.1, is an open-return suction type wind tunnel at METU Center for Wind Energy Research (METUWIND). This wind tunnel has an 8 m long test section composed of plexiglass walls with a cross-section of 1x1 m^2, a settling chamber and a contraction cone with a contraction ratio of 5:1. A 1.2 m diameter axial fan impelled by a 45-kW electric motor is used to move the air through the tunnel. The maximum inflow velocity and turbulence intensity at the inlet of the test section (i.e., without turbulence grid) is around 25 m/s and less than 0.35 %, respectively. An interchangeable passive turbulence grid can be placed between the contraction and the inlet of the test section by sliding from the side wall of the wind tunnel. Reynolds number in the test section is provided through a close-loop control system that drives the wind tunnel.

Figure 2.1. The open-return suction type boundary layer wind tunnel is utilized for the wake measurements.

2.2 Wind Turbine Models

The model wind turbine and the porous disc (Figure 2.2) utilized in the present study are comparable to those used in Camp and Cal [19]. The cross-section of the model wind turbine is linearly tapered, with a twist angle of 22º at the root and 15º at the tip. The model wind turbine blades are manufactured using a 0.5 mm aluminum sheet by cutting and pressing in a die to give the desired twist distribution and taper along the profile. The model wind turbine is powered by a DC brushless mini motor which is integrated inside the nacelle to control the rotational speed. Nacelle and hub are fabricated using 3D printing technology with PLA+ filament. The porous disc has the same diameter and similar thrust coefficient as the model wind turbine, 0.12 m and 0.6, respectively. In addition, the porous disc is cut from plywood via laser and has non-uniform porosity in the radial direction in order to duplicate the wind turbine design. Table 2.1 illustrates the design properties of the model wind turbine and the porous disc.

Figure 2.2. Models used in wake measurements: the model wind turbine (left) and the porous disc (right).

Table 2.1 Design aspects of the model wind turbine and the porous disc

Properties	*Model Wind Turbine*	*Porous Disc*
Diameter	120 mm	
Hub Diameter	10.2 mm	10.8 mm
Twist Angle	22º at root, 15º at the tip	-
Taper Distribution	Linear	-
Porosity	-	Non-uniform
Material	Aluminum	Plywood
Disc thickness	-	3.2 mm
Mast diameter	10 mm	
Mast property	Smooth shaft	
Blockage	1.15 %	

2.3   PIV Setup

Two-dimension two-component (2D2C) PIV system used in wake measurements has a New Solo PIV Nd: YAG laser, Phantom v641 high-speed camera with a Nikon-Nikkor 60 mm lens, a Dantec Dynamics timer box, Dynamic Studio data acquisition, and analysis software. To make measuring easier while traversing downstream the model wind turbine/porous disc, the parts of the PIV system (the laser, optics, and camera) are mounted on a three-axis traverse mechanism which traverses in one dimension of 0.6 m. A SAFEX fog generator is used to seed the flow with frog droplets of 1 μm in diameter. Table 2.2 summarizes the components used in the 2D2C PIV setup.

Table 2.2 2D2C PIV components used in wake measurements

Laser Sheet	Laser type	Nd: YAG
	Manufacturer	New Wave Research
	Model	Solo 120XT
	Maximum energy	120mJ/pulse
	Wavelength	532 nm
	Thickness	≈2 mm
Optics	Mirrors	Dielectric Mirror, 532 nm
	Spherical Lens	
	Cylindrical Lens	Plano-convex, 750 mm FL
		Plano-concave, -12.4 mm FL
Camera	Sensor type	CMOS
	Sensor resolution	$2560 \times 1600 \ pixel^2$
	Sensor size	$25.6 \times 16.0 \ mm^2$
	Pixel pitch (size)	10 μm
	Depth	12 bits
	Maximum repetition rate	1400 fps @ Full resolution
	Internal memory buffer	2500 fps @ 1920×1080
		16 GB
Camera Lens	Manufacturer	Nikon
	Focal length	60 mm
	f# (aperture)	2.8
Seeding	Type	Fog
	Nominal diameter	≈ 1 μm
	Seeding generator	Safex Fog generator

2.4   Experiment Details

Wake development of both models is examined under different inflow conditions in order to observe the effect of the ambient turbulence intensity level. For the first experiment campaign, both models are operated in a uniform inflow with low turbulence intensity (without a passive turbulence grid at the inlet of the test section) and the results are compared with the findings obtained under the passive turbulence grid inflow case, in which the free stream flow is considered homogenous and isotropic. Furthermore, for the second campaign, both models are immersed into the boundary layer created by using spires at the inlet of the test section. Setups and facilities are checked before experiments to be sure to have same conditions. In addition, experiments for all cases are repeated three times to ensure the validity of the results. Details regarding experiments and setup are explained in detail hereafter.

2.4.1   Uniform Inflow and Passive Grid Turbulence Case

2.4.1.1   Background of Grid Turbulence

Homogenous isotropic turbulence can be approximated using regular passive turbulence grids in wind tunnel studies. Regular turbulence grids are inexpensive and intuitive tools composed of mesh grids placed at the wind tunnels. Flow downstream of the passive grids can be divided into two regions as the near-wake and the far-wake regions. In the near-wake region, boundary conditions dominate the flow as a result of individual bar wakes; on the other hand, turbulence decay is the dominating characteristic in the far-wake region [69], [70].

The induced vortices downstream of the bars generate grid turbulence. After flow reaches a certain downstream position, flow transforms into a homogenous and isotropic turbulent flow, characterized by slow rotating vortices that roughly scale to the size of the grid bars [71]. Corrsin [72] introduced two conditions to obtain a homogenous region downstream of the passive grid. First, it is suggested that the

cross-section of the tunnel should be equal to or greater than the mesh size, and a homogenous region occurs after x/M ≥ 40 where x is the downstream distance of the passive grid and M is the mesh length.

In grid turbulence, the decay of the energy can be fitted in power law and shown as [73]

$$\frac{k}{U_0^2} \sim (x - x_0)^{-n} \qquad (2.1)$$

where U_0 is mean velocity and n is power coefficient.

Taylor [74] conducted an experimental study downstream of a passive grid and fit the decay of the energy into power low with n = -1. Comte-Bellot and Corrsin [75] conducted extensive experiments using multiple passive grids. They revealed that n is highly influenced by the grid geometry and grid Reynolds number and varies in a range of -1.2 ≥ n ≥ -1.3. By characterizing the wake of the passive grids in numerous studies [69], [76], [77], it is proven to be n value varies in the range of -1 ≥ n ≥ -1.4.

Turbulence intensity also can be fitted into power law and expressed as

$$I^2 = A(\frac{x - x_0}{M})^{-n} \qquad (2.2)$$

where A is a constant, M is the mesh size of the grid and n is the decay exponent. Baines and Peterson [78], Vickery [79] as well as Roach [80] set the decay exponent as -5/7, while Laneville [81] proposed an exponent value of -8/9.

Roach [80] performed a comprehensive experimental study and investigated wake development characteristics of passive turbulence grids with various designs and layouts. He classified the differences in the turbulent characteristics of the passive grid wakes and obtained empirical relations to derive design guidelines. Results demonstrate that turbulence intensity in the wake of the passive grid decays along downstream distance with the power of -5/7 (i.e. $x^{-5/7}$). In addition, eddy lengths

23

are independent of the type of passive grid. On the other hand, passive grids composed of circular bars and wires are Reynolds number dependent while Reynolds number dependency does not occur with square/rectangular bar grids and perforated plates. In addition, Bearman and Morel [82] investigated the wake characteristics of four different passive grids experimentally. Results show that the wake patterns of the circular bars are highly influenced by the Reynolds number and roughness of the bars. Moreover, the wakes of the blunt bodies are characterized by separation at the sharp corners. Furthermore, Nakamura et al. [83] showed that trimming the edges of the square and rectangular-shaped bars has a minor effect on the characteristics of the turbulence of the wake of the passive grid.

2.4.1.1.1 Passive Turbulence Grid Design Methodology

The passive turbulence grid with squared meshes used in experiments is designed based on empirical relations obtained by Roach [80]. Figure 2.3 shows the dimensions of the grid design and related grid porosity calculation can be seen in equation (2.3).
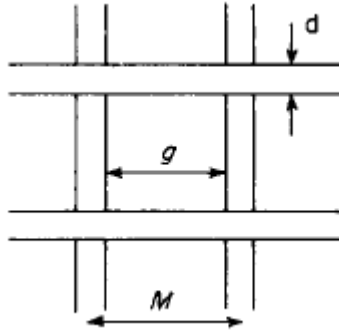
Figure 2.3. Sketch of the passive grid turbulence with squared mesh and its dimensions used in the design process [80]

$$\beta = (1 - \frac{d}{M})^2 \tag{2.3}$$

Turbulence intensities downstream of the passive turbulence grid are approximated through the following equations by Roach [80].

$$I_U = 1.13\left(\frac{x}{d}\right)^{-5/7} \qquad (2.4)$$

$$I_V = (1.13)(0.89)\left(\frac{x}{d}\right)^{-5/7} \qquad (2.5)$$

2.4.1.2 Experimental Setup and Details

The free stream Reynolds number is fixed to 100,000 based on the free stream velocity and the model wind turbine/porous disc diameter for all cases. Two free stream turbulence levels, namely 0.5% and 4.5%, are generated in the wind tunnel test section at the hub height location of both the model wind turbine and the porous disc for uniform inflow and passive turbulence grid case experiments. The higher turbulence intensity level is provided by installing a passive turbulence grid explained in depth before in Chapter 2 between the contraction and wind tunnel test section inlet (see figure 2.4 and figure 2.5). Using hotwire data obtained at the model position for 30 seconds at a sampling rate of 10 kHz, the integral length scale is computed to be roughly 0.071 m.

The wind turbine models are placed 6 m downstream of the test section inlet and in the middle of the test section (0.5 m from the bottom and side wall). To exclude the effect of the tower on the PIV images, the turbine/disc is entered from the side wall. A sketch of the measurement setup can be seen in figure 2.4. The reference for the wake measurements is the (x, y, z) coordinate system, of which the origin is set to the turbine/disc hub center.
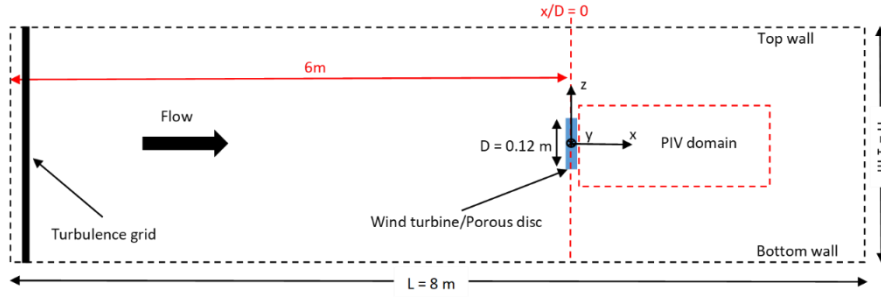
Figure 2.4. Sketch of the test section and the measurement setup of the grid turbulence case

Using an ATI Gamma Force/Torque sensor, a series of load measurements are performed to match the model wind turbine's thrust coefficient to the that of the porous disc by using following relation.

$$C_T = \frac{T}{\frac{1}{2}\rho U_\infty^2 A} \qquad (2.6)$$

where T is axial force applied by the flow to the models, ρ is air density, U_∞ is free stream velocity and A is model surface area. First of all, the thrust coefficients of the porous disc under different inflow turbulence intensity levels are calculated. Subsequently, by varying the rotational speed of the rotor, the thrust coefficient of both models is matched under the same inflow conditions. Results for two inflow turbulence intensity levels of interest are presented in table 2.3. To achieve the necessary thrust coefficient illustrated below, the model wind turbine is driven at a constant speed of 4250 rpm, equivalent to a tip speed ratio around 2.

Table 2.3 Thrust coefficients for different test cases

Test Cases	Thrust Coefficient (C_T)
Wind Turbine-no grid (WT-ng)	0.6
Wind Turbine-grid (WT-g)	0.6
Porous Disc-no grid (PD-Ng)	0.62
Porous Disc-grid (PD-g)	0.59

Double-frame particle images are pre-processed with a low-pass filter to advance the image quality and substitute background noise. The generated vector maps are then subjected to three-step adaptive correlation analysis with a final interrogation window size of 32x32 pixels^2 and 50% overlap, and a vector spacing of 1.58 mm is obtained.
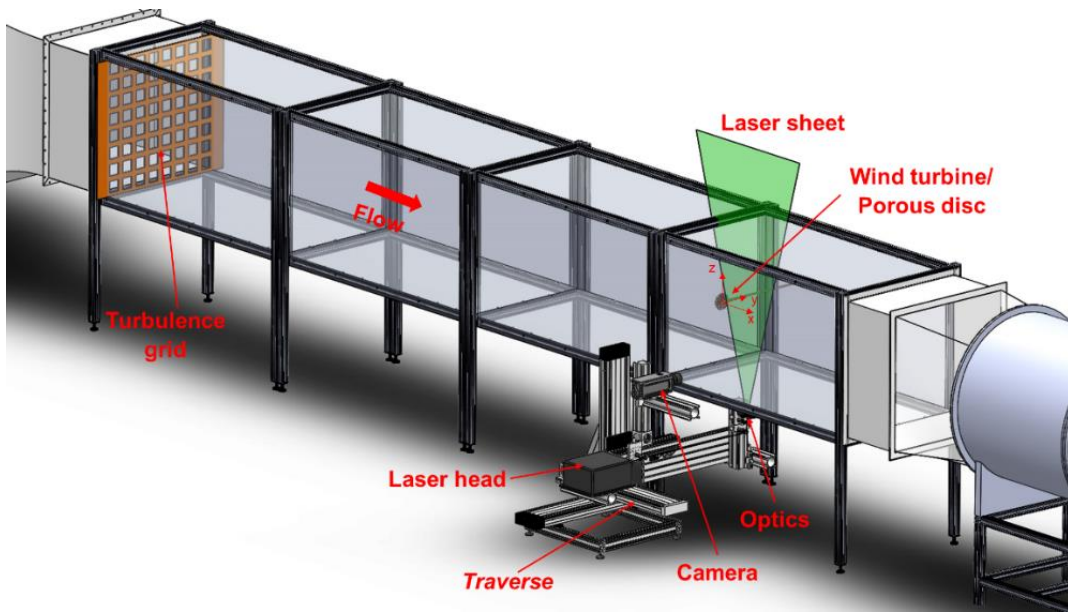
Figure 2.5. PIV setup employed in wake measurements

The wake measurements are performed in a range of $0.5 \leq x/D \leq 7.0$ downstream of the model wind turbine and the porous disc. Figure 2.6 illustrates the multiple PIV measurement windows which are combined to obtain the total vector field. The positions of the field of view are illustrated as rectangular shapes in the x-z plane using the coordinate system mentioned before. The grey-colored fields depict the 0.12D (%10) overlap region of two adjacent fields of views (FOVs), which corresponds to about 10 vectors. The area of each field of view (FOV) is 186 x 296 mm2 (1.55D x 2.47D) along the streamwise and the vertical directions, respectively.

The model wind turbine and the porous disc location are shown as a blue rectangle with an exaggerated thickness for the sake of clarity.

The total averaged vector field is obtained by stitching and averaging 1000 image pairs for each field of view to assure statistical convergence for each case. While taking image pairs of the wake field, the time between two pulses is used at 80 μs and the acquisition frequency is set at 10 Hz.
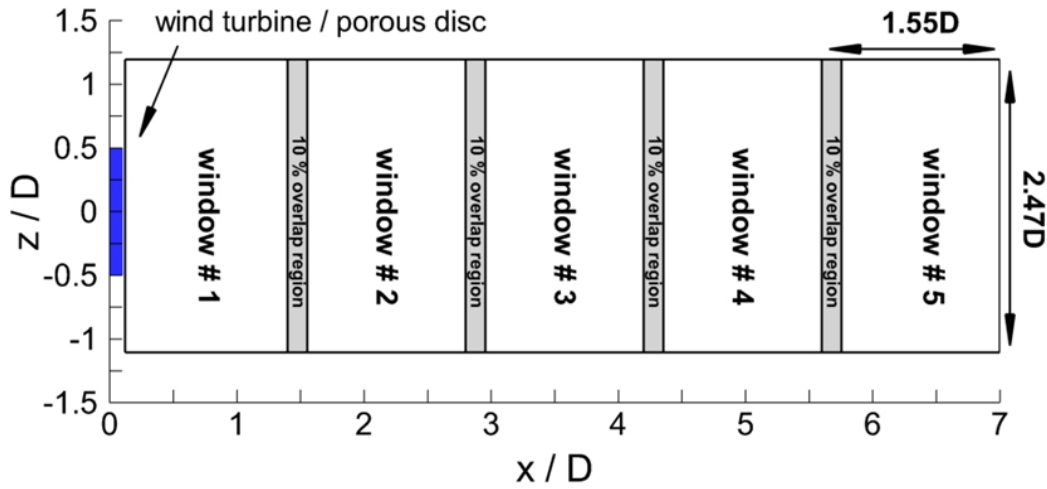
Figure 2.6. PIV measurement domain in the flow field shows the field of view dimensions and the overlap regions. The blue rectangular region represents the wind turbine/porous disc located between $-0.5 \leq z/D \leq 0.5$

2.4.2   Boundary Layer Inflow Case

2.4.2.1   Background of Atmospheric Boundary Layer

As a result of unequal heating by solar radiation, pressure variations over the earth's surface led to global winds. Moreover, the wind is influenced by inertial and Coriolis forces as well as the friction force induced by the motion of the wind at the earth's surface [11]. Atmospheric Boundary Layer (ABL) is the portion of the atmosphere that is in direct contact with the earth's surface [84], hence ABL can be considered the lowest part of the atmosphere. Momentum, water vapor, and heat changes

between the air and the surface occur within the ABL. For instance, drag forces induced by the motion of the wind diffuse by turbulent mixing.

The ABL thickness can vary from 100 m to 3,000 m depending on the terrain surface roughness, air density, and the angle of latitude [84]. In addition, the ABL can be splited into two main parts an inner part and an outer part (Ekman layer). The inner region is further divided into two sublayers, namely the interfacial (roughness) sublayer, and the inertial (logarithmic) sublayer.
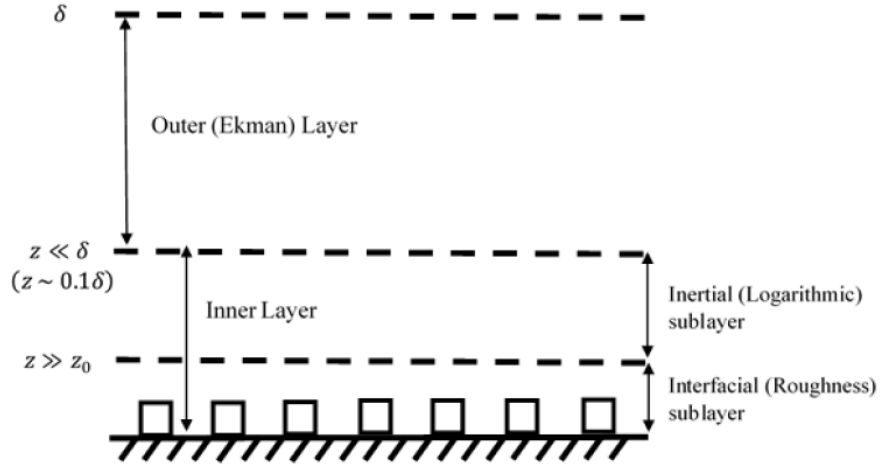
Figure 2.7. The layout of the structure of the ABL [85]

Horizontal velocity, starting from the zero location where velocity is zero which is called the no-slip condition, in the ABL profile increases with the height. Thus, velocity gradient occurs in the vertical direction. Two models which are frequently used to model the vertical velocity profiles are the log-low and the power law. Logarithmic velocity profile can be defined as:

$$U(z) = \frac{u^*}{k} \ln \left(\frac{z}{z_0} \right) \qquad (2.7)$$

where z is the elevation above the ground, z_0 is the surface roughness length and k=0,4 is von Karman's constant. $u^* = \sqrt{\frac{\tau_0}{\rho}} = \sqrt{-(\overline{u'w'})}$ is the friction velocity, where ρ is the air density and τ_0 is shear stress at the surface. [71].

$$\frac{U(z)}{U_{ref}} = (\frac{z}{z_{ref}})^\alpha \qquad (2.8)$$

Equation (2.7) is the basic form of the power law where U(z) is defined as the wind speed at z location, U_{ref} is the reference wind speed at z_{ref} which is the reference height and α is the power law exponent. α is associated with the turbulence level of the atmosphere and depends on the Atmospheric Boundary Layer (ABL) stability and surface roughness.

Depending on the vertical temperature distribution of the atmosphere, the ABL stability (i.e. the capacity of the atmospheric boundary layer to withstand vertical motion or dampen current turbulence) is frequently categorized as stable, neutrally stable, or unstable. In the case of unstable ABL, the air close to the surface that is highly heated rises and starts to cool adiabatically. If cooling is not enough to ensure thermal equilibrium between the heated air and the ambient, the heated air continues to ascend and generates large convection cells. Consequently, a thick boundary layer consisting of turbulent eddies on large scales is formed. When the ABL is stable, the heated air cools down to become cooler than the ambient air so that vertical motion within the ABL is vanquished. Thus, in stable conditions, wind shear is considerable and friction with the ground dominates turbulence. On the other hand, the air that rises in a neutral atmosphere is in thermal equilibrium with its surroundings.

2.4.2.1.1 Simulation of Atmospheric Boundary Layer

The ABL can be simulated using passive and active techniques in wind tunnel studies. Turbulence grids, spires, roughness elements, vortex generators, barrier

walls, and combinations of these experimental tools can be classified as passive techniques. Furthermore, there are active techniques like active turbulence grids, jets, and multiple fans. Certain conditions, such as the velocity profile, turbulence intensity level, turbulent length scales, and power spectrum, must be met in order to accurately recreate the ABL inside the wind tunnel.

Passive atmospheric boundary layer simulation techniques have been used in early experimental studies. For instance, to reproduce the characteristics of the ABL, Owen, and Zienkiewicz [86] employed a grid with parallel rods in which rods thicken from the top wall to the bottom wall. Results show that varying distance between the rods develops a linear or logarithmic variation of the velocity profile at far downstream. Phillips [87] utilized flat plates with varying lengths and spacing between the two adjacent plates to generate shear flow with zero pressure gradient. It is revealed that flow characteristics can be controlled by changing both length and spacing between the flat plates.

Counihan [88]–[90] conducted a series of experiments to simulate the ABL inside a wind tunnel and examined the wake characteristics of four different vortex generators, namely triangular, cranked triangular, plane elliptic, and wedge elliptic. Using the triangle generator, Counihan observed a trend for redundant momentum loss in the inner part of the boundary layer and insignificant loss in the outer area. On the other hand, the elliptic wedge generators generated satisfactory results in a rural setting. Counihan [89] performed further experiments and used roughness elements, which are called "LEGO" bricks, placed on the bottom wind tunnel wall to mimic the characteristics of the terrain surface. He introduced empirical relations which relate the planar density distribution of the roughness elements to aerodynamic roughness length.

Standen [91] experimentally studied to reproduce the ABL in wind tunnels with different triangular shapes called spires to generate a thick shear layer and showed that spires can be used to simulate the ABL up to 450 m. Irwin [92] improved Standen's method and developed a design approach for spires with a triangular

31

shapes. Results show that the vertical velocity profile of the ABL can be simulated by the triangular shape spires mounted at the inlet of the test section chased by roughness elements. Farell and Iyengar [93] simulated the ABL in a wind tunnel for urban terrain conditions. They produced the initial momentum deficit by utilizing a combination of a barrier wall with quarter-elliptic, constant wedge-angle spires or triangular flat spires, and then cubic roughness elements are placed with a staggered layout in the wind tunnel. They showed that the velocity profile matches the boundary layer with a power law exponent of 0.28. A comparison of experimental data and real scale values in terms of turbulence intensities and integral length scales also demonstrates that this simulation can be employed at sizes of approximately 1: 500 to imitate the flow towards the center of a metropolitan region. Balendera et al. [94] performed a wind tunnel study through five quarter-elliptic wedge spires, a castellated barrier, and roughness elements to simulate the ABL for urban terrain conditions. On a scale of 1:375, the simulated results were found to match the atmospheric data for urban terrain quite well.

In conjunction with advances in technology and control systems, active techniques in simulations of the ABL have been started employed in wind tunnel facilities. Teunissen [95] utilized a grid of 8 x 8 jets to simulate the ABL in a wind tunnel by inducing turbulence into the flow. By adjusting the flow rates of jets in columns and rows, he achieved to reproduces of homogenous two-dimensional linear shear flow. Cao et al. [96] used 99 individually controllable fans and oscillating airfoils to simulate the ABL with desired velocity profiles in the wind tunnel of Miyazaki University. Pang and Lin [97] simulated the ABL by combining two controllable vibrating spires (a version of traditional spires which is divided into two pieces and controlled by servo motors) and roughness elements.

2.4.2.1.2   Design Methodology of Spires

The spires used in experiments are designed to simulate a specific atmospheric boundary layer depth identified by a power law exponent in the mean velocity profile

which represents a specific terrain or exposure type by using the methodology represented by Irwin [92]. The spires are placed symmetrically at the inlet of the test section with a constant lateral spacing which is arranged cautiously to ensure homogeneity and uniformity in the mean velocity [98]. Spire lateral spacing (s) and the spire height (h) relations are given in Irwin [92] by:

$$s = \frac{W}{N} \qquad (2.9)$$

$$h = \frac{2W}{N} \qquad (2.10)$$

where W is the width of the test section and N is the number of spires.

Irwin [92] introduced a relation that is the ratio of the boundary layer thickness to spire height using obtained data from various wind tunnel experiments as can be seen in equation (2.10).

$$\delta = 0.72h(1 + \frac{1}{2}\alpha) \qquad (2.11)$$

where α is the mean velocity power law, exponent. Furthermore, to calculate the total frontal area of the spires, equation (2.11) can be used, which is given as:

$$A_S = \frac{\Psi HW}{(1 + \Psi\theta)C_{D_0}} \qquad (2.12)$$

where $C_{D_0} = 1.45$ is the true drag coefficient and θ=1.7 is the blockage factor given in Irwin [92] in the range of 0.02<$\frac{b}{h}$<0.2. In addition, Ψ, which is a coefficient, can be calculated as follows.

$$\Psi = \beta \frac{[\frac{2}{1+2\alpha} + \beta - \frac{X_0}{\delta}\frac{0.136\alpha}{1+\alpha}]}{(1-\beta)^2} \qquad (2.13)$$

where X_0 is the distance from the spires.

As a final step, in the range of $0.02 < \frac{b}{h} < 0.2$, the area of the base of the spires associated with the height, number, and frontal area of the spires can be computed as follows.

$$b = \frac{2A_S}{Nh} \qquad (2.14)$$

For more details about the design process of the spires used in the RÜZGEM C3 Wind Tunnel, please refer to [98].

2.4.2.2   Experimental Setup and Details

Similar to the uniform flow with low ambient turbulence intensity and the passive grid turbulence cases, the free stream Reynolds number is fixed to 100,000 based on the free stream velocity outside the boundary layer and the model wind turbine/porous disc diameter in all cases. Wake measurements are conducted at different vertical positions inside the boundary layer resulting in different velocity gradients, ambient turbulence intensity, and shear profiles.

Figure 2.8 shows the velocity and turbulence intensity profiles at the downstream position where both the model wind turbine and the porous disc are placed. Furthermore, the velocity profile is fitted using power law with a power law exponent of 0.14 (α=0.14). Using the assessment of the velocity gradient profile in the wall-normal direction, the boundary layer thickness at x=0 is calculated to be roughly 670 mm from the bottom wall, and then other boundary layer parameters are calculated as can be seen in Table 2.4.
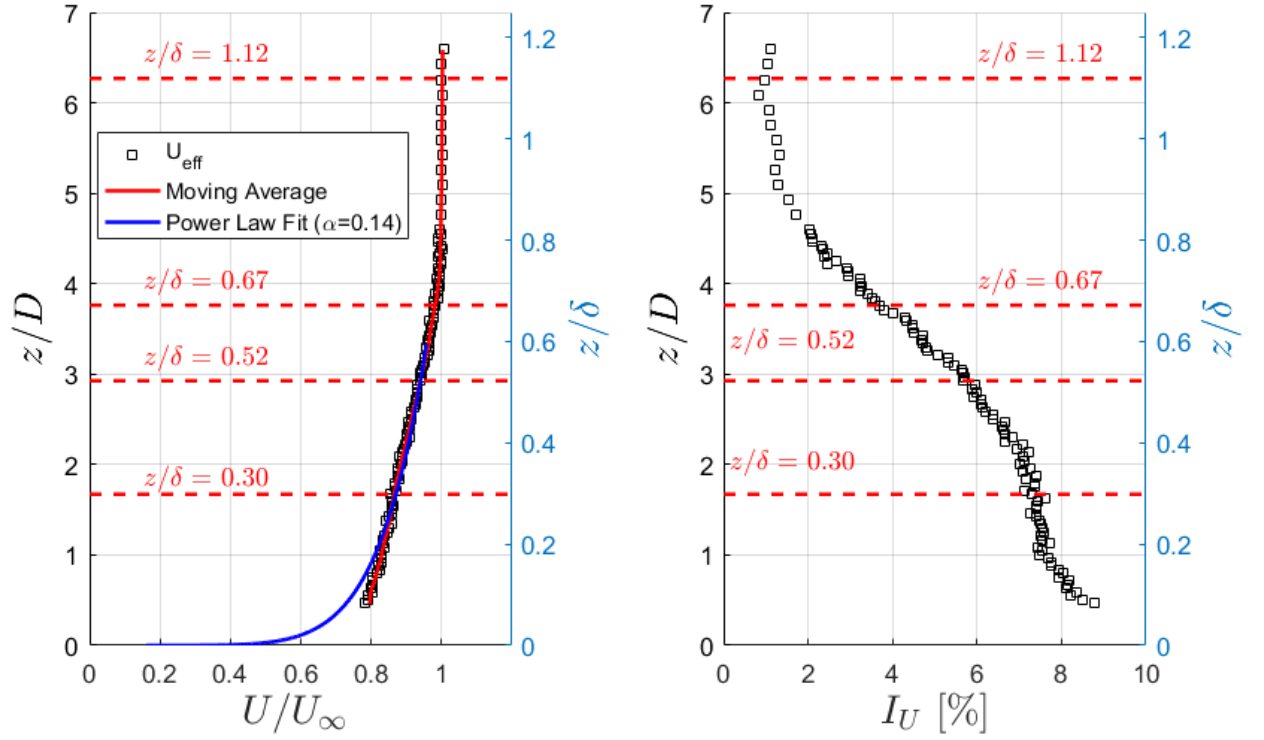
Figure 2.8. Normalized mean streamwise velocity (left) and turbulence intensity (right) profiles in the wall-normal direction

Table 2.4. Aspects of the boundary layer at the wind turbine/porous disc position (x=0).

Boundary layer properties	α	δ (m)	δ* (m)	θ (m)	δ*/θ
Wind turbine/porous disc position (x=0)	0.140	0.670	0.056	0.047	1.190

The positions, which are selected to place the model wind turbine and the porous disc for wake measurements, from the bottom wall in the boundary layer in the test section in terms of z/D and z/δ and corresponding free stream conditions are listed in Table 2.5 and shown in Figure 2.8. The wake measurements are conducted outside the boundary layer downstream of the model wind turbine and the porous disc

(z/δ=1.12) is selected as the baseline case. From Table 2.5, as expected, lowering the positions within the boundary layer results in lower free stream velocity at hub level (z=0) and Reynolds number and higher turbulence intensity.

Table 2.5 Free stream conditions in the wake measurements of the model wind turbine and the porous disc

z/D	6.17	3.75	2.92	1.67
z/δ	1.12	0.67	0.52	0.30
Re_D	1.01×10^5	9.68×10^4	9.58×10^4	9.06×10^4
U_{hub} (m/s)	14.86	14.65	14.04	12.76
U_{hub}/U_∞	1	0.98	0.94	0.85
I_{hub} (%)	0.70	3.55	5.80	7.73

Figure 2.9 presents the sketch of the test section of the wind tunnel and the setup used in wake measurements. Both models are located 6 m downstream of the test section inlet, which is the same location in the grid turbulence case. However, the position of both models altered in the vertical direction to obtain various inflow velocity and turbulence intensity profiles. Figure 2.10 shows a sketch of the measurement setup. Similar to the previous case, the reference for the wake measurements is the (x, y, z) coordinate system with the origin which is fixed to the center of the model wind turbine and the porous disc.
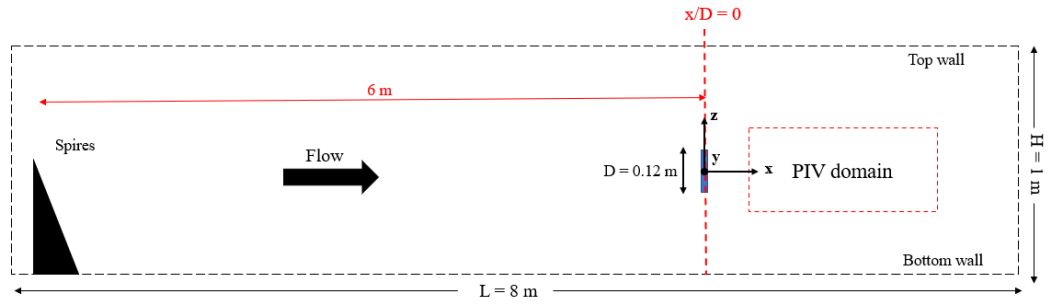
Figure 2.9. Sketch of the measurement setup of the boundary layer case.

The same thrust coefficient matching procedure used in the turbulence grid case is employed and the model wind turbine is operated at 4250 rpm. The velocity fields downstream of the model wind turbine and the porous disc are obtained with 2D2C PIV along the vertical plane (x-z plane). Double-frame particle images are pre-processed with a low-pass filter technique to advance the image quality and substitute background noise. The generated vector maps are then subjected to three-step adaptive correlation analysis with a final interrogation window size of 32x32 pixels^2 and 50% overlap, and a vector spacing of 1.56 mm is obtained.
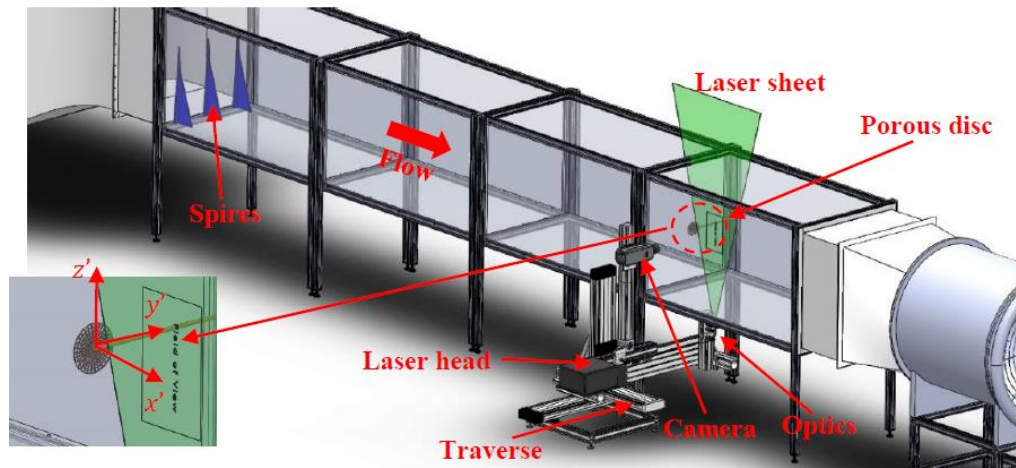
Figure 2.10. PIV setup employed in wake measurements [21]

The wake measurements are performed in a range of $0.5 \leq x/D \leq 7.0$ downstream of the model wind turbine and the porous disc. Figure 2.11 illustrates the multiple PIV measurement windows which are combined to obtain the total vector field. The positions of the field of view are illustrated as rectangular shapes in the x-z plane using the coordinate system mentioned before. The grey-colored fields between the windows depict the 0.12D (%) overlap region of two adjacent fields of views (FOVs), which corresponds to about 10 vectors. The area of each field of view (FOV) is 172 x 268 mm2 (1.43D x 2.23D) along the streamwise and the vertical directions, respectively. The model wind turbine and the porous disc location are shown as a blue rectangle with an exaggerated thickness for the sake of clarity.

The total averaged vector field is obtained by stitching and averaging 1000 image pairs for each field of view to assure statistical convergence for each case. Acquisition frequency is set at 10 Hz.
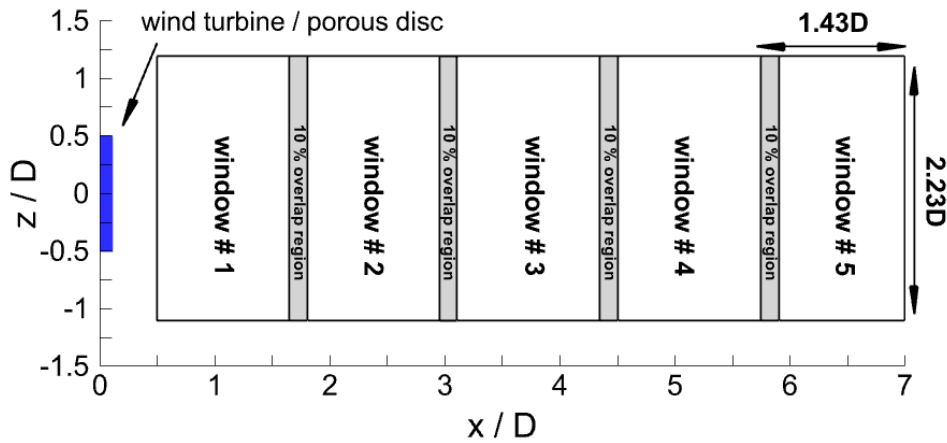
Figure 2.11. The domain of PIV measurements in the flow field shows the field of view dimensions and the overlap regions. The blue rectangular region represents the wind turbine/porous disc located between $-0.5 \leq z/D \leq 0.5$

38

2.5 Uncertainty Analysis

To obtain statistical convergence of the flow field variables, it is crucial to quantify the uncertainty of the errors in PIV measurements. Typically, systematic and random errors are used to categorize these measurement inaccuracies [99]. Peak locking, calibration, particle time response, optical distortions, and synchronization are the most common causes of systematic errors [99]. Normally, these errors are fixed through corrections or treated as insignificant. As opposed to this, random errors that change over time during measurements are typically linked to out-of-plane motion, low seeding densities, displacement gradients, and recording noise [99]. Some random errors, however, are insignificant in comparison to others and can also be disregarded. The estimation of the displacement and associated gradients accounts for most random errors. As a result, since a finite number of samples are employed in calculations, the estimation of the statistical properties of the flow field determined from the instantaneous velocity field using PIV measurements is impacted by the convergence error [100], [101]. In the current work, for both inflow conditions and each case, 1000 vector fields are used. It is assumed that these vector fields are uncorrelated and follow a normal distribution since they are stochastically independent.

It is worth noting that the following statistical uncertainty statistics demonstrate percentage differences; therefore, they are not comparable with those of the values given in the result parts.

Table 2.6 presents the normalized uncertainty approximates of flow quantities for the grid turbulence case. One can observe that estimated uncertainty values are higher in the model wind turbine cases than that in the porous disc cases. Moreover, estimated uncertainty values increase as ambient turbulence intensity increases.

Table 2.6 The normalized uncertainty estimates for grid turbulence case

Test Cases	WT-ng	WT-g	PD-ng	PD-g
$(\varepsilon_U/U_{hub})_{mean}$ [%]	0.426	0.565	0.349	0.501
$(\varepsilon_W/U_{hub})_{mean}$ [%]	0.427	0.500	0.325	0.395
$(\varepsilon_{\overline{u'u'}}/U_{hub}^2)_{mean}$ [%]	0.060	0.085	0.040	0.066
$(\varepsilon_{\overline{w'w'}}/U_{hub}^2)_{mean}$ [%]	0.059	0.067	0.034	0.040
$(\varepsilon_{\overline{u'w'}}/U_{hub}^2)_{mean}$ [%]	0.046	0.057	0.027	0.038
$(\varepsilon_k/U_{hub}^2)_{mean}$ [%]	0.043	0.055	0.027	0.039

Table 2.7 and Table 2.8 present normalized uncertainty estimates for the boundary layer case. Similar to turbulence grid case conditions, it is evident that normalized uncertainty estimates are higher in the wind turbine cases compared to porous disc cases at the same vertical positions. Moreover, it is evident that uncertainty estimates increase as both the mode wind turbine and the porous disc merge lower positions within the boundary layer.

Table 2.7 The normalized uncertainty estimates the porous disc cases at boundary layer inflow

Test Cases	WT-20	WT-35	WT-45	WT-75
$(\varepsilon_U/U_{hub})_{mean}$ [%]	0.749	0.700	0.632	0.537
$(\varepsilon_W/U_{hub})_{mean}$ [%]	0.652	0.643	0.598	0.528
$(\varepsilon_{\overline{u'u'}}/U_{hub}^2)_{mean}$ [%]	0.138	0.123	0.103	0.802
$(\varepsilon_{\overline{w'w'}}/U_{hub}^2)_{mean}$ [%]	0.107	0.105	0.092	0.076

$(\varepsilon_{\overline{u'w'}}/U_{hub}^2)_{mean}$ [%]	0.085	0.079	0.067	0.054
$(\varepsilon_k/U_{hub}^2)_{mean}$ [%]	0.089	0.082	0.070	0.057

Table 2.8 The normalized uncertainty estimates the model wind turbine cases at boundary layer inflow

Test Cases	PD-20	PD-35	PD-45	PD-75
$(\varepsilon_U/U_{hub})_{mean}$ [%]	0.657	0.593	0.535	0.404
$(\varepsilon_W/U_{hub})_{mean}$ [%]	0.500	0.475	0.446	0.381
$(\varepsilon_{\overline{u'u'}}/U_{hub}^2)_{mean}$ [%]	0.104	0.086	0.071	0.045
$(\varepsilon_{\overline{w'w'}}/U_{hub}^2)_{mean}$ [%]	0.060	0.055	0.049	0.040
$(\varepsilon_{\overline{u'w'}}/U_{hub}^2)_{mean}$ [%]	0.055	0.048	0.041	0.029
$(\varepsilon_k/U_{hub}^2)_{mean}$ [%]	0.061	0.052	0.044	0.031

CHAPTER 3

**WAKE CHARACTERISTICS OF THE MODEL WIND TURBINE AND THE
POROUS DISC OPERATING UNDER GRID TURBULENCE**

In this chapter, the effects of inflow turbulence intensity on the wake development characteristics of the model wind turbine and the porous disc are presented in terms of the mean wake flow field, turbulence, wake decay, and wake spreading characteristics. In addition, Proper Orthogonal Decomposition (POD) analyses are conducted using PIV images for further investigation. For the sake of simplicity, hereafter, WT-ng and PD-ng refer to the wind turbine and porous disc at 0.5% turbulence intensity (i.e., no turbulence grid), and WT-g and PD-g refer to the wind turbine and porous disc at 4.5% turbulence intensity (i.e., with turbulence grid).

3.1   Mean Wake Flow Field

Figure 3.1. shows the contour plots of the normalized streamwise velocity fields in the wake of the model wind turbine and the porous disc up to 7D downstream. One can observe that all cases show fairly symmetrical velocity distribution around the centreline which is the dashed black line along the geometrical center of both models. In the case of low inflow turbulence intensity levels ($I_{ambient}$=0.5 %), in the near-wake region, results show that velocity decays rapidly in the wake of both the model wind turbine and the porous disc. Furthermore, the PD-ng case has a faster wake recovery in the near-wake region, particularly between $0.5 \leq x/D \leq 1.5$, since the porous disc performs like a passive turbulence grid transforms flow's kinetic energy into turbulence with flow jets through porous parts. However, after x/D=3, in the far wake region, wake recovers much faster in the WT-ng case compared to the PD-ng case as turbulent mixing increases significantly as a result of the tip vortices break down.

In the case of high inflow turbulence intensity level ($I_{ambient}$=4.5%), wake recovery occurs much faster in both the model wind turbine and the porous disc cases compared to the case without grid turbulence. In addition, in the near-wake region, the rate of velocity decay is higher for the porous disc case (PD-g) in comparison with the model wind turbine case (WT-g), similar to the case with low inflow turbulence intensity (i.e. uniform flow). The WT-g case wake recovers faster than the PD-g case, even though the contour levels of both cases seem to be comparable in the far wake region. Another interesting finding worth mentioning is that, when comparing the WT-ng case with the PD-g case, the velocity deficit characteristics of the turbine operating at low freestream turbulence ($I_{ambient}$=0.5%) are very similar to the wake of the disc operating at high freestream turbulence ($I_{ambient}$=4.5%), especially after x/D=4. This finding can be observed more clearly in Figure 3.3 which illustrates the velocity profiles at various downstream locations, this finding will be discussed in more detail later.

Figure 3.1. Normalized streamwise velocity fields: (a) Wind turbine-no grid (WT-ng), (b) Wind turbine-grid (WT-g), (c) Porous disc-no grid (PD-ng), and (d) Porous disc-grid (PD-g). The dashed black line marks the geometric centerline of the wind turbine/porous disc. The blue rectangular region represents the wind turbine/porous disc located between $-0.5 \leq z/D \leq 0.5$

Figure 3.2. presents the contours of normalized out-of-plane vorticity downstream of the wind turbine and the porous disc at different ambient turbulence intensity levels. At low ambient turbulence intensity level ($I_{ambient}$=0.5%), the WT-ng and the PD-ng cases show a slight asymmetrical vorticity distribution. Results reveal that, in the WT-ng case, out-of-plane vorticity diffuses quickly in the WT-ng case after x/D~4 where tip vortices break down. On the other hand, the vorticity region of the PD-ng case extends to a larger area due to the fact that out-of-plane vorticity decreases gradually only under the effect of ambient turbulence intensity. Moreover, vorticity levels in magnitude are greater in the near-wake region and lower in the far wake region in the WT-ng case compared with the PD-ng case. For the high turbulence intensity level ($I_{ambient}$=4.5%) case, both the wind turbine (WT-g) and

the porous disc (PD-g) vorticity magnitudes get reduced since increasing ambient turbulence intensity level increases turbulent mixing which results in decreasing vorticity. Nevertheless, due to the shadow of the nacelle and hub, rotational momentum, and the presence of tip vortices, the vorticity magnitude in the WT-g case is larger than the PD-g case, especially in the near-wake region similar to low ambient turbulence intensity level case. Furthermore, although the extent of the vorticity field for the PD-g case remains slightly larger than that of the WT-g case, one can observe that vorticity fields are comparable after x/D=4.

Figure 3.2. Normalized out-of-plane vorticity fields: (a) Wind turbine-no grid (WT-ng), (b) Wind turbine-grid (WT-g), (c) Porous disc-no grid (PD-ng), and (d) Porous disc-grid (PD-g). The dashed black line marks the geometric centerline of the wind turbine/porous disc. The blue rectangular region represents the wind turbine/porous disc located between $-0.5 \leq z/D \leq 0.5$

46

Figure 3.3. presents the normalized streamwise velocity profiles at x/D=2 (a), x/D=4 (b), and x/D=6 (c) for the model wind turbine and the porous disc at two different ambient turbulence intensity levels, namely low ($I_{ambient}$=0.5%) and high ($I_{ambient}$=4.5%) ambient turbulence intensity levels. Symmetrical distributions of velocity profiles along the geometrical centerline of both models (i.e. z/D=0), especially after x/D=4, can be observed under both ambient turbulence intensity conditions. Furthermore, in Figure 3.3, inherent differences between the near and far wake regions are depicted. In the near-wake region, where turbulent mixing is more efficient downstream of the porous disc and absent in the model wind turbine wake due to the effects of tip vortices, under low ambient turbulence conditions, the maximum wake deficit value is greater in the WT-ng case compared to the PD-ng case. To illustrate, the minimum wake velocity is 29% lower in the WT-ng case compared with the PD-ng case at x/D=2. However, the WT-ng case has a higher minimum velocity compared to the PD-ng case after x/D=4. For instance, the minimum wake velocity is around 12% and 14% higher in the WT-ng case, in which turbulent mixing delays due to tip vortices break down compared to the porous disc case at x/D=4 and x/D=6, respectively. For the case of higher ambient turbulence intensity, both the near-wake and the far-wake of both models exhibit comparable trends in velocity deficit distribution. The minimum velocity in the WT-g case is around 30% lower than that of the PD-g case at x/D=2. Moreover, higher ambient turbulence intensity has a clear influence on the degradation of maximum velocity deficit in both the wind turbine and the porous disc wakes. For instance, at x/D=4 and x/D=6, the maximum velocity deficit is 14% and 20% lower in the WT-g case compared to the WT-ng case and is 17% and 30% lower in the PD-g case compared to the PD-ng case, respectively. Results further indicate that even though both the wind turbine and the porous disc operate at the same thrust coefficient, the porous disc fails to match the model wind turbine velocity profiles at both ambient turbulence intensity levels [102]. For instance, at x/D=4 and x/D=6, the minimum wake velocity is around 12.5% and 11% lower in the WT-g case compared to the PD-g case, respectively. Hence the collective influence of the higher ambient

turbulence and wind turbine added turbulence results in faster wake recovery for the model wind turbine in the far-wake region in comparison with the porous disc.

Regarding average velocity fields shown in Figure 3.1 and velocity profiles shown in Figure 3.3, both the WT-ng and the PD-g exhibit similar velocity profiles and wake decay characteristics, especially in the far wake after x/D≥4 [102]. Therefore, based on the existing results for the model wind turbine, this implies that a wind turbine operating at relatively low freestream turbulence may be replicated in a wind tunnel with a porous disc working at a higher freestream turbulence level. This finding indicates that the inherent differences between the wakes of porous discs and wind turbines become less significant as ambient turbulence rises, and it also suggests that the far wake of a wind turbine operating in low freestream turbulence can be represented by a porous disc operating at high freestream turbulence levels. Furthermore, these outcomes related mean wake flow field are consistent with the results obtained by Vermeer [14], Aubrun et al. [17], Lignarolo [18], and Li et al. [103].

(a)

(b)

(c)
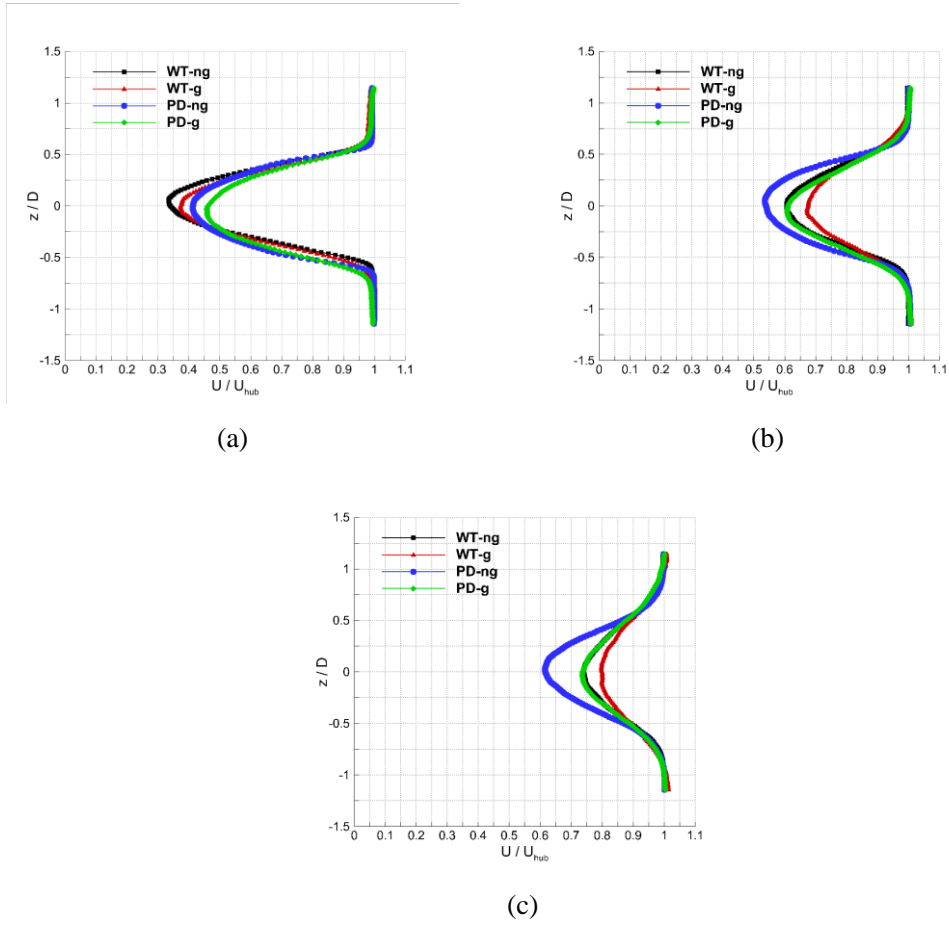
Figure 3.3. Normalized streamwise velocity profiles at different downstream positions: x/D=2 (a), x/D=4 (b), and x/D=6 (c) under different ambient turbulence intensity levels (0.5% no turbulence grid, and 4.5% with turbulence grid). Wind turbine-no grid (WT-ng), Wind turbine-grid (WT-g), Porous disc-no grid (PD-ng), and Porous disc-grid (PD-g). The wind turbine/porous disc is located between $-0.5 \leq z/D \leq 0.5$
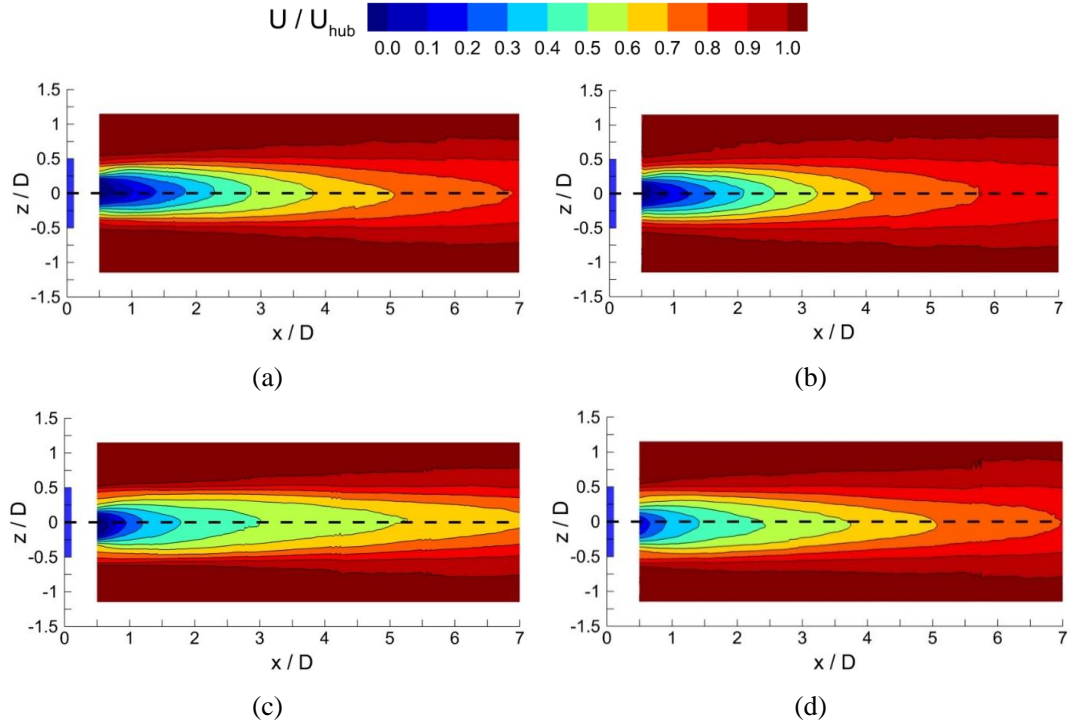
49

3.2 Wake Turbulence

Figure 3.4. Normalized mean turbulent kinetic energy fields: (a) Wind turbine-no grid (WT-ng), (b) Wind turbine-grid (WT-g), (c) Porous disc-no grid (PD-ng), and (d) Porous disc-grid (PD-g). The dashed black line marks the geometric centerline of the wind turbine/porous disc. The blue rectangular region represents the wind turbine/porous disc located between $-0.5 \leq z/D \leq 0.5$

Figure 3.4 presents the normalized turbulent kinetic energy fields in the wake of the model wind turbine and the porous disc at low ambient turbulence intensity ($I_{ambient}$=0.5%) and high ambient turbulence intensity ($I_{ambient}$=4.5%). Starting with the low ambient turbulence intensity level case, results reveal that the mean turbulent kinetic energy fields of the model wind turbine show an asymmetrical distribution while which is not the case for the porous disc. For instance, in the WT-ng case, it is evident that peak levels of normalized mean kinetic energy occur around the mid-span levels of the model wind turbine ($z/D = \pm 0.25$). In the top and bottom regions of the wake, high turbulent kinetic energy regions develop, extending up to 4D downstream for the upper part and about 2D for the lower. On the other hand, in

50

the PD-ng case, in the near-wake between $-0.25 \leq z/D \leq 0.25$ and extends up to 1D downstream and exhibits peak levels of turbulent kinetic energy. For the high ambient turbulence intensity level case, one can observe similar asymmetrical and symmetrical distributions for the WT-g and PD-g cases, respectively. Results demonstrate that increasing the ambient turbulence intensity level results in increasing the mean kinetic turbulent kinetic energy levels, especially in the near-wake and extending the high mean turbulent kinetic energy regions in the WT-g case. However, due to increasing turbulent mixing, mean turbulent kinetic energy levels reduce in the near-wake of the porous disc at high ambient turbulence intensity inflow. Furthermore, similar to the WT-g case, the higher ambient turbulence intensity results in larger high mean turbulent kinetic energy regions in the far wake of the PD-g case. One can also observe that, in the PD-g case, there is a production region where mean turbulent kinetic energy increases after x/D=4 and extends up to x/D=7, which is mentioned before in the literature [20].
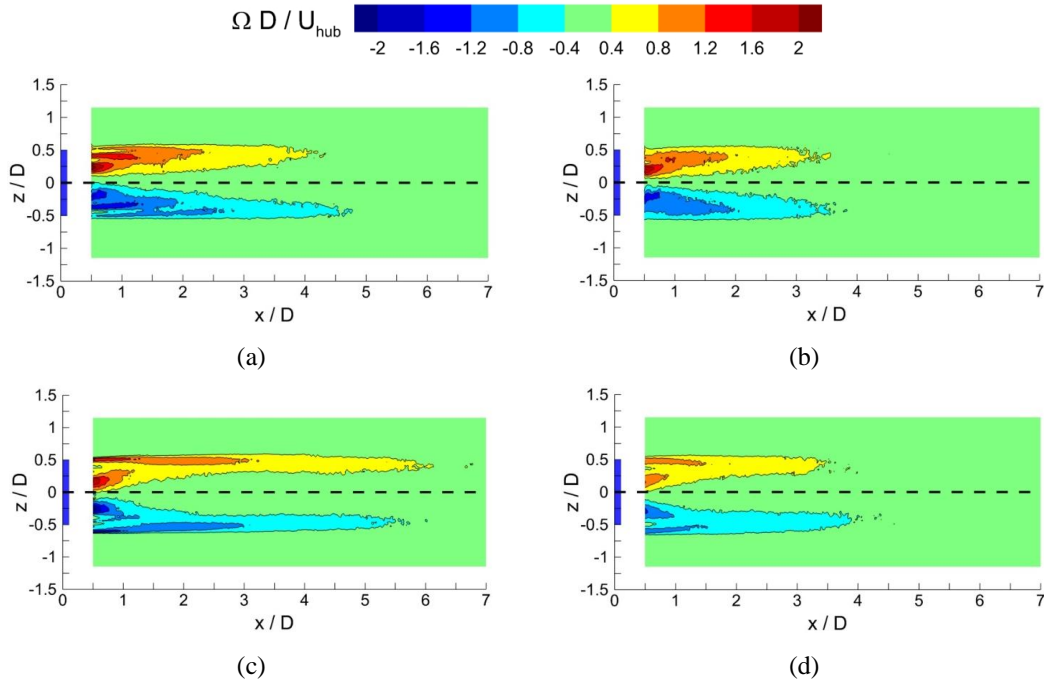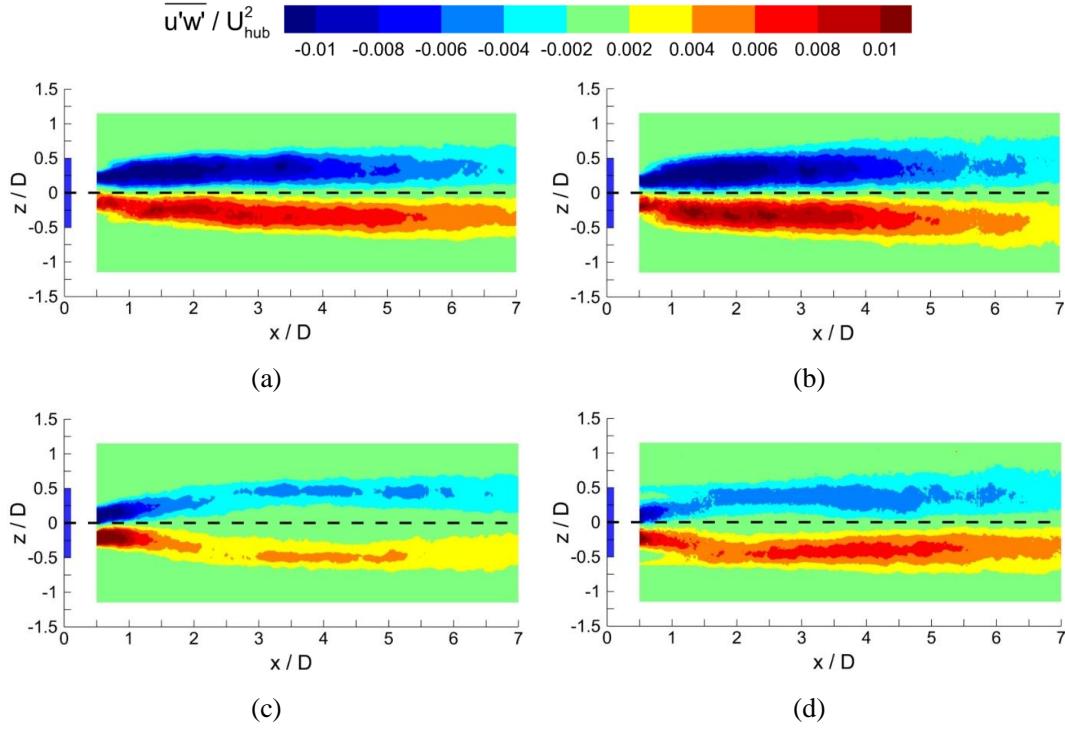
Figure 3.5. Normalized Reynolds shear stress fields: (a) Wind turbine-no grid (WT-ng), (b) Wind turbine-grid (WT-g), (c) Porous disc-no grid (PD-ng), and (d) Porous disc-grid (PD-g). The dashed black line marks the geometric centerline of the wind turbine/porous disc. The blue rectangular region represents the wind turbine/porous disc located between $-0.5 \leq z/D \leq 0.5$

Figure 3.5 presents the normalized Reynolds shear stress fields $(\overline{u'w'/U_{hub}^2})$ in the wake of the model wind turbine/porous disc at low ambient turbulence intensity $(I_{ambient}=0.5\%)$ and at high ambient turbulence intensity $(I_{ambient}=4.5\%)$. The Reynolds shear stress values change the sign in the cross-stream direction near the centerline; hence typical negative-positive distributions are clearly shown for the wind turbine and the porous disc cases [19]. Reynolds shear stress levels are higher in the near-wake, particularly near the center of the porous disc and the model wind turbine, and gradually decrease with increasing downstream locations. Under both ambient turbulence intensity conditions, the Reynolds shear stress distributions for

the wind turbine cases show elevated values compared to porous disc cases. To illustrate, for the low freestream turbulence intensity case ($I_{ambient}$=0.5%), at x/D=4, the normalized Reynolds shear stress value for the WT-ng case at the upper tip height is 62% higher than that for the PD-ng case. Moreover, the maximum levels in terms of magnitude extend up to x/D= 3.5 for the wind turbine cases, which is contributed to the average tip vortices breakdown position downstream [12], while the same levels occur between 0.5 <x/D <1 for the porous disc cases. As the inflow turbulence intensity level increases, lower Reynolds shear stress levels occur far downstream of the model wind turbine, which is not the case for the porous disc. As a result, at increasing turbulence intensity levels, the Reynolds shear stress levels cease to be comparable after x/D=4.5.
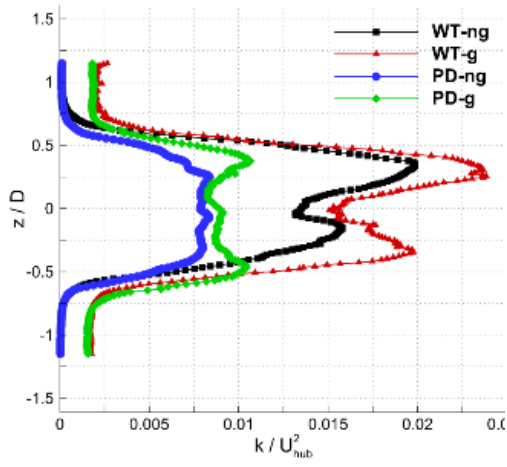
a)
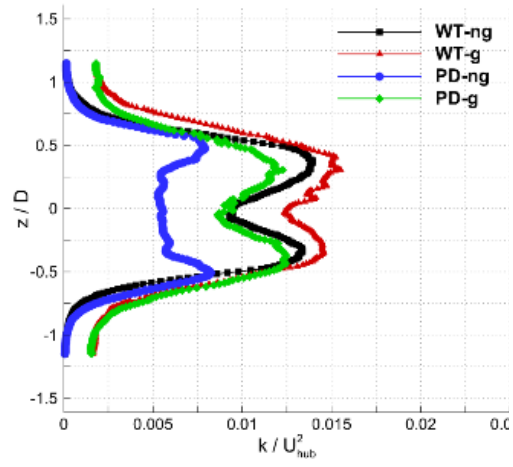
b)
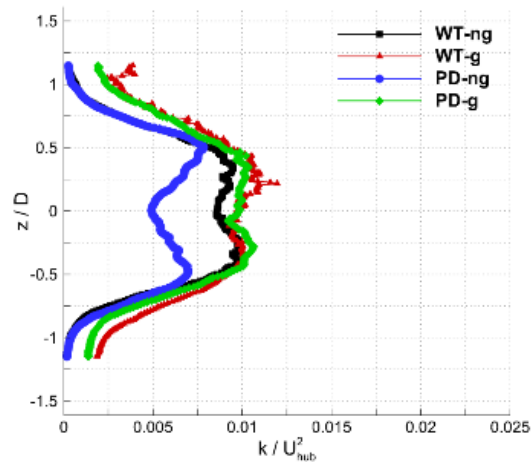
c)

Figure 3.6. Normalized turbulent kinetic energy profiles at various downstream positions: x/D=2 (a), x/D=4 (b) and x/D=6 (c) under different ambient turbulence intensity levels (0.5% without turbulence grid, and 4.5% with turbulence grid). Wind turbine-no grid (WT-ng), Wind turbine-grid (WT-g), Porous disc-no grid (PD-ng), and Porous disc-grid (PD-g). The wind turbine/porous disc is located between $-0.5 \leq z/D \leq 0.5$

54

Figure 3.6. presents the profiles of normalized turbulent kinetic energy at x/D=2 (a), x/D=4 (b), and x/D=6 (c) for the model wind turbine and the porous disc at two different ambient turbulence intensity levels. A fairly symmetrical double peak distribution is evident for both the model wind turbine and the porous disc especially starting at x/D=4. Results demonstrate that, at x/D=2, the turbulent kinetic energy levels of the model wind turbine are significantly higher compared to the porous disc. In addition, higher ambient turbulent intensity is noticeable in terms of higher peaks in the WT-g and PD-g cases. At both ambient turbulence intensity levels, the model wind turbine exhibits more turbulent kinetic energy than the porous disc at x/D=4. To illustrate, in the WT-ng case, the magnitudes of the upper peak and lower peaks are 65.5% and 62% higher compared to the PD-ng case.

Results further indicate that, regardless of downstream position, increasing ambient turbulence intensity levels results in elevated peak values. Moreover, in comparison to the porous disc case at a 0.5% turbulence intensity level (PD-ng), the peaks of the upper and lower halves rise and move through the hub level for the porous disc case at a 4.5% turbulence intensity level (PD-g). On the other hand, except for the PD-ng case where the turbulent kinetic energy levels are reduced, minor variations exhibit between the model wind turbine and the porous disc at x/D=6.
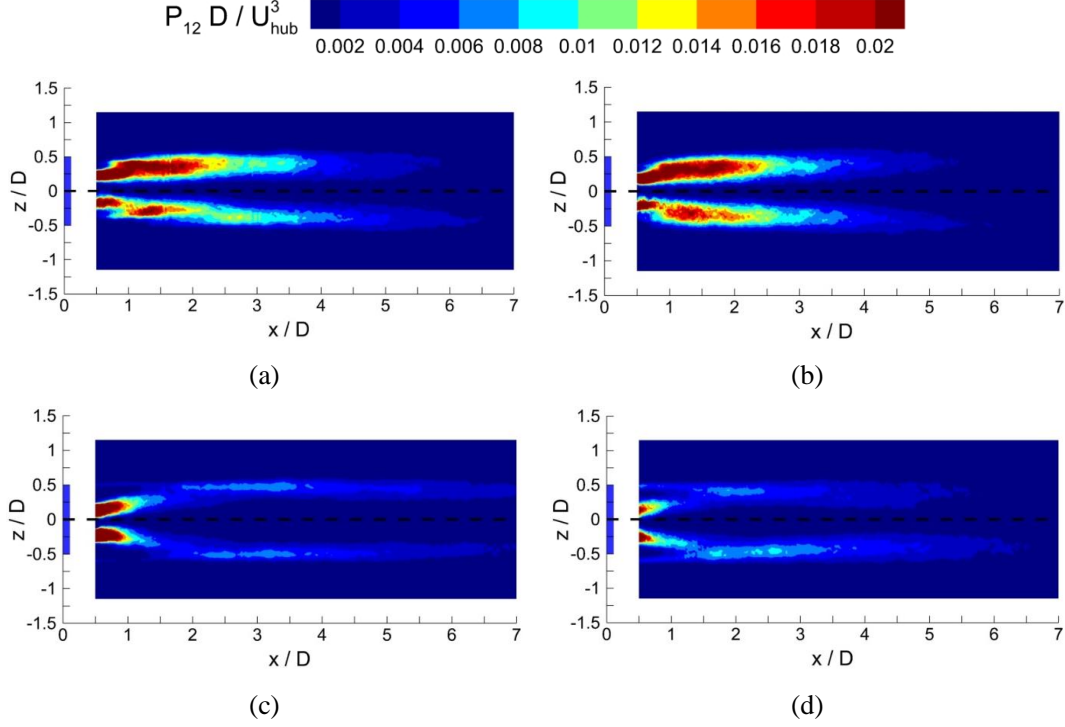
Figure 3.7. Normalized Production (P12) of turbulent kinetic energy fields: (a) Wind turbine-no grid (WT-ng), (b) Wind turbine-grid (WT-g), (c) Porous disc-no grid (PD-ng), and (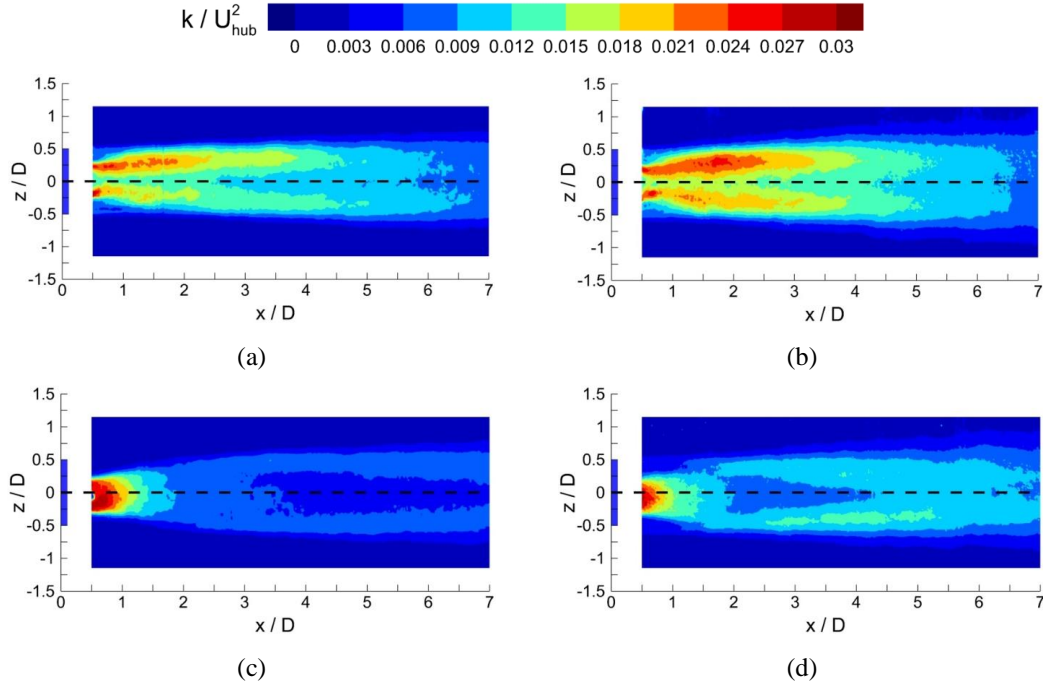d) Porous disc-grid (PD-g). The dashed black line marks the geometric centerline of the wind turbine/porous disc. The blue rectangular region represents the wind turbine/porous disc located between $-0.5 \leq z/D \leq 0.5$

Figure 3.7. presents the normalized production ($P_{12} = -\overline{u'w'}(dU/dz)$) of turbulent kinetic energy distributions in the wake of the model wind turbine and the porous disc at low ambient turbulence intensity ($I_{ambient}$=0.5%) and at high ambient turbulence intensity ($I_{ambient}$=4.5%). Similar to mean turbulent kinetic energy distribution, the model wind turbine cases have non-symmetrical production regions, while the production regions for the porous disc cases are symmetrical. In comparison to porous disc cases, the production in wind turbine cases is significantly higher. For instance, the production zone above the centerline in the WT-ng case extends up to x/D=2, whereas in the PD-ng case, it is only extended up to x/D=1. For

the case with high ambient turbulence intensity ($I_{ambient}$=4.5%), the TKE production reduces for both the wind turbine and porous disc. Results demonstrate that, regarding the extended region of the production zone in the PD-g case that reaches up to 7D downstream, the decay of the turbulent kinetic energy is lower for the porous disc compared to the model wind turbine as the ambient turbulence intensity increases. When comparing the wake development characteristics of the model wind turbine and the porous disc under the effects of varying ambient turbulence intensity level in terms of wake turbulence, the findings of the current study is in good agreement with the outcomes obtained by Aubrun et al. [17] and Lignorolo et al. [15] and Lignarolo et al. [18].

3.3   Wake Decay Characteristics

(a)   (b)
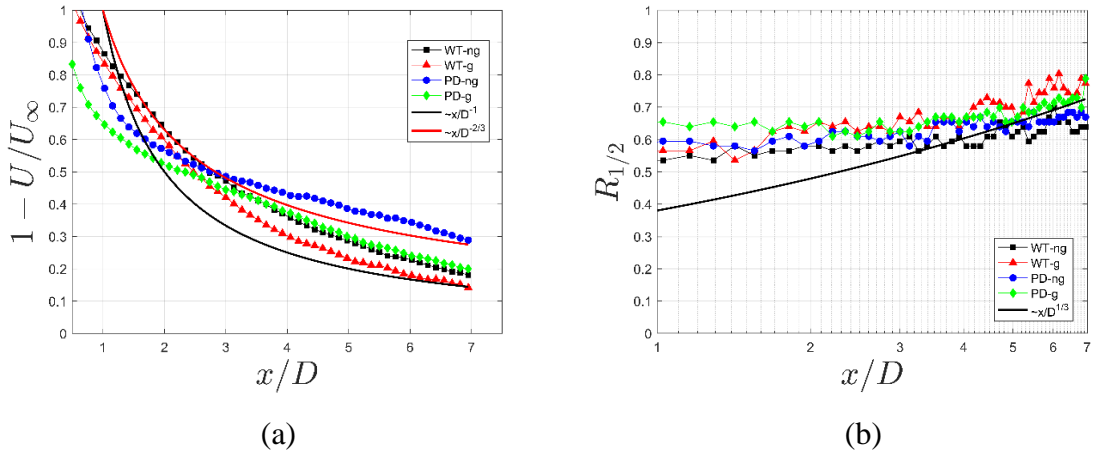
Figure 3.8. (a) Velocity deficit ($1 - U/U_{hub}$) along the geometric centerline under different ambient turbulence intensity levels ($I_{ambient}$=0.5% and $I_{ambient}$=4.5%). (b) Wake half-width for wind turbine and porous under different ambient turbulence intensity levels ($I_{ambient}$=0.5% and $I_{ambient}$=4.5%)

Figure 5.8.a presents the wake velocity deficit profiles along the wake centerline of the model wind turbine and the porous disc at two ambient turbulence intensity levels as well as wake decay variations of axisymmetric wake proposed by Johnson et al. [104] and Pope [73], which are respectively proportional with $x/D^{-2/3}$ and x/D^{-1}. Results show that, except for the PD-ng case, especially after $x/D=3$, the wake velocity deficit decays for the WT-g, WT-ng, and PD-g cases lie between the two trendlines. In this regard, one can observe that increasing ambient turbulence results in reduced differences in wake velocity deficit. Thus, this comparison indicates that it is essential to specify the operating ambient turbulence to reproduce the far wake aspects of a model wind turbine using a matched porous disc.

Figure 5.8.b presents the wake half-width distribution downstream of the model wind turbine and the porous disc as introduced in Pope [73]. Results show that the ambient turbulence intensity seems to have a slight impact on the wake half-width. Furthermore, the growth of the wake half-width is proportional to $x/D^{1/3}$ which is typical behavior for axisymmetric wake [73].
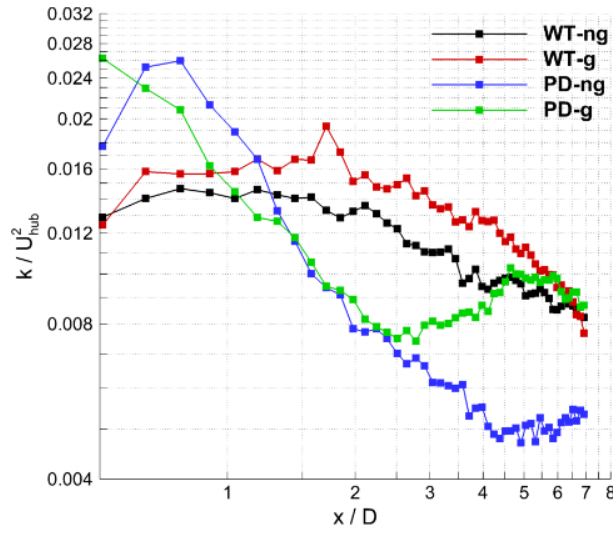
Figure 3.9. Decay of normalized turbulent kinetic energy along the geometric centerline under different ambient turbulence intensity levels ($I_{ambient}$=0.5% and $I_{ambient}$=4.5%). Wind turbine-no grid (WT-ng), Wind turbine-grid (WT-g), Porous disc-no grid (PD-ng), and Porous disc-grid (PD-g).

Figure 3.9 presents the decay of normalized turbulent kinetic energy along the geometric centerlines ($z/D = 0$) in the streamwise direction. Results show that porous disc cases have elevated turbulent kinetic energy values at a short distance downstream compared to wind turbine cases and start to decrease immediately as flow advances. On the other hand, kinetic energy profiles for wind turbine cases have similar values at x/D<1 and slightly increase up to x/D=2. After x/D=1, kinetic energy for all cases reaches similar values, and the production region starts for both wind turbine cases. This production region increases up to a peak around x/D=1.5 for the WT-ng case and around x/D=2 for the WT-g case, and then both turbulent kinetic energy profiles decrease up to x/D=7. Moreover, turbulent kinetic energy decreases up to x/D=5 and x/D=3 for the PD-ng and PD-g cases, respectively. Turbulent kinetic energy values for both porous disc cases are significantly low compared to wind turbine cases between x/D=2 and x/D=3. A production region starts at x/D=3 in the PD-g case, and turbulent kinetic energy increases rapidly.

Turbulent kinetic energy levels of WT-ng, WT-g, and PD-g cases reach similar values, and profiles collapse on each other between x/D=5 and x/D=7. On the other hand, a slight increase in the PD-ng case occurs after x/D=5, but turbulent kinetic energy values are comparably low in comparison with the other cases.

(a)   (b)
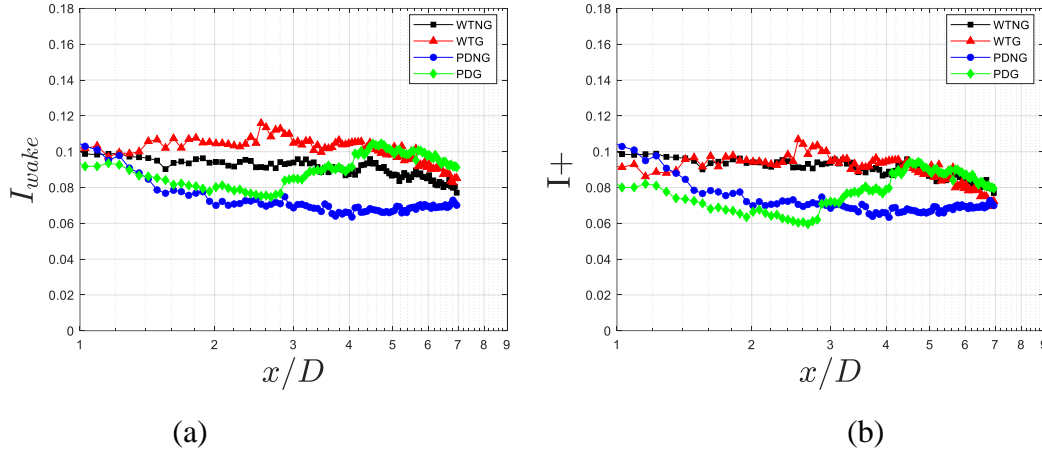
Figure 3.10. (a) Wake turbulence intensity and (b) added turbulence intensity downstream of the model wind turbine and the porous disc subjected to different ambient turbulence intensity levels ($I_{ambient}$=0.5% and $I_{ambient}$=4.5%)

Figure 3.10. presents the wake turbulence intensity (a) and the added turbulence intensity (b) along wake centerlines ($z/D = 0$) in the streamwise direction. Figure 3.10.a shows that wake turbulence intensity levels are similar at x/D=1. Additionally, higher ambient turbulence intensity effects, especially after x/D = 1.5, are evident in terms of increased wake turbulence intensity values in the WT-g and PD-g cases compared to WT-ng and PD-ng cases, respectively. A production region can be seen in the PD-g case that occurs around x/D=3. Furthermore, while an increase occurs in the PD-ng case, the wake turbulence intensity levels for the WT-ng, WT-g, and PD-g cases decrease at similar rates after x/D=4.5. Furthermore, after x / D = 6, the intensity level of the wake turbulence in PD-g is higher than that of the WT-ng and WT-g cases.

It can further be observed that, similar to the turbulent kinetic energy profiles, the added turbulence profiles of the WT-g, WT-ng, and PD-g cases collapse after x/D = 4.5, although they have different levels of wake turbulence intensity. Such observations further support the claim that a porous disc requires a certain ambient turbulence intensity level to reproduce the wake of a model wind turbine properly. In addition, it can be seen that the increase in ambient turbulence intensity has a minimal influence on the added turbulence in the wake of the model wind turbine.

3.4   Wake Spreading Characteristics

3.4.1   Bastankhah and Porté-Agel Wake Model

Bastankhah and Porté-Agel wake model [65] is based on mass and momentum conservations without viscous and pressure terms. In addition, a self-similar wake with a Gaussian shape is assumed with a linear-wake growth rate. Maximum normalized velocity deficit at a different downstream location, i.e., C(x), can be represented as:

$$C(x) = 1 - \sqrt{1 - \frac{C_T}{8(\frac{k^* x}{d_0} + \epsilon)^2}} \qquad (3.1)$$

Wake expansion is assumed linear and wake width can be written like in Jensen [59]

$$\frac{\sigma}{d_0} = k^* \frac{x}{d_0} + \epsilon \qquad (3.2)$$

where σ is the standard deviation of Gaussian-like velocity deficit profiles, d_0 is the diameter of the turbine, k^* is the wake growth rate, and ϵ is the initial wake width. Then wake velocity distribution model can be formalized as

$$\frac{\Delta U}{U_\infty} = \left(1 - \sqrt{1 - \frac{C_T}{8(\frac{k^*x}{d_0}+\epsilon)^2}}\right) \times \exp\left(-\frac{1}{2(\frac{k^*x}{d_0}+\epsilon)^2}\left\{\left(\frac{z-z_h}{d_0}\right)^2 + \left(\frac{y}{d_0}\right)^2\right\}\right) \tag{3.3}$$

where normalized velocity deficit and maximum normalized velocity deficit are defined as

$$\frac{\Delta U}{U_\infty} = \frac{U_\infty - U_W}{U_\infty} \tag{3.4}$$

Niayifar utilized LES and Porté-Agel [105] to predict the variation of the wake growth rate with ambient turbulence intensity between 6.5% and 15%, which was combined with the Bastankhah and Porté-Agel wake model. In addition, they used the same initial wake width formula from [65].

$$k^* = 0.383 I_{ambient} + 0.0037 \tag{3.5}$$

$$\epsilon = 0.25\sqrt{\beta}, \tag{3.6}$$

where $\beta = \frac{1}{2}\frac{1+\sqrt{1-C_T}}{\sqrt{1-C_T}}$.

Fuertes et al. [24], using field measurements data, formulated a wake growth rate based on Bastankhah and Porté-Agel wake model. They also introduced a relation for the initial wake width as a function of the wake growth rate.

$$k^* = 0.35 I_{ambient} \qquad (3.7)$$

$$\epsilon = -1.91 k^* + 0.34 \qquad (3.8)$$

3.4.2   Wake Spreading Results

Figure 3.11 presents the variations in wake width (σ/D) with downstream distance for the model wind turbine/porous disc at different ambient turbulence intensity levels.
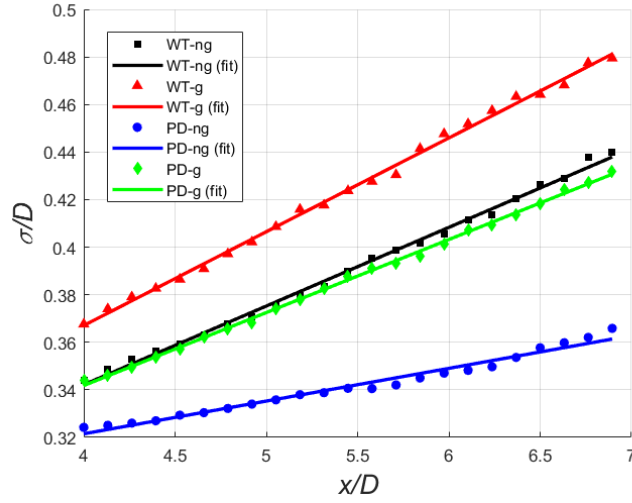
Figure 3.11. Variation of the normalized standard deviation (i.e. wake width) of the velocity deficit profiles for the wind turbine and porous disc along the streamwise direction with curve fits to obtain k^* and ϵ.

The values of wake growth rate and initial wake width for both models under different ambient turbulence intensity level conditions are tabulated in table 3.1 These values are obtained using equation (3.2) and equation (3.3), and linear curve fitting to wake velocity profiles started from x/D=4 as presented in Figure 3.11.

Table 3.1 k^* and ϵ for the wind turbine and the porous disc

Test Cases	Wake growth rate, k^*	Initial wake width, ϵ
Wind turbine-no grid (WT-ng)	0.033	0.210
Wind turbine-grid (WT-g)	0.039	0.209
Porous disc-no grid (PD-ng)	0.014	0.267
Porous disc-grid (PD-g)	0.031	0.219

It can be seen from Table 3.1 that the wake growth rate values of the model wind turbine are higher compared to that of the porous disc at both ambient turbulence intensity levels. Particularly, at low ambient turbulence intensity ($I_{ambient}$=0.5%), the

64

wake growth rate value of the WT-ng case is roughly 2.36 times higher than the wake growth rate value of the PD-ng case. However, one can observe that difference between the model wind turbine and the porous disc in terms of wake growth rate value decreases as ambient turbulence intensity increases. To illustrate, at a high ambient turbulence intensity level ($I_{ambient}$=4.5%), the difference between the wake growth rate values of the model wind turbine and the porous disc becomes fractional, and the wake growth rate value of the WT-ng case is roughly 1.06 times higher than the wake growth rate value of the PD-ng case. One can further observe that the initial wake width values of the porous disc under both ambient turbulence intensity conditions are higher than in the model wind turbine cases. In addition, it seems that increasing ambient turbulence intensity has an insignificant influence on the initial wake width for the model wind turbine. On the other hand, the initial wake width value in the PD-g case has an 18% decreased value compared to the PD-ng case as ambient turbulence intensity increases from 0.5% to 4.5%. This implies the effect of inherent differences between the wake development characteristics of the wind turbine and the porous disc, especially in the near-wake region.
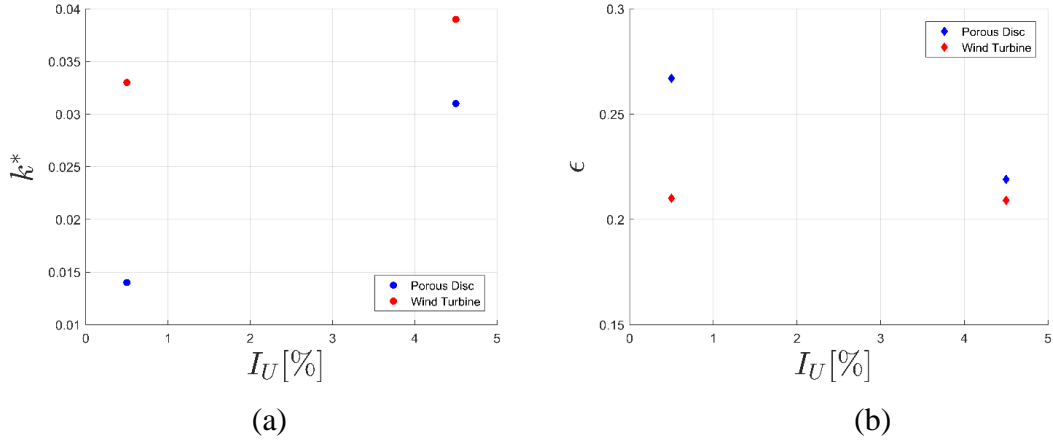
Figure 3.12. (a) Variation of wake growth rate and (b) initial wake width with ambient turbulence intensity

Figure 3.12 presents the variation of the wake growth rate and the initial wake width of both wind turbine models under uniform and grid turbulence inflow conditions. Results reveal that the wake growth rate of the model wind turbine is higher than that of the porous disc at both ambient turbulence intensities. Moreover, the wake growth rate increases with increasing ambient turbulence intensity. It is also evident that the wake growth rate of the model wind turbine case at lower ambient turbulence intensity (WT-ng) is similar to that of the porous disc at higher ambient turbulence intensity (PD-g). In addition, for the porous disc, the initial wake width decreases as ambient turbulence intensity increases while the initial wake width of the model wind turbine is insensitive to changes in ambient turbulence intensity.

3.5   Proper Orthogonal Decomposition (POD) Analysis

POD is a tool that decomposes the flow structure into a finite set of spatial modes based on kinetic energy content, and the superposition of these modes reconstructs the flow field. In the wind turbine wake, the most energetic POD modes are generally associated with large, organized structures, and they are graded according to their energy. Besides the capability of describing dominant features in the flow field, the POD is such an effective technique that maximum turbulent kinetic energy can be represented by a linear combination of a few most energetic modes. This method has recently been popular for analyzing wind turbine wakes and large-scale coherent structures of wind farms [106]–[108], due to its low computational cost and ability to order the modes regarding their energy content.

Lumley [109], [110] initially proposed this approach to study turbulence, while Sirovich [111] later developed the Snapshot POD, which is better suited to spatially dense but temporally infrequent data. POD has been applied to investigate the coherent structures in the wake of a single wind turbine as well as wind farms. Bastine [112] modeled a single wind turbine in the ABL by employing the LES and actuator disc method. Results show that using POD analysis, the wake characteristics of the single wind turbine can be approximated using only three modes. De Cillis et

66

al. [113], [114] employed POD analysis to a numerical wake dataset obtained through LES and the actuator line method to study the effects of the tower and nacelle on wake recovery. Results show that the presence of the tower and nacelle has a positive effect on wake recovery while tip vortices prevent turbulence mixing. Bastankhah and Porté-Agel [108] conducted a wind tunnel study and investigated the interaction of the ABL with a model wind turbine under different tip speed ratios and yaw angles, and used POD to examine the suitability of the method in wake meandering studies. Results indicate that a few highest energetic modes are adequate to roughly predict some characteristics of the wind turbine wake under the effect of the ABL. In order to replicate a wind farm with an infinitely long row of turbines and to analyze the wake interaction and wind turbine performance, Andersen et al. [108] combined LES with the actuator line approach. POD modes show that low-frequency dynamics are related to the ABL's large-scale movement and highly correlated with the wake dynamics. Sorensen et al. [9] numerically simulated the wake of a three-bladed wind turbine using LES coupled with the actuator line method, and then employed POD to snapshots of the flow field to validate the definition for the length of the near-wake introduced by the authors. Results reveal distinct structures such as a monopole, dipole, quadrupole, and hexapole in the plane parallel to the rotor. POD analysis is employed for numerical simulation, using LES and the actuator line method, of a single wind turbine to obtain a deeper insight into the wake dynamics by Debnath et al. [115]. Several POD modes associated with the instabilities of the tip vortices, interaction with rotor wake, and the vortex shedding from the turbine tower are detected. VerHulst and Meneveau [116] used the POD method to investigate a wind farm by LES simulations. They discovered that the dominating coherent structure in the flow is streamwise counter-rotating rolls, which form ejection and sweep zones. In order to recreate TKE production and flux from wind tunnel experiments of aligned and staggered wind turbine arrays, Hamilton et al. [99] employed POD analysis. They found that only 1% of all modes are necessary. Moreover, Hamilton et al. [107] performed Double Proper Orthogonal Decomposition (DPOD) analysis on a wake of a turbine within a wind farm. They

introduced a correction procedure for a low-order reconstruction of the Reynolds stress tensor. Camp and Cal [117] performed wind tunnel tests using PIV and compared the wake structures of a three-bladed model wind turbine and matching porous disc in the fourth row of a 4 x 3 array via POD analysis. By POD demonstration of the snapshots of the flow field obtained by PIV measurements, they identified differences in terms of scales and the structure of the wakes, especially in the near-wake region. In addition, Lignarolo et al. [118] used PIV to compare a model wind turbine to a porous disc and then employed POD analysis as a filter to separate periodic fluctuations from random fluctuations in the wake flow.

3.5.1   Mathematical Background of POD

Proper Orthogonal Decomposition (POD), particularly Snapshot Proper Orthogonal Decomposition (SPOD), is a statistical tool that breakdowns space-time flow fields into discrete spatial modes and temporal coefficients, which is done by computing the major eigenvalue and eigenvector of a matrix composed of flow snapshots.

In POD analysis, fluctuating velocity is considered as

$$u'(x,t) = U(x,t) - \overline{U}(x,t) \qquad (3.9)$$

where $U(x,t)$ is instantaneous velocity snapshots and $\overline{U}(x,t)$ is the mean velocity, and x and t refer to spatial coordinates [106]. Instantaneous vector field (i.e. $u'(x,t)$) can be decomposed a series of deterministic spatial functions

$$u'(x,t) = \sum_{n=1}^{N} a_n(t)\phi^{(n)}(x) \qquad (3.10)$$

where $a_n(t)$ is the time-dependent POD coefficient for mode n, $\phi^{(n)}(x)$ is the spatial POD mode for mode n, and N is the number of snapshots [111]. The changing

velocity that is instantaneously measured over M spatial positions and is measured at N times is organized into the matrix [110]:

$$\hat{U} = \frac{1}{N} \begin{bmatrix} u_1'^1 & u_1'^2 & \cdots & u_1'^N \\ \vdots & & \ddots & \vdots \\ u_M'^1 & u_M'^2 & \cdots & u_M'^N \end{bmatrix}$$

Then auto-covariance matrix (C) can be expressed as

$$C = \hat{U}^T \hat{U} \qquad (3.11)$$

The above steps provide to introduce this problem as an eigenvalue problem as following

$$C A_n = \lambda_n A_n \qquad (3.12)$$

where A_n is the eigenvector corresponding to the eigenvalue λ_n. The eigenvalues of all N modes are ordered in magnitude such that [117]:

$$\lambda_1 > \lambda_2 > \cdots \lambda_n \qquad (3.50)$$

where λ_n is set to zero during analysis. By projecting the snapshot basis into the eigenvalue space and then normalizing, the normalized POD modes may be produced from the solutions to the eigenvalue problems, which can be written as follows [104]:

$$\phi^{(n)} = \frac{\hat{U} A_n}{\|\hat{U} A_n\|} \qquad (3.13)$$

where $\|...\|$ denotes the L_2-norm. It's worth noting that the eigenfunctions found here are orthogonal in time rather than space. After concatenating the POD modes to form, $\Psi = [\phi^{(1)}, \phi^{(2)} ... \phi^{(n)}]$, the POD coefficients can then be found as follows:

$$a_n = \Psi^{-1} u'_n \qquad (3.14)$$

3.5.2   Results
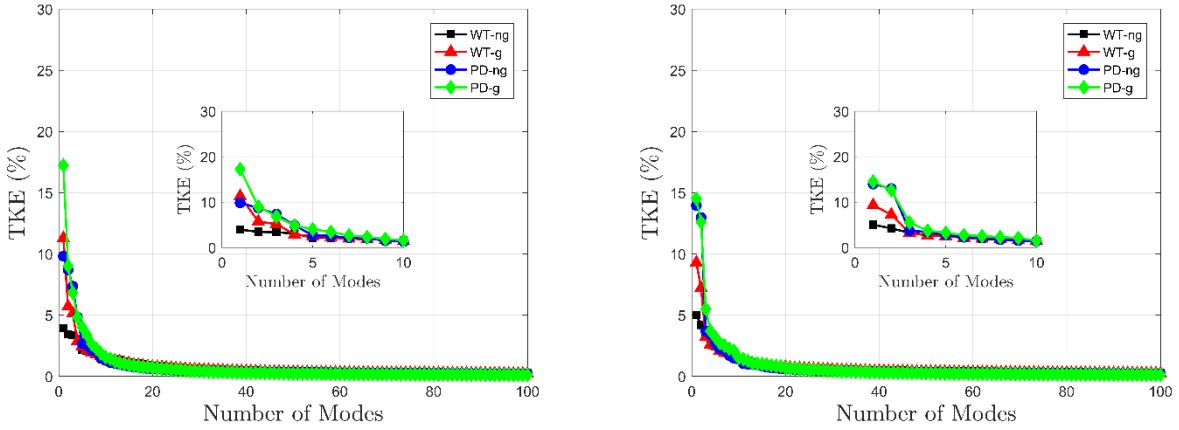
Figure 3.13. Comparison of percentage of turbulent kinetic energy (TKE) attributed to eigenvalues of first 100 modes in the near-wake of the model wind turbine and the porous disc at different ambient turbulence intensity levels: streamwise velocity (left) and radial velocity (right).

Figure 3.13 presents the comparison of the percentage of the TKE associated with eigenvalues of the first 100 modes based on streamwise (left) and radial (right) velocities in the near-wake region (0.5≤x/D≤1.5) which are sorted from the highest to lowest in magnitude obtained by Proper Orthogonal Decomposition (POD) analysis of the model wind turbine and the porous disc at two ambient turbulence intensity levels. Results reveal that the first mode of the PD-g case in terms of streamwise velocity has the highest percentage of the TKE among all cases with 17%. The percentage of the first mode of the TKE in the PD-ng and WT-g is roughly 10% and 11%. On the other hand, the percentage of the first mode of the WT-ng case

70

is only %4. The percentages of the TKE in the PD-ng, PD-g, and WT-g decrease exponentially up to 5th mode, and then occur around the same value up to 10th mode. In addition, one can observe that the TKE percentages of the WT-ng case are around from 3% to 4% up to 10th mode.

The first mode of the porous disc cases obtained from POD analysis based on the radial velocity field is significantly higher than that of the model wind turbine cases. Similar to the streamwise velocity field case, the percentages of the WT-ng case are quite low in the first modes; however, they are very similar in terms of magnitudes up to 10th mode. To illustrate, the percentage of the first mode in the PD-ng and PD-g cases are respectively 14% and 13.8% while that of the WT-ng and WT-g cases are 4% and 9%, respectively. In addition, it can be observed that percentages of the TKE in the porous disc cases are almost similar for all modes.
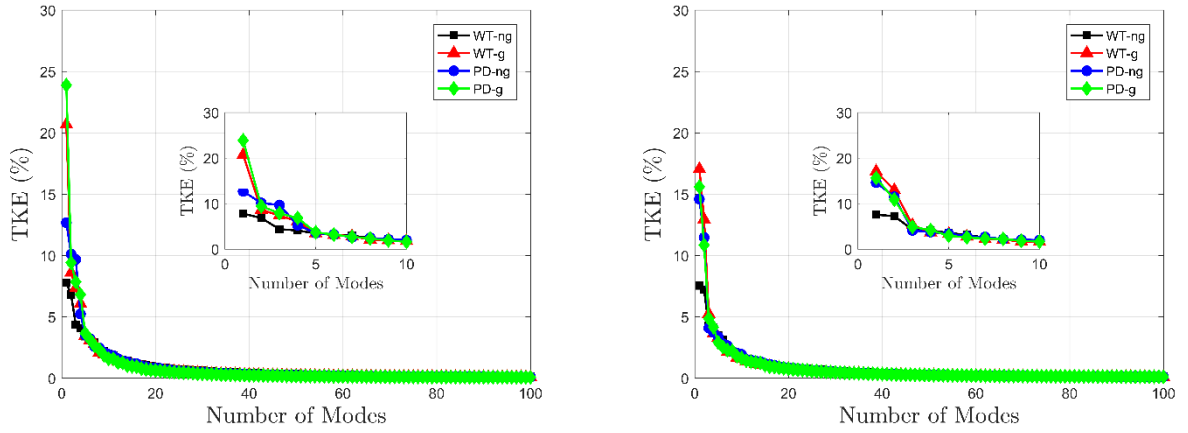
Figure 3.14. Comparison of percentage of turbulent kinetic energy (TKE) attributed to eigenvalues of the first 100 modes in the far wake of the model wind turbine and the porous disc at different ambient turbulence intensity levels: streamwise velocity (left) and radial velocity (right)

Figure 3.14 presents the comparison of the percentage of TKE associated with eigenvalues of the first 100 modes based on streamwise (left) and radial (right) velocities in the far wake region (4.6≤ x/D≤ 5.8) which are sorted from highest to

lowest in magnitude obtained by Proper Orthogonal Decomposition (POD) analysis of the model wind turbine and the porous disc at two ambient turbulence intensity levels. Results reveal that the first mode of the PD-g and WT-g cases, which are under the high ambient turbulence intensity conditions, in terms of streamwise velocity have significantly higher percentages of the TKE compared to the ones under the low ambient turbulence intensity conditions. For instance, the percentage of the first mode of the PD-g and WT-g cases are respectively 24% and 21% while that of the PD-ng and WT-ng are 11.5% and 8%, respectively. On the other hand, starting from 2th mode, the percentages of TKE for the PD-ng, PD-g, and WT-g become similar.

The percentages of TKE obtained from the radial velocity field for all cases except WT-ng have similar magnitudes for all modes. Similar to previous cases, the percentage for the WT-ng case is the smallest one among others and decreases gradually after 2th mode.
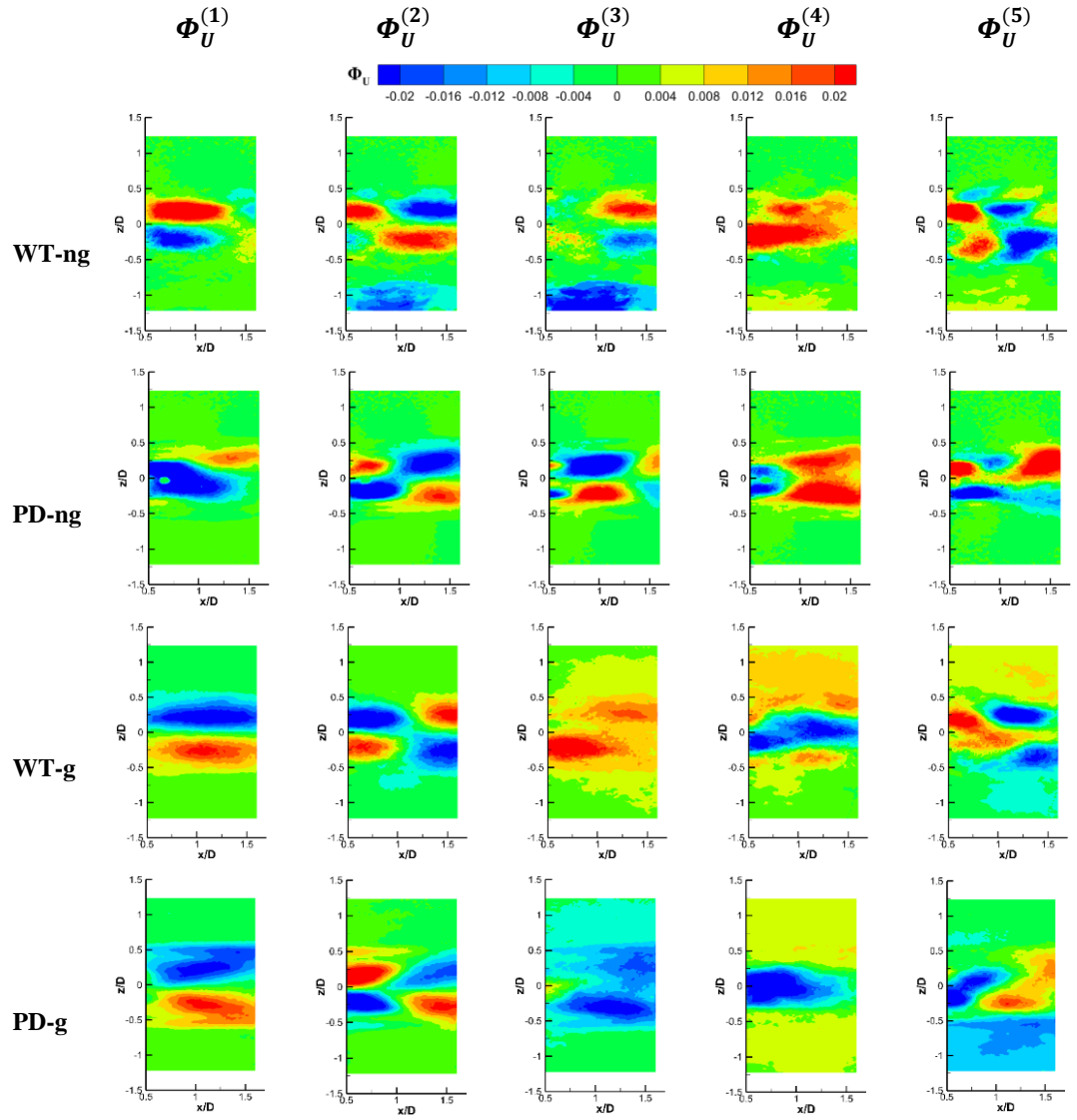
Figure 3.15. POD streamwise components (Φ_U) of first 5 modes in the near-wake of the model wind turbine and the porous disc at different ambient turbulence intensity levels.
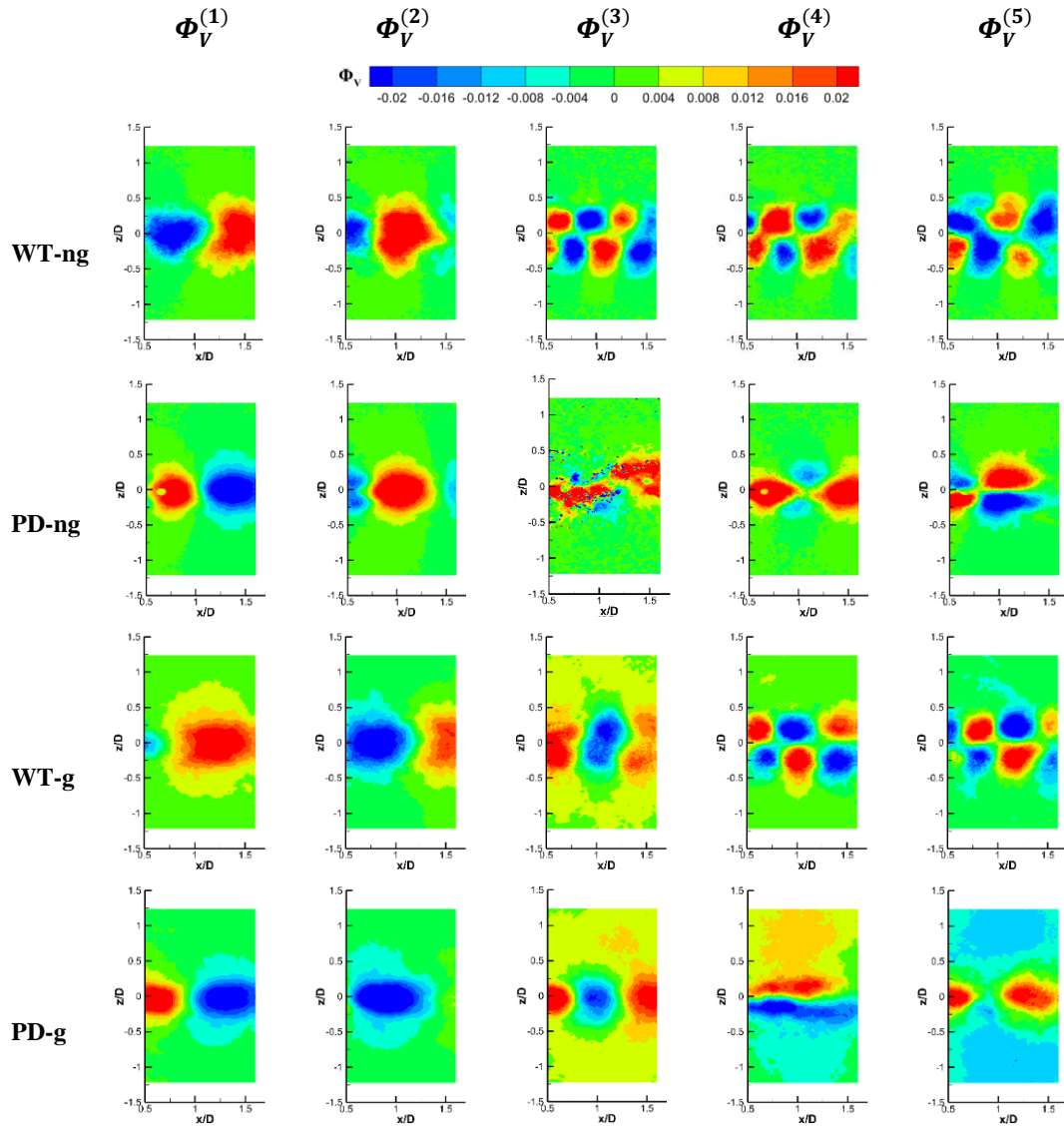
Figure 3.16. POD radial components (Φ_V) of first 5 modes in the near-wake of the model wind turbine and the porous disc at different ambient turbulence intensity levels.

Figure 3.15 and Figure 3.16 illustrates the first five modes in streamwise and radial directions (Φ_U and Φ_V) in the near-wake region of the model wind turbine and the porous disc. Results show that even though the differences in wake development are evident between the wind turbine and porous disc, with some sign and order changes, the streamwise modes of the PD-g, WT-ng, and WT-g are comparable. However, the 4th and 5th modes of the PD-ng case are not comparable with others. In addition, one can observe that the first vertical components of POD modes are fairly comparable. On the other hand, despite the fact that some vertical components such as the 3th mode of the PD-g and WT-g are quite similar, there are inherent differences between the modes for all cases.
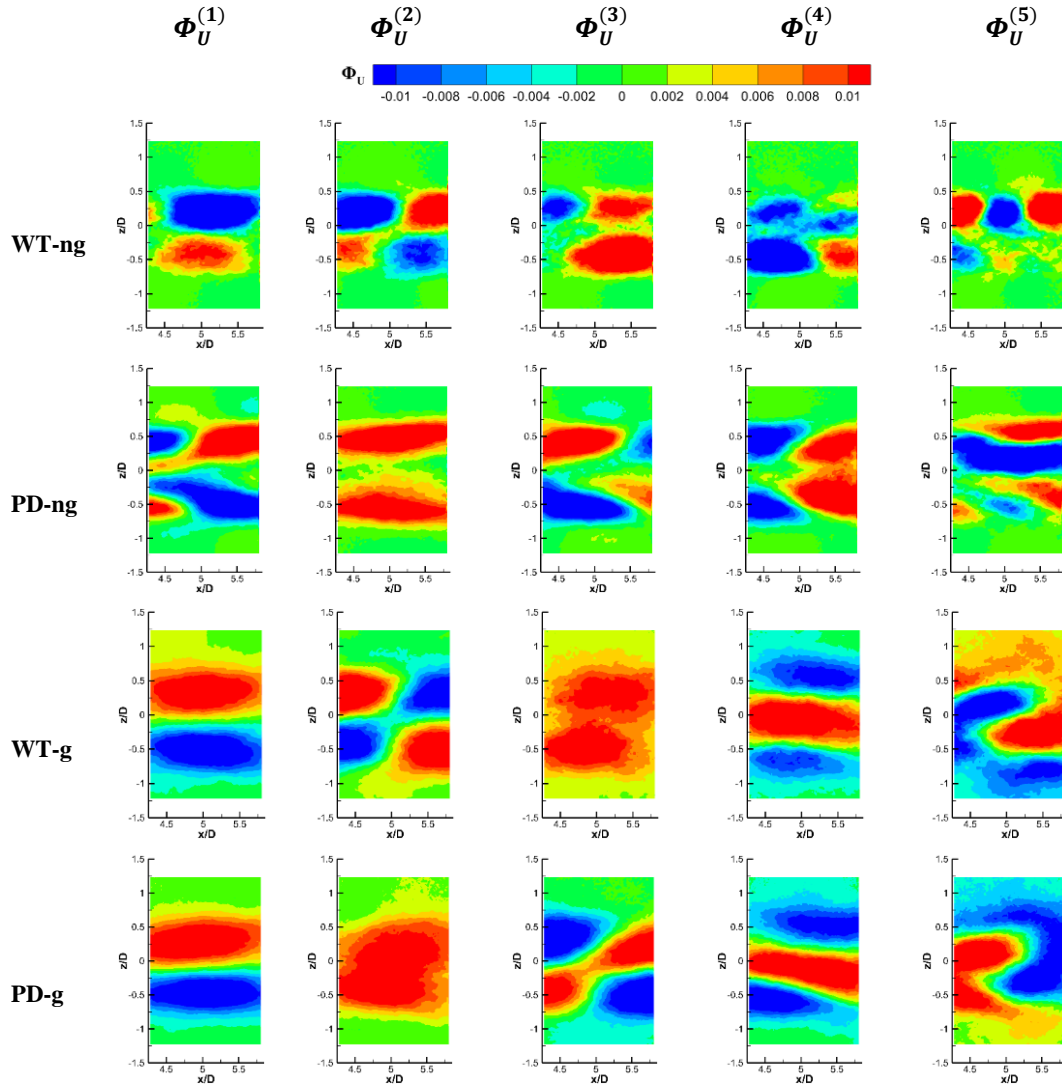
Figure 3.17. POD streamwise components (Φ_U) of first 5 modes in the far wake of the model wind turbine and the porous disc at different ambient turbulence intensity levels.
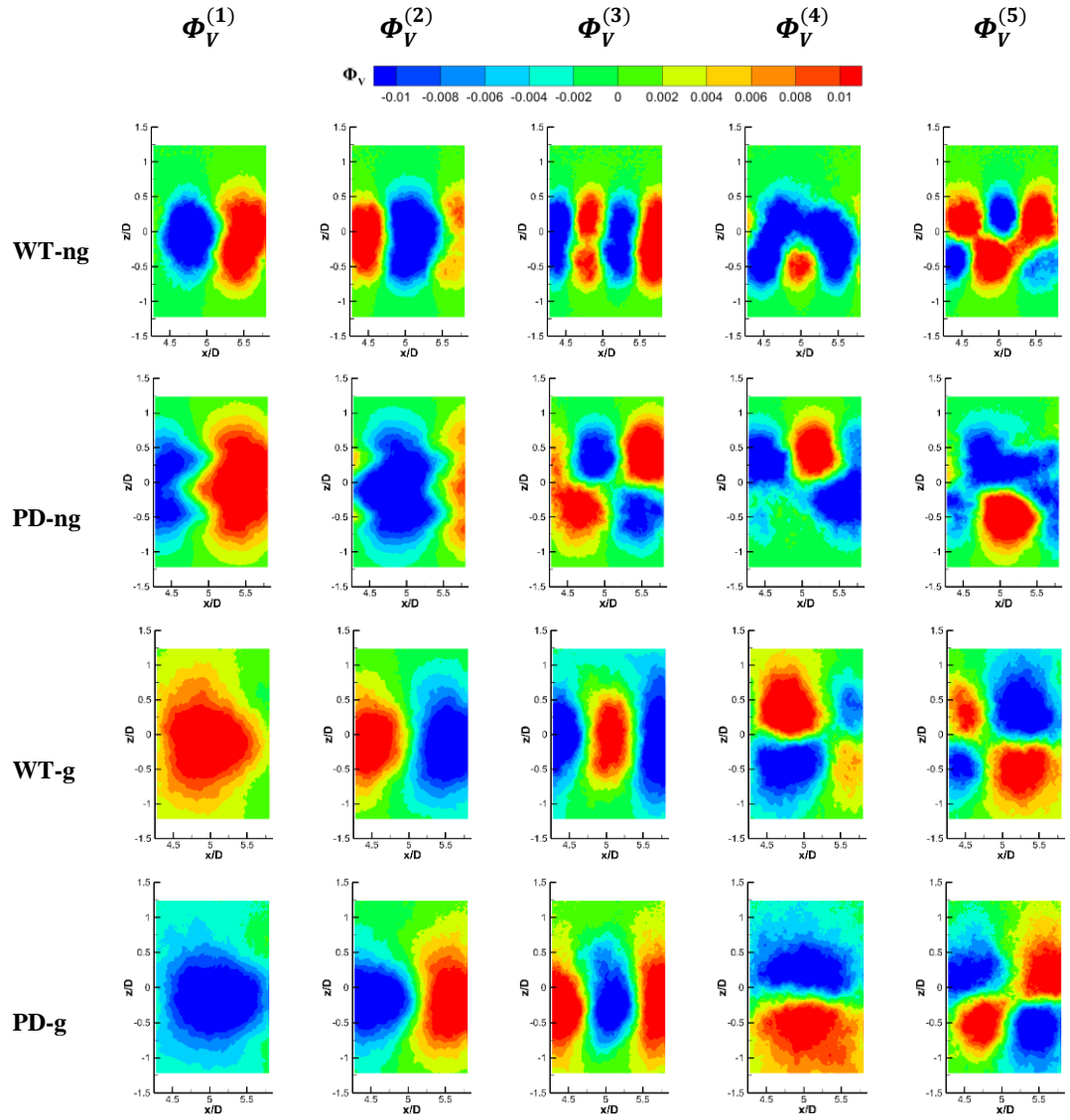
Figure 3.18. POD radial components (Φ_V) of first 5 modes in the far wake of the model wind turbine and the porous disc at different ambient turbulence intensity levels.

Figure 3.17 and Figure 3.18 illustrate the first five modes in streamwise and radial directions (Φ_U and Φ_V) in the far wake region of the model wind turbine and the porous disc. Results show that although streamwise components of the model wind turbine and the porous disc are not comparable under the low ambient turbulence intensity conditions, they are very similar at high ambient turbulence intensity. Particularly, all five streamwise components of POD modes of the PD-g and WT-g cases are quite similar in terms of shape regardless of order and sign shifts. Furthermore, similar structures can be observed in vertical components of POD modes of the PD-g and WT-g cases while which is not the case for the others.

3.6   On the Relationship Between Shear and Turbulent Kinetic Energy

It is observed that a discrepancy in turbulent kinetic energy between the top and bottom parts of the wake is evident, in the model wind turbine cases. Since passive turbulence grid inflow is supposed to be isotropic and homogenous after x/M=40 downstream the grid, such an asymmetry is not expected. Furthermore, it is observed that vertical shift in maximum velocity deficit occurs in the velocity profiles especially in the near-wake region. Thus, to investigate this difference between the top and bottom part of the wake, the turbulent kinetic energy decay is examined by addressing the shear of the wake velocity profiles. This study is further expanded to porous disc cases and the results are compared with that of the model wind turbine cases.
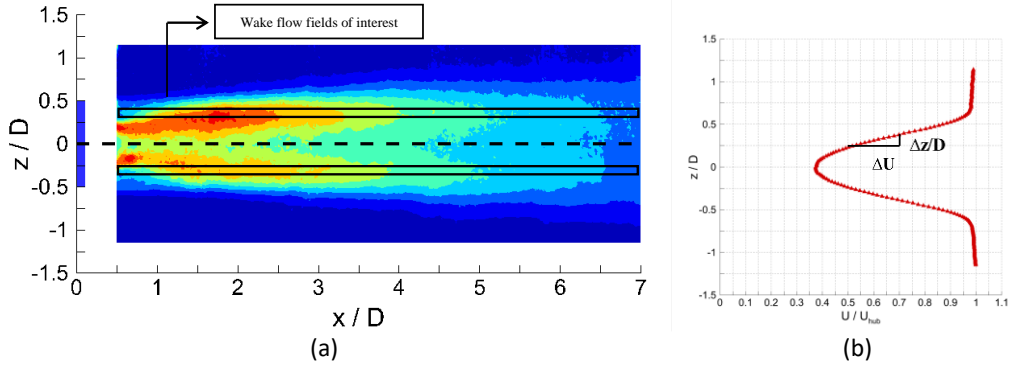
Figure 3.19. (a) Wake flow fields at the top and bottom part downstream of the model wind turbine and the porous disc of interest, (b) sketch of wake velocity distribution and quantities to calculate the gradient

Figure 3.19 illustrates the wake flow field of interest and the gradient of wake velocity between $0.25 \leq z/D \leq 0.35$, where maximum local TKE occurs in the near-wake region. Mean TKE levels are obtained by averaging all TKE values along the z direction for $\frac{z}{D} \in [0.25, 0.35]$. The averaging in the z direction is performed for improved convergence of the resulting profiles. An average wake velocity gradient is calculated for this range at each x/D location as,

$$m_U(x) = \frac{\Delta U(x)}{\Delta z(x)/D}. \qquad (3.15)$$

A similar analysis is also carried for the bottom part enclosed by $\frac{z}{D} \in [-0.35, -0.25]$. It is worth noting that distance in the z-direction is normalized with the diameter of the model wind turbine/porous disc while any normalization process has not been applied to the neither velocity nor the turbulent kinetic energy. We compare the TKE against the square root of the slope given in (3.15) as the decay rates along the downstream direction match for most of the cases when we use the square root.
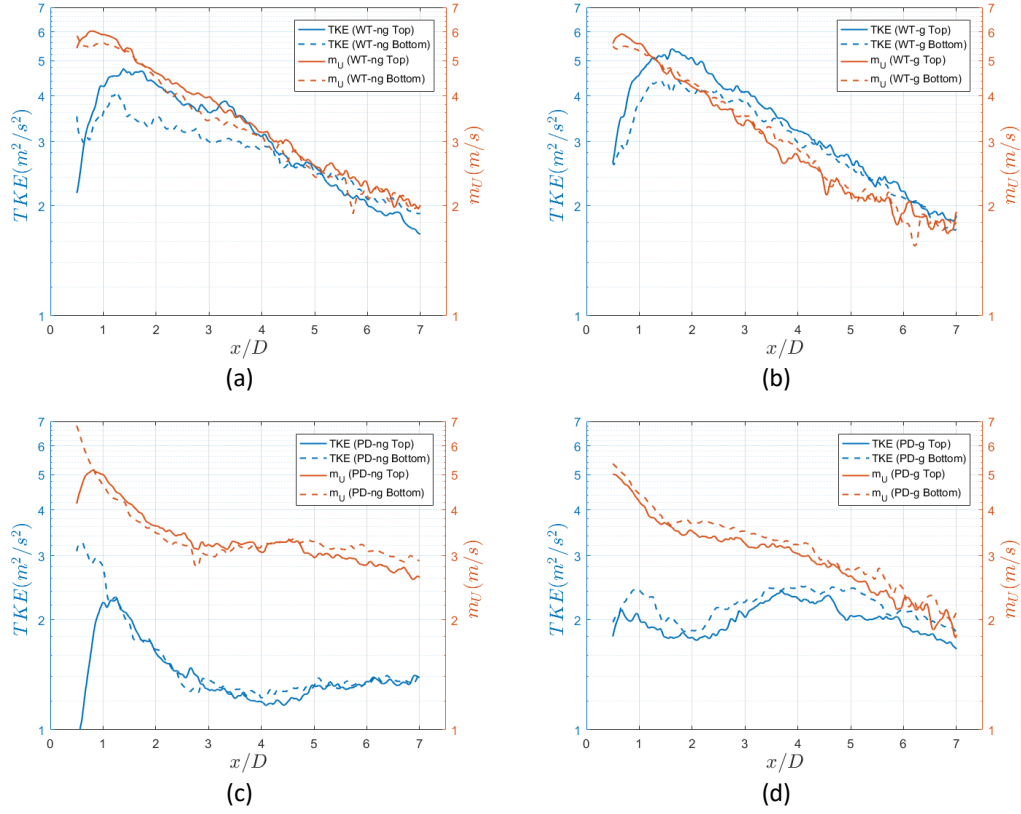
Figure 3.20. Distribution of mean TKE and the square root of wake velocity gradient at the top and bottom part of the wake: (a) WT-ng, (b) WT-g, (c) PD-ng, (d) PD-g

Figure 3.20 presents the square root of the wake velocity gradient and mean turbulent kinetic energy profiles at both top and bottom parts of the wake of all four cases. It is observed that decay rates of both TKE and the square root of wake velocity gradient at both parts of wake are almost equal beyond $x/D \approx 1.5$ for WT-ng, WT-g and PD-ng cases and beyond $x/D = 4$ for PD-g case. For WT-ng case, a discrepancy can be observed in TKE levels at the top and bottom parts for $0.5 \leq x/D \leq 1$ and the difference is maximum between $1 \leq x/D \leq 2$, although reducing as moving downstream. For the case of the model wind turbine where ambient turbulence intensity is higher (the WT-g case), one can observe that all profiles become similar and decay at the same rate after x/D=1.5.

For the PD-ng case, despite the similar trends of TKE and square root of wake velocity gradient between $0.5 \leq x/D \leq 5$, significant differences in terms of magnitude between the distributions are evident. On the other hand, trends for square root of wake velocity gradients of both halves decay while the turbulent kinetic energy distributions increase after x/D=5. For the PD-g case, TKE starts increasing at the point where the decay in the slope slows down at around $x/D = 2$. Similarly, TKE starts decreasing at $x/D = 4$ where we see a slight increase in the decay rate of the slope. A difference in both TKE and slope profiles is observed between the top and bottom parts of the wake. In other words, the distribution of both quantities at different halves of the wake is notably different. Furthermore, inconsistency between the top and bottom part of the wake in terms of turbulent kinetic energy and square root of wake velocity gradient can be observed between $0.5 \leq x/D \leq 1$. Similar to the model wind turbine cases, these inconstintencies lessen as free stream turbulence intensity level raises. On the other hand, it can be observed that the turbulent kinetic energy distribution is correlated with the square root of the wake velocity gradient downstream of the model wind turbine after x/D=1 at both parts of the wake. Both quantities increase and decrease at the same downstream position and nearly have the same values throughout the downstream of the porous disc. However, when compared with the PD-ng case, in the PD-g case, distributions of the mean turbulent kinetic energy and the square root of wake velocity gradient are fairly comparable after x/D=4 as the ambient turbulence intensity increases from 0.5% to 4.5%. In addition, one can observe that the correlation between the mean turbulent kinetic energy and the wake velocity deficit is still pronounced regardless of the free stream turbulence intensity level.

Figure 3.21 shows the comparison of the mean turbulent kinetic energy and the square root of wake velocity gradient distributions of the WT-ng and WT-g cases at the top and bottom wake parts separately. Results demonstrate that effects of inflow turbulence intensity level are more pronounced in the near-wake region so that the WT-g case has higher TKE levels up to x/D=3 at the top part and x/D=5 at the bottom part compared to the WT-ng case. On the other hand, although the WT-ng case shows

a deficit at the top part, TKE values are nearly the same at the bottom part in the far-wake region. Nevertheless, the decay rate of both quantities are comparable at both parts of the wake.
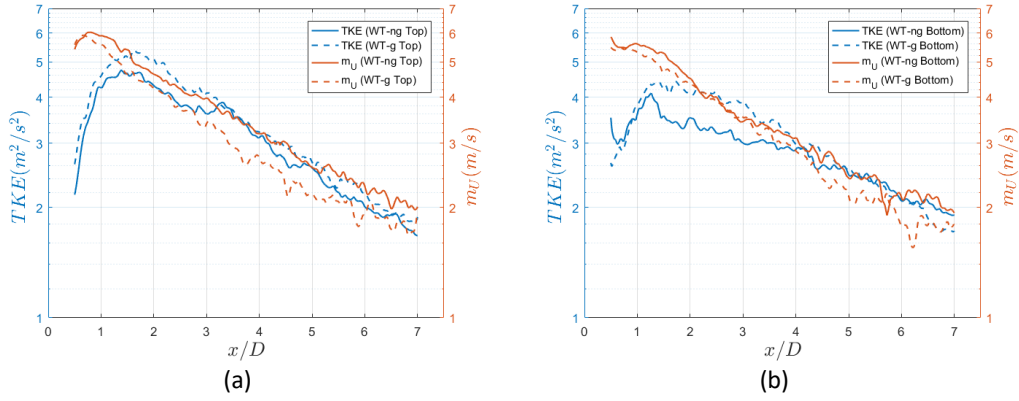
Figure 3.21. Distribution of mean TKE and the square root of wake velocity gradient for the WT-ng and WT-g cases: (a) the top part of the wake, (b) the bottom part of the wake

Figure 3.22 illustrates the distribution of mean turbulent kinetic energy and the square root of wake velocity gradient in the wake of the PD-ng and PD-g cases at both top and bottom wake. Results show that in contrast to the model wind turbine cases, the turbulence downstream the porous disc is significantly influenced by the inflow turbulence. Both the TKE levels and the decay rates do not match in the two cases which have different free stream turbulence intensity levels. Contrary to what one might expect, the PD-ng case is observed to create substantially larger levels of TKE in the bottom part of the wake than the PD-g case. At the top wake, a similar phenomenon is also seen. It is also worth noting that in the near vicinity of the disc, the trends seen in the TKE levels are similar to the trends seen the slopes, suggesting that the turbulence production in this region can be associated with a shear-driven instability.
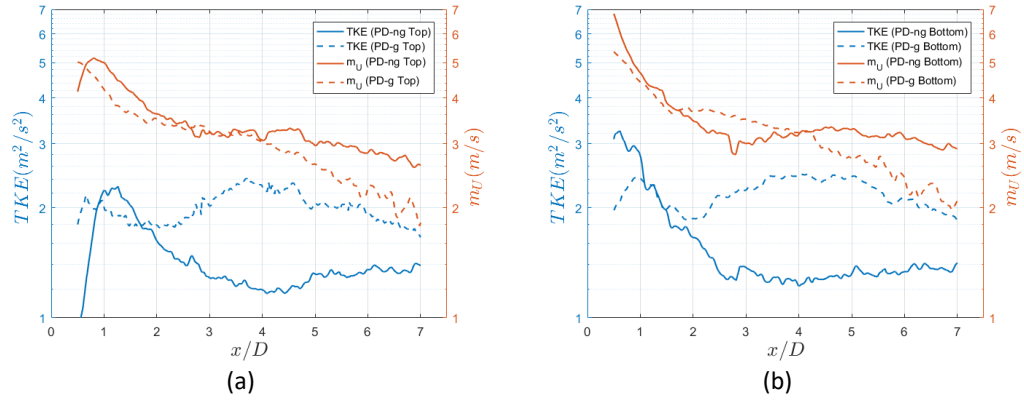
Figure 3.22. Distribution of mean TKE and the square root of wake velocity gradient for the PD-ng and PD-g cases: (a) the top part of the wake, (b) bottom part of the wake

Figure 3.23 presents the decay of mean TKE and the square root of the wake velocity gradient of the WT-ng and the PD-g cases. As mentioned before, it is observed that the wake velocity profiles of the model wind turbine case operating in the low ambient turbulence intensity level (WT-ng) are almost identical to that of the porous disc case which operates in the high ambient turbulence intensity level. However, significant differences can be observed in the normalized turbulent kinetic energy contour plots of these cases. Nonetheless, it can be seen that the distribution and decay rate of both mean turbulent kinetic energy and the square root of wake velocity gradient are comparable, particularly after x/D=4 at both halves of the wake. Furthermore, the correlation between the turbulent kinetic energy and the square root of the wake velocity is evident in both cases. However, regardless of parallelism in the decay characteristics of both quantities downstream in the WT-ng and PD-g cases, the similarity in the wake velocity profiles might be a coincidence and needs more investigation to be proven.
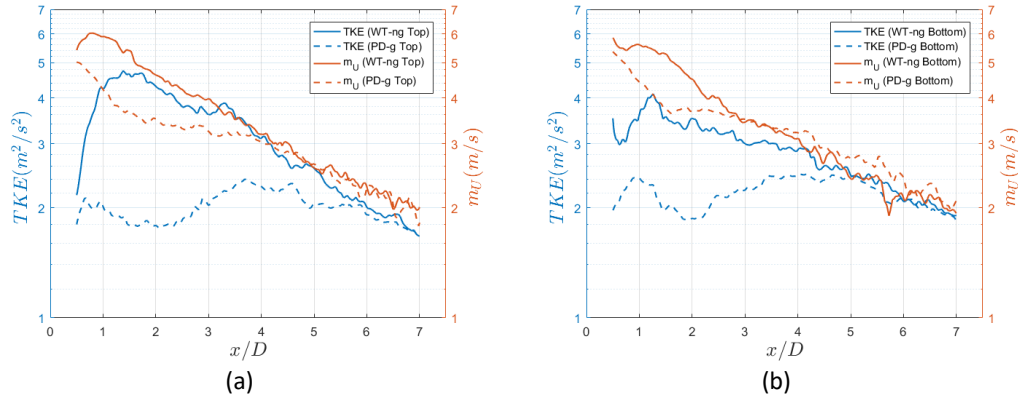
Figure 3.23. Distribution of mean turbulent kinetic energy and the square root of wake velocity gradient for the WT-ng and PD-g cases: (a) the top part of the wake, (b) bottom part of the wake

Results obtained this investigation reveal that turbulent kinetic energy levels are significantly different at the top and bottom part of the wake in the mdel wind turbine cases and especially in the near-wake region, effects of inflow turbulence intensity level is evident. In addition, trends of both TKE and slope are not comparable in the PD-ng and PD-g cases. Thus, despite the similar rate of decay in both the WT-ng and PD-g cases, present results based on planar PIV data which examine only axial and radial flow quantities. In this respect, as future work, to have deeper insight of the three-dimensional effects, an experimental campaign in the traverse plane of the both models through PIV or wake velocity measurements using hot-wire anemometer starting from immediate downstream the models should be conducted. In addition, CFD simulations might be planned to investigate the wake development by dublicating experimental setup of the current thesis study. On the other hand, present findings raise hopes and promise that a turbulent kinetic energy model in the wake of wind turbines or porous discs can be developed based on vertical shear distribution in the wake.

CHAPTER 4

WAKE CHARACTERISTICS OF THE MODEL WIND TURBINE AND THE POROUS DISC OPERATING UNDER BOUNDARY LAYER INFLOW

This chapter presents the boundary layer inflow effects on the wake characteristics of the model wind turbine and the porous disc is presented in terms of the mean wake flow field, wake turbulence, wake decay, and wake spreading characteristics. In addition, Proper Orthogonal Decomposition (POD) analyses are performed using PIV images for further investigation. For the sake of simplicity, hereafter, WT-20, WT-35, WT-45, and WT-75 refer to the model wind turbine cases under boundary layer inflow conditions at $z/\delta=1.12$, $z/\delta=0.67$, $z/\delta=0.52$, and $z/\delta=0.30$, respectively. Similarly, PD-20, PD-35, PD-45, and PD-75 refer to the porous disc cases at $z/\delta=1.12$, $z/\delta=0.67$, $z/\delta=0.52$, and $z/\delta=0.30$, respectively.

4.1 Mean Wake Flow Field

Figure 4.1 shows the normalized streamwise velocity fields in the wake of the model wind turbine and the porous disc at different z/δ positions, namely $z/\delta=1.12$, $z/\delta=0.67$, $z/\delta=0.52$, and $z/\delta=0.30$, up to 7D downstream. Results show that the velocity deficit is higher in the model wind turbine cases compared with the porous disc cases independent of the ambient turbulence intensity in the near-wake region. In addition, wake recovery occurs much faster in the near-wake region, especially between $0.5 \leq x/D \leq 1.5$, for the porous disc cases compared to the model wind turbine cases at every z/δ position. However, in the far wake region, where the effects of tip vortices are not pronounced, the rate of wake recovery is significantly higher in the model wind turbine cases than that of the porous disc cases at every z/δ location.

In the case in which the model wind turbine and the porous disc are outside the boundary layer ($z/\delta=1.12$), where there is no inflow shear effect, one can observe

that mean velocity distributions are fairly symmetrical around the centerline position which is illustrated with the dashed black line passes through the geometrical center of both models despite the fact that there is a slight downward deviation in the model wind turbine case and a slight upward deviation in the porous disc case. However, wakes of the model wind turbine skew downward at $z/\delta=0.67$, $z/\delta=0.52$, and $z/\delta=0.30$ while velocity distribution is symmetrical around $z/D=0$ in the porous disc cases. Furthermore, as merging in z/δ positions, ambient turbulence intensity increases resulting in increasing the wake recovery rates in both the model wind turbine and the porous disc cases.
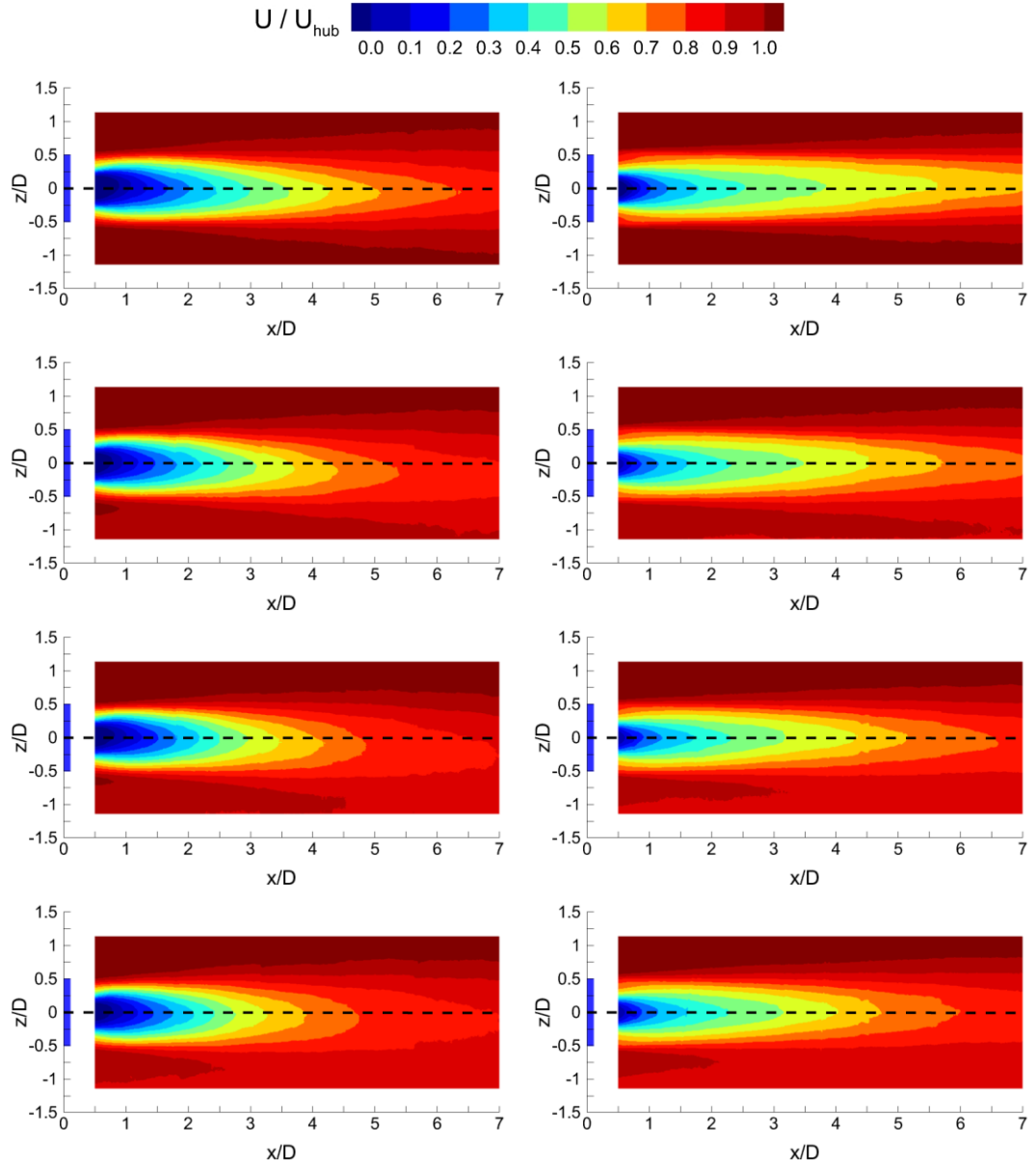
Figure 4.1. Normalized streamwise velocity field of the model wind turbine (left) and the porous disc (right). (First row z/δ=1.12, second row z/δ=0.67, third row z/δ=0.52, fourth row z/δ=0.30). The geometric centerline of the wind turbine/porous disc is presented by the dashed line. The blue rectangular region represents the wind turbine/porous disc located between $-0.5 \leq z/D \leq 0.5$

87
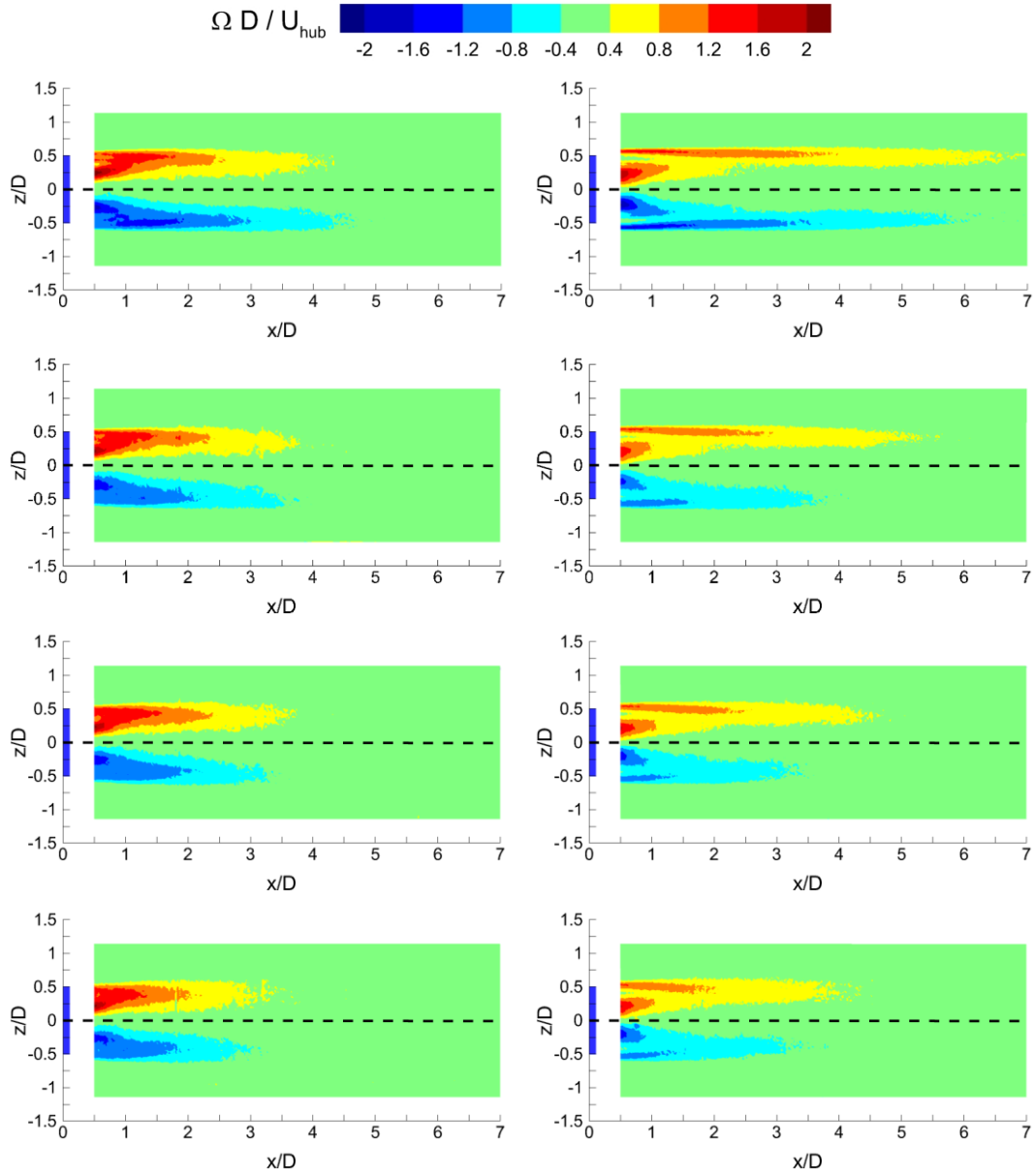
Figure 4.2. Normalized out-of-plane vorticity fields: the model wind turbine (left) and the porous disc (right) (First row z/δ=1.12, second row z/δ=0.67, third row z/δ=0.52, fourth row z/δ=0.30). The geometric centerline of the wind turbine/porous disc is presented by the dashed line. The blue rectangular region represents the wind turbine/porous disc located between $-0.5 \leq z/D \leq 0.5$

Figure 4.2 presents the contours of normalized out-of-plane vorticity downstream of the model wind turbine and the porous disc at different z/δ positions. Results show that the model wind turbine cases have a symmetrical normalized out-of-plane vorticity distribution in terms of extensions of the regions that have the same level while which is not the case for the porous disc. On the other hand, it is evident that out-of-plane vorticity distribution becomes asymmetrical in the model wind turbine cases as one merge within the boundary layer.

Starting with the case outside the boundary layer (z/δ=1.12), one can observe that the wind turbine case has higher out-of-plane vorticity values in the near-wake region compared with the porous disc case. However, higher out-of-plane vorticity levels extend far downstream of the porous disc compared to the model wind turbine, especially after x/D=4 which was the same downstream position shown in the WT-ng case in Chapter 3. Normalized out-of-plane vorticity distributions become asymmetrical as inflow shear is more pronounced as one merge within the boundary layer. Furthermore, due to increasing ambient turbulence intensity, normalized out-of-plane vorticity magnitudes of both the model wind turbine and the porous disc reduce and higher-level regions shrink as the z/δ position decreases. Thus, at z/δ=0.30 (4th row in Figure 6.2), especially after x/D=3, far wake regions downstream the model wind turbine and the porous disc become comparable.
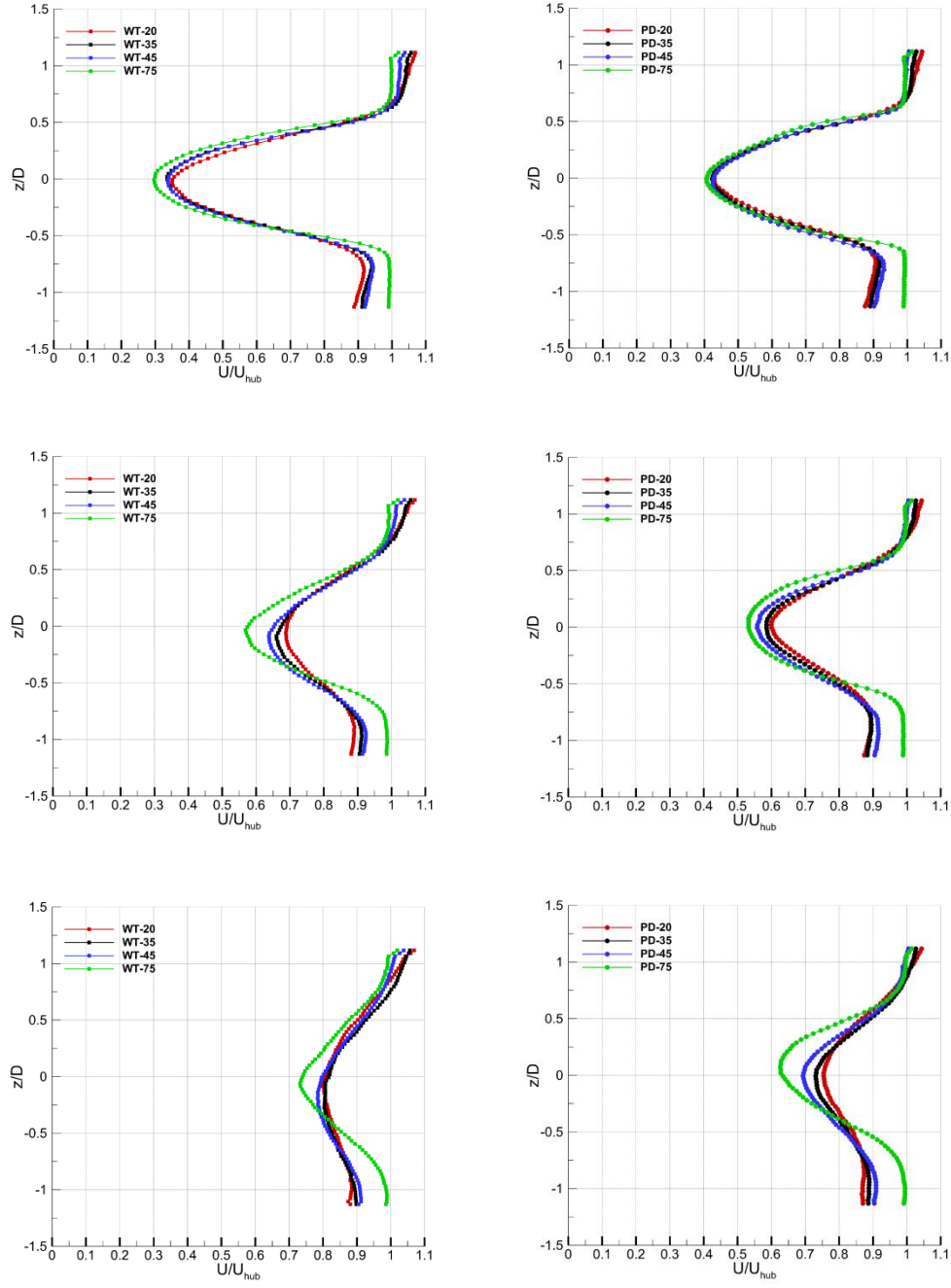
Figure 4.3. Normalized streamwise velocity distributions of the model wind turbine (left) and the porous disc (right) at different downstream positions: x/D=2 (first row), x/D=4 (second row) and x/D=6 (third row). The wind turbine/porous disc is located between $-0.5 \leq z/D \leq 0.5$

90

Figure 4.3 presents the normalized streamwise velocity profiles at x/D=2 (first row), x/D=4 (second row), and x/D=6 (third row) for the model wind turbine and the porous disc at different z/δ positions. Results show that the maximum velocity deficits for the model wind turbine cases are higher than that of the porous disc cases in the near-wake region. On the other hand, since the wake recovery of the model wind turbine is faster than that of the porous disc after the tip vortices breakdown, the maximum velocity deficits in the porous disc cases are higher compared to the model wind turbine cases. In addition, one can further observe that downward deviation of the wake in the model wind turbine cases results in a shift of the minimum velocity points downstream the porous disc with increasing downstream locations, especially after x/D=4. Nonetheless, velocity distributions of the porous disc cases are fairly symmetrical around the centerline position (z/D=0) downstream.

In the near-wake region, at x/D=2, although freestream velocity is smaller than the hub velocity (U/U_{hub}<1) for all cases except the ones at z/δ=1.12, velocity distributions are asymmetrical around z/D=0. In addition, in the model wind turbine cases, velocity deficit decreases as ambient turbulence intensity level increases: therefore, the wake recovery rate increases while the z/δ position decreases. For instance, the minimum velocity in the wake of the model wind turbine at z/δ=1.12 is roughly 25% lower than that of the model wind turbine at z/δ=0.30. On the other hand, an increase in the ambient turbulence intensity seems to have little effect on the velocity profile of the porous disc. At x/D=4, one can observe that the wake of the model wind turbine recovers faster than that of the porous disc, and minimum velocity points move below z/D=0 as a result of the downward deviation of the model wind turbine wakes. To illustrate, the minimum velocity downstream the wake of the model wind turbine is around 21% and 20% higher compared to the porous disc at z/δ=0.52 and z/δ=0.30, respectively. At x/D=6, one can observe that velocity profiles of the model wind turbine cases in the boundary layer (at z/δ=0.52 and z/δ=0.67) collapse onto each other while which is not the case for the porous disc. In addition, these outcomes regarding mean wake flow field characteristics of both models under the effect of boundary layer inflow are consistent with the results obtained by

91

Vermeer [14], Aubrun et al. [17], Lignarolo [18], Chamorro and Porte-Agél [49], [119], Porte-Agél et al. [37] and Li et al. [103].

4.2   Wake Turbulence

Figure 4.4. Normalized mean turbulent kinetic energy fields: (left) the model wind turbine and (right) the porous disc (First row z/δ=1.12, second row z/δ=0.67, third row z/δ=0.52, fourth row z/δ=0.30). The geometric centerline of the wind turbine/porous disc is presented by the dashed line. The blue rectangular region represents the wind turbine/porous disc located between $-0.5 \le z/D \le 0.5$

Figure 4.4 presents the normalized turbulent kinetic energy fields in the wake of the model wind turbine and the porous disc at different locations in the boundary layer (i.e. at different z/δ positions). Results show that turbulent kinetic energy magnitudes in the wake of both the model wind turbine and the porous disc increase as the z/δ position decreases due to increasing ambient turbulence intensity. Furthermore, due to inflow shear effects, turbulent kinetic energy levels increase at the upper part of the wakes as moves deeper into the boundary layer.

Starting with the case outside the boundary layer ($z/\delta=1.12$), one can observe that the porous disc case has a symmetrical turbulent kinetic energy distribution around the wake centerline while the upper part of the wake of the model wind turbine case has a significantly higher turbulent kinetic energy level. Compared with the passive grid turbulence case, one can observe that turbulent kinetic energy distributions outside the boundary layer in the wake of both models are similar. As one merges within the boundary layer, the extension of the higher levels in the near-wake region of the porous disc cases reduces due to increasing ambient turbulence intensity resulting in increasing turbulent mixing. Moreover, especially at $z/\delta=0.52$ and $z/\delta=0.30$, a higher level of turbulent kinetic energy occurs in the upper part of the wake of the porous disc. One can further observe that turbulent kinetic energy levels increase as ambient turbulence intensity increases; hence a production region occurs downstream of the porous disc, and this region extends through the porous disc as the z/δ position decreases.
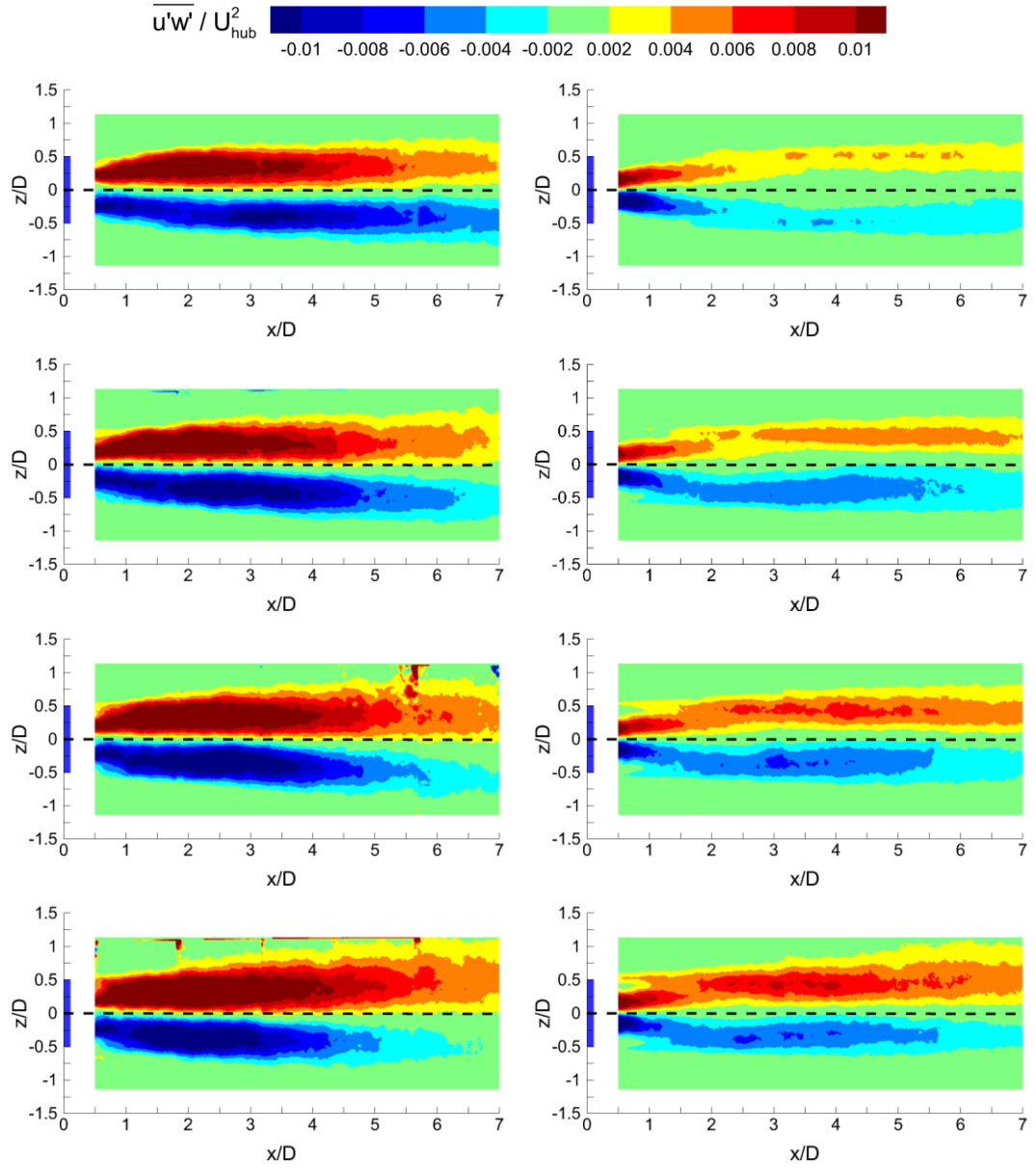
Figure 4.5. Normalized Reynolds shear stress fields: (left) the model wind turbine and (right) the porous disc (First row z/δ=1.12, second row z/δ=0.67, third row z/δ=0.52, fourth row z/δ=0.30). The geometric centerline of the wind turbine/porous disc is presented by the dashed line. The blue rectangular region represents the wind turbine/porous disc located between $-0.5 \leq z/D \leq 0.5$

Figure 4.5 presents the normalized Reynolds shear stress fields in the wake of the model wind turbine and the porous disc at different positions in the boundary layer (i.e. at different z/δ positions). One can observe that the Reynolds stress values in the wake of the model wind turbine are significantly higher than that of the porous disc regardless of the z/δ position. Results further show that the normalized Reynolds shear stress distribution of the porous disc has a symmetrical distribution around the centerline position which is illustrated with the dashed line in the case outside the boundary layer ($z/\delta=1.12$). In addition, higher levels occur in the near-wake region, and they reduce continuously with increasing downstream locations. On the other hand, at the same z/δ position, the upper part of the wake of the model wind turbine has elevated values compared with the lower part.

It is evident that a higher level of the Reynolds shear stress extends to a larger region as both the model wind turbine and the porous disc immersed in the boundary layer results in ambient turbulence intensity level pronouncing more. Moreover, due to inflow shear, the difference between the upper and bottom parts of the wake increases in magnitude.
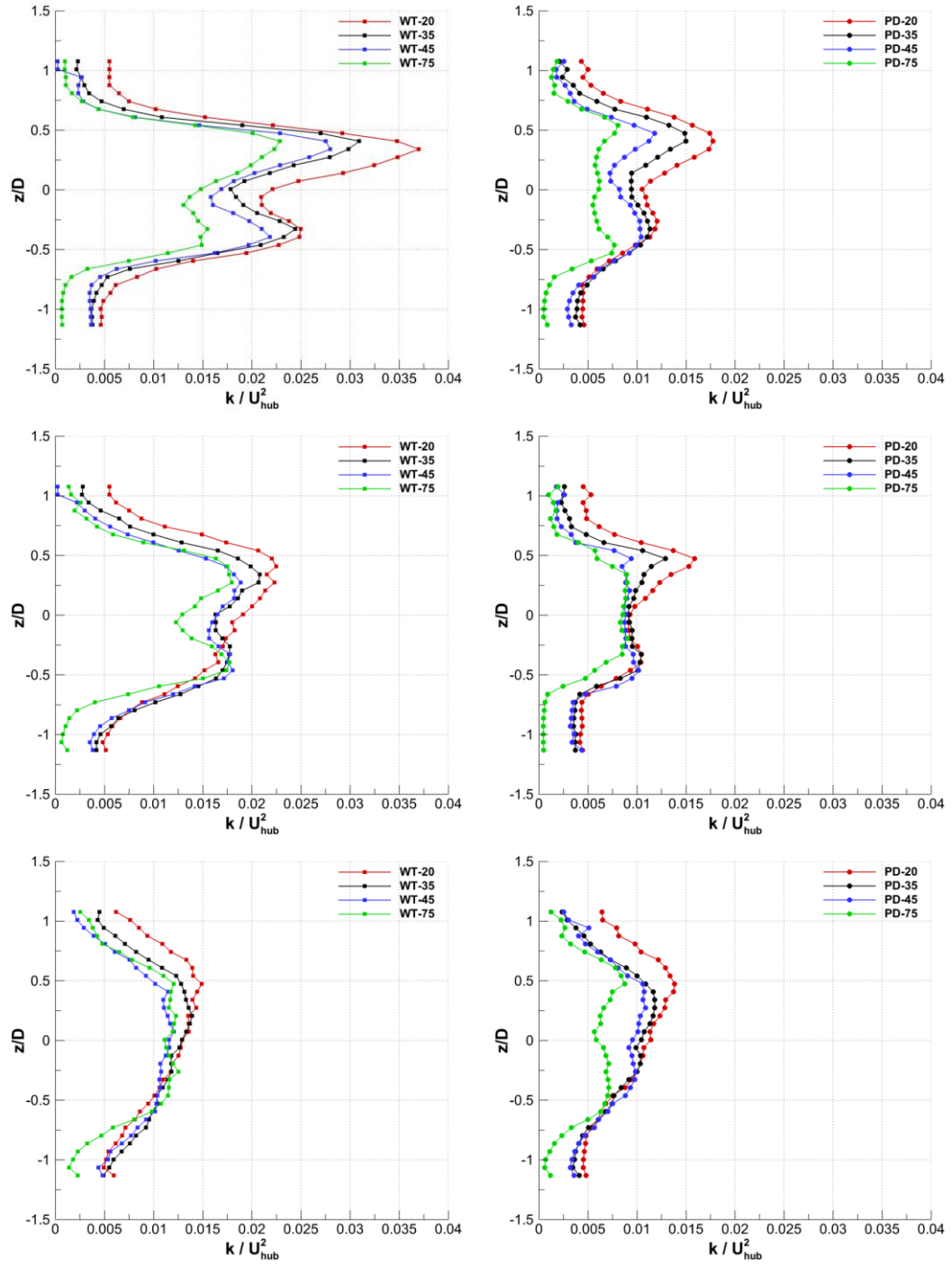
Figure 4.6. Normalized turbulent kinetic energy profiles of the model wind turbine (left) and the porous disc (right) at different downstream positions: x/D=2 (first row), x/D=4 (second row), and x/D=6 (third row). The wind turbine/porous disc is located between $-0.5 \leq z/D \leq 0.5$

Figure 4.6 presents the normalized turbulent kinetic energy profiles for the model wind turbine (left) and the porous disc (right) at x/D=2 (first row), x/D=4 (second row), and x/D=6 (third row) at different positions in the boundary layer (i.e. at different z/δ positions). A fairly symmetrical distribution with a double peak can be observed for both the model wind turbine and the porous disc at x/D=2 and x/D=4. In addition, one can observe the higher peak at the top halves of the wakes (i.e. at z/D≥0), and increasing ambient turbulence intensity levels results in elevated peak values. Results show that the turbulent kinetic energy levels of the model wind turbine are significantly higher than that of the porous disc at x/D=2. For instance, the maximum normalized kinetic energy value in the WT-75 case is two times higher than that of the PD-75 case. Moreover, due to higher ambient turbulent intensity, higher peaks occur as one moves deeper positions within the boundary layer. To illustrate, the maximum normalized kinetic energy in the PD-20 case is 31%, 38%, and 125% higher than PD-35, PD-45, and PD-75, respectively. At x/D=4, differences in magnitude between the model wind turbine and the porous disc cases reduce, particularly the ones at z/δ=0.52 and z/δ=0.30 where the ambient turbulence intensity is relatively higher. On the other hand, the double peaks shape of the distributions vanishes, and except for the porous disc case outside the boundary layer (z/δ=1.12), all turbulent kinetic energy profiles tend to collapse onto each other. In other words, in the far-wake region, all turbulent kinetic energy profiles other than the porous disc out of the boundary layer cease to be similar at x/D=6. For instance, the maximum kinetic energy in the WT-20 case is only 4% higher compared to the PD-20 case.
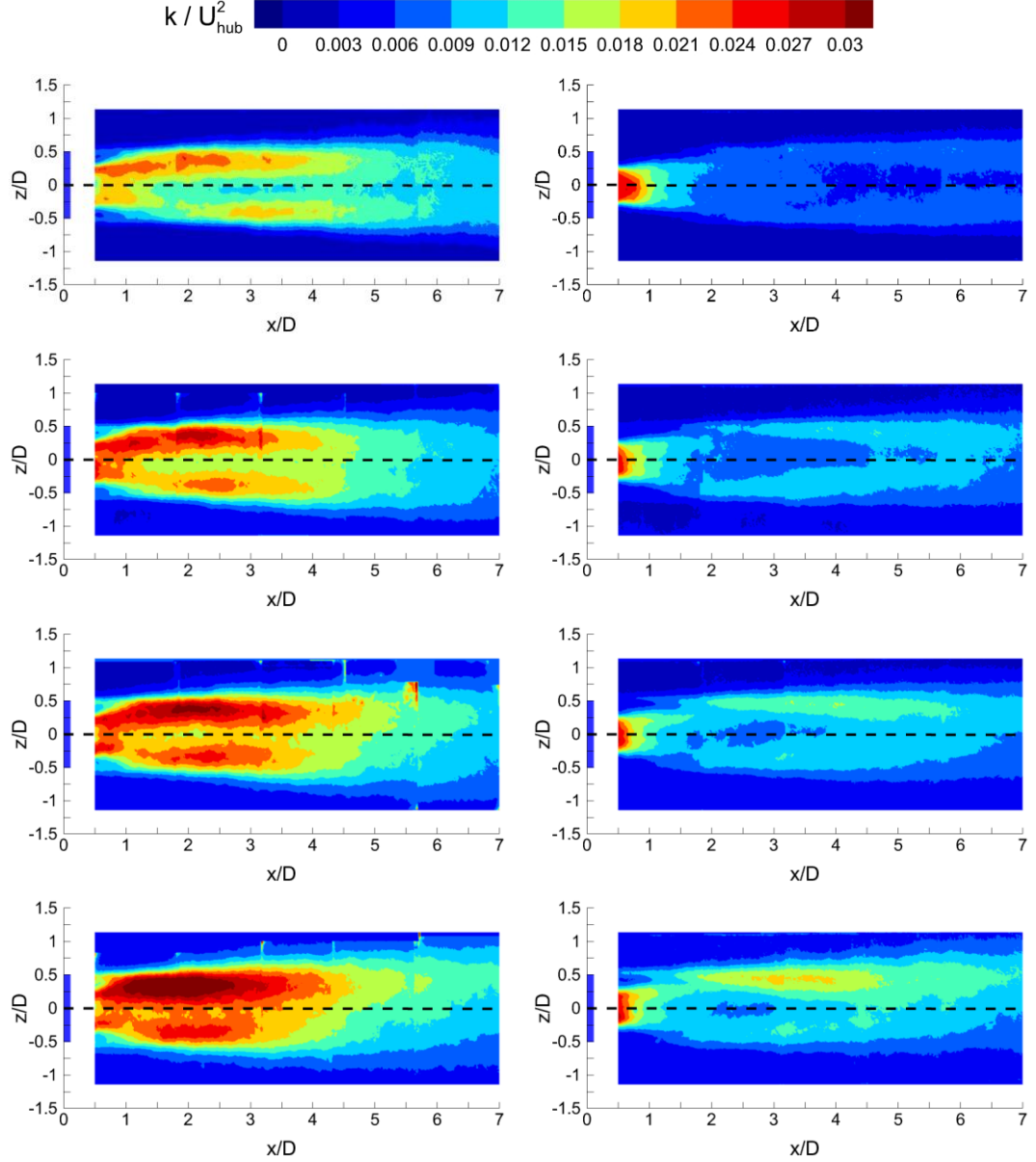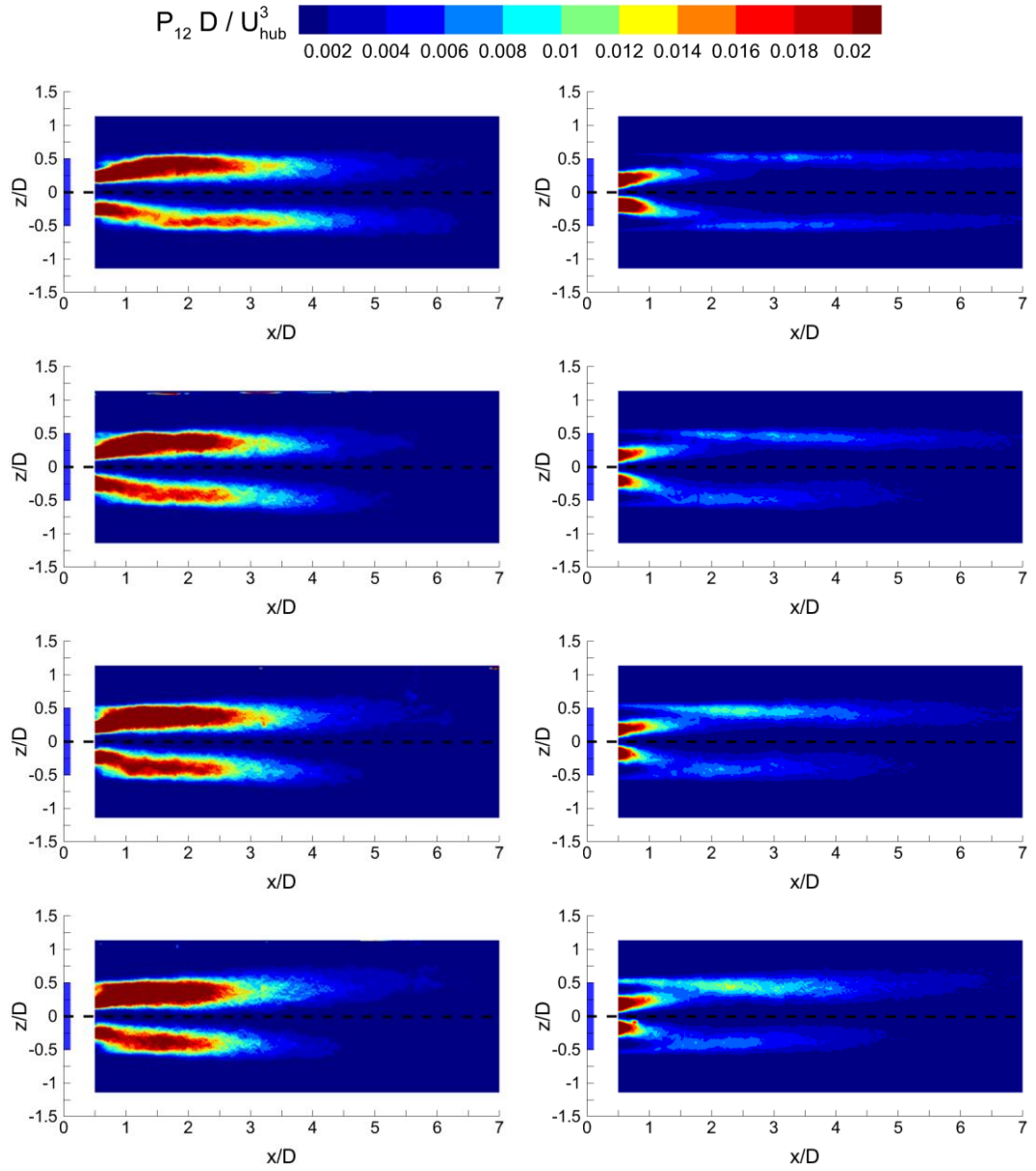
Figure 4.7. Normalized Production (P12) of turbulent kinetic energy fields: (left) the model wind turbine and (right) the porous disc (First row z/δ=1.12, second row z/δ=0.67, third row z/δ=0.52, fourth row z/δ=0.30). Blue rectangular region represents the wind turbine/porous disc located between $-0.5 \leq z/D \leq 0.5$

Figure 4.7 presents the normalized production ($P_{12} = -\overline{u'w'}(dU/dz)$) of turbulent kinetic energy distributions in the wake of the model wind turbine and the porous disc at different positions in the boundary layer (i.e. at different z/δ positions). Starting with the case out of the boundary layer, results reveal that the normalized production of the turbulent kinetic energy has non-symmetrical distribution around the centerline while which is not the case for the porous disc. On the other hand, one can observe that the model wind turbine case has significantly higher levels, particularly in the near-wake region. Furthermore, normalized production distributions cease to be comparable in the far wake region. For instance, maximum levels extend up to x/D=4 in the WT-75 case and they gradually decrease up to x/D=3 as the model wind turbine moves to lower positions within the boundary layer. On the other hand, maximum levels in the PD-75 case are up to x/D=1.5 and it reaches up to x/D=1.25 in the PD-20 case. Furthermore, the effects of the higher ambient turbulence intensity are more pronounced as one merged within the boundary layer in such a way that production of the turbulence levels rises for all the cases, and distribution downstream of the porous disc becomes non-symmetrical. Furthermore, these findings in terms of wake turbulence at boundary layer inflow are consistent with the results obtained by Vermeer [14], Aubrun et al. [17], Lignarolo [18], Chamorro and Porte-Agél [49], [119], Porte-Agél et al. [37] and Li et al. [103].

4.3   Wake Decay Characteristics
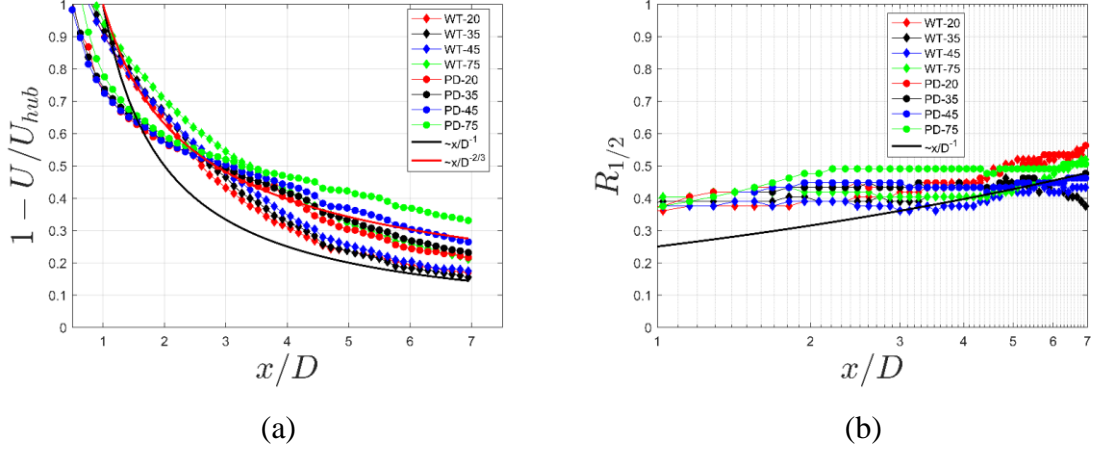
Figure 4.8. (a) Velocity deficit $(1 - U/U_{hub})$ along the geometric centerline at different z/δ positions. (b) Wake half-width for wind turbine and porous at different z/δ positions

Figure 4.8.a presents the wake velocity deficit profiles along the wake centerline of the model wind turbine and the porous disc at different z/δ locations as well as wake decay variations proposed by Johnson et al. [104] and Pope [73]. Results reveal that, except for the PD-75 case ($z/\delta=1.12$), the wake velocity deficit decays for the porous disc cases are proportional to $x/D^{-2/3}$, especially after $x/D=3$. Thus, these results are consistent with Pope [73]. Nevertheless, after $x/D=3$, the wake velocity deficit decays for the model wind turbine cases are proportional to x/D^{-1}, where the results match the experimental study of Johnson et al. [104]. Furthermore, one can observe that velocity deficit profiles cumulate between x/D^{-1} and $x/D^{-2/3}$ after $x/D=6$, where velocity distributions become comparable.

Figure 4.8.b shows the wake half-width distribution downstream of the model wind turbine and the porous disc introduced by Pope [73]. Results indicate that wake of both modes at the same z/δ positions has similar half-width values. Furthermore, the growth of the wake half-width is proportional to $x/D^{1/3}$ which is typical behavior for axisymmetric wake [73].

(a)	(b)
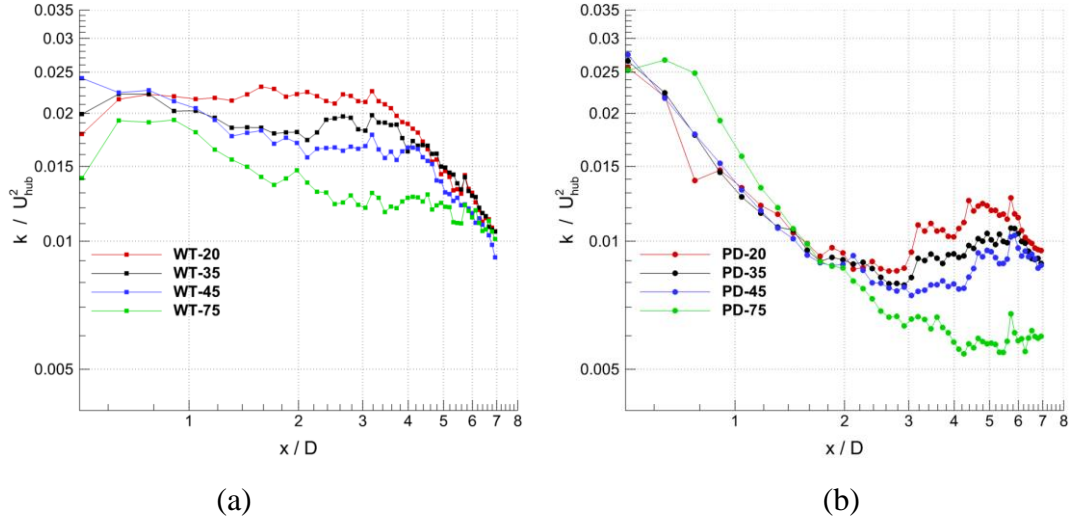
Figure 4.9. Decay of normalized turbulent kinetic energy of (a) the model wind turbine, (b) the porous disc along the geometric centerline at different z/δ positions

Figure 4.9 illustrates the decay of normalized turbulent kinetic energy along the geometric centerlines ($z/D = 0$) in the streamwise direction. Results show that the porous disc case outside the boundary layer has higher levels of turbulent kinetic energy compared to other porous disc cases up to x/D=2. Between 3≤x/D≤6, a production region occurs downstream of the porous disc cases while which is not the case for the PD-75 case. Downstream these production regions, the turbulent kinetic energy of the three porous disc cases (at z/δ=0.52, z/δ=0.67, and z/δ=1.12) starts to reduce gradually at a constant rate. On the other hand, except for the case outside the boundary layer, a slight decrease occurs between 0.5≤x/D≤3 for the model wind turbine cases, and then the turbulent kinetic energy reduces with the constant rate which is the same with the porous disc cases mentioned hereinbefore. Thus, one can observe that the turbulent kinetic energy distributions for all cases other than the porous disc case outside the boundary layer start to collapse onto each other in the far wake region.
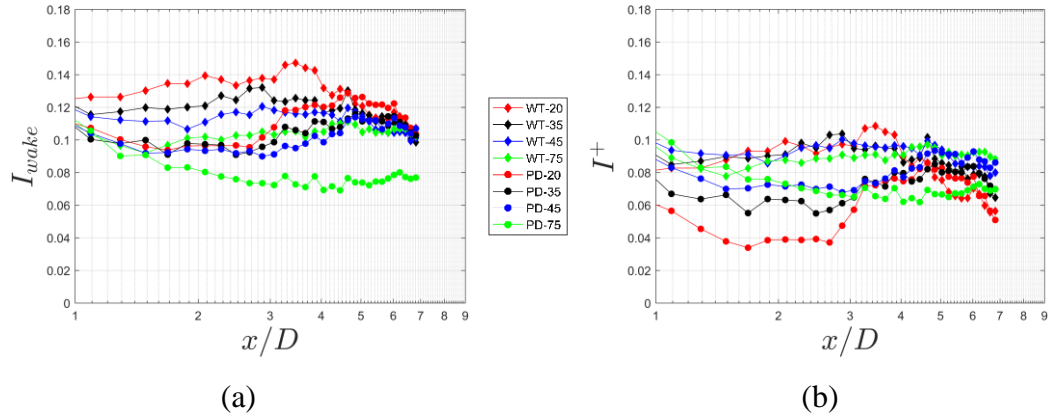
Figure 4.10. Wake turbulence intensity (a) and added turbulence intensity (b) downstream of the model wind turbine and the porous disc at different z/δ positions

Figure 4.10 presents (a) the wake turbulence intensity and (b) the added turbulence intensity along wake centerlines ($z/D = 0$) in the streamwise direction. Figure 4.10.a shows that wake turbulence intensity levels are higher for the model wind turbine cases compared to the porous disc cases. Additionally, higher ambient turbulence intensity effects, especially between 1.5≤x/D≤5, are evident in terms of increased wake turbulence intensity values. A production region can be seen in the porous disc cases after x/D=3. Furthermore, while an increase occurs in the PD-ng case, the wake turbulence intensity levels for the WT-ng, WT-g, and PD-g cases decrease at similar rates after x/D=4.5. Furthermore, after x / D = 5, the turbulence intensity levels of the wake turbulence for all the cases have similar values except for the WT-75 case.

Furthermore, similar to the turbulent kinetic energy profiles, the added turbulence profiles of the WT-g, WT-ng, and PD-g cases collapse after x/D = 4.5, although they have different levels of wake turbulence intensity. Such observations further support the claim that a porous disc requires a certain level of ambient turbulence intensity level to reproduce the wake of a model wind turbine properly. Furthermore, it can be seen that the increase in ambient turbulence intensity has an insignificant influence on the added turbulence in the wake of the model wind turbine.

4.4 Wake Spreading Characteristics

(a)   (b)
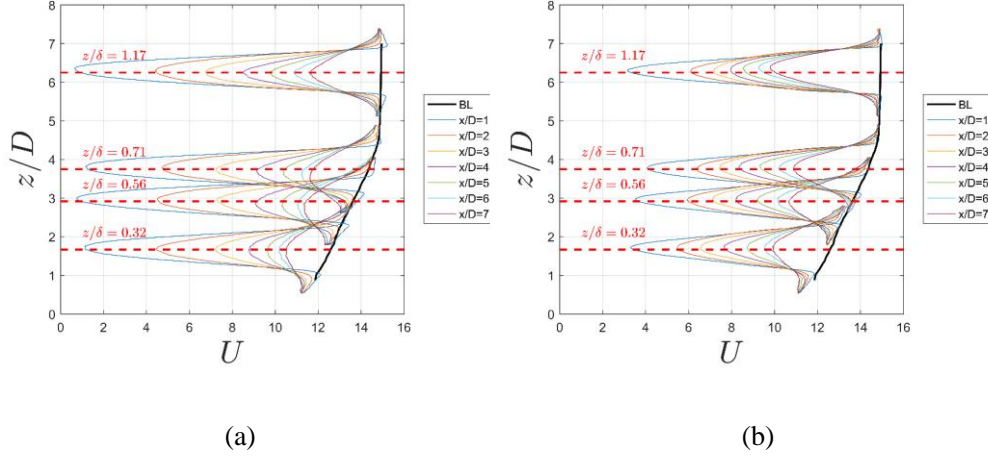
Figure 4.11. (a) Velocity profiles in the wake of the model wind turbine and (b) the porous disc

Figure 4.11 presents the velocity distribution downstream of the model wind turbine and the porous disc as well as the inflow boundary layer. One can observe that velocity profiles are skewed due to inflow shear. Hence it is not precise to calculate the wake growth rate and the initial wake width using Equations (3.28) and (3.29) which assume the wake velocity profile downstream of the wind turbine is Gaussian. Thus, to calculate the wake growth rate and the initial wake width, the inflow boundary layer velocity profile is subtracted from the wake velocity profiles of all cases, and axisymmetric velocity profiles are obtained which are shown schematically in Figure 4.12.
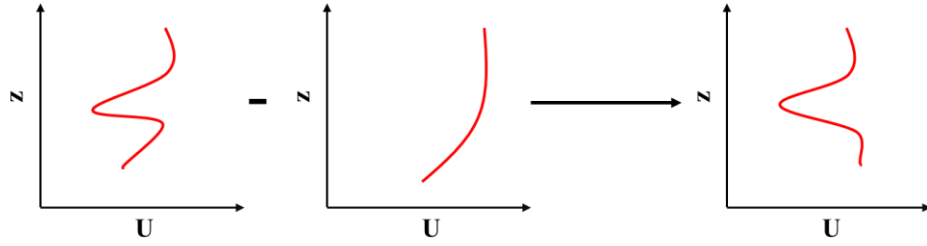
Figure 4.12. Sketch of subtraction process to obtain symmetrical wake profile downstream the model wind turbine and the porous disc
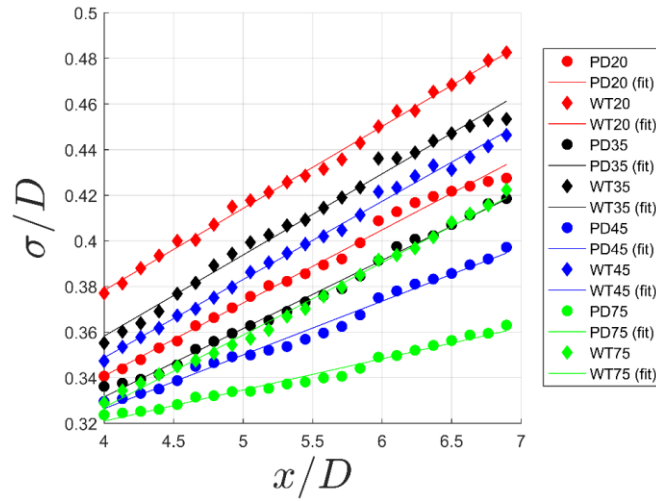
Figure 4.13. Variation of the normalized standard deviation (i.e. wake width) of the velocity deficit profiles for the wind turbine and porous disc along the streamwise direction with curve fits to obtain k^* and ϵ.

The values of wake growth rate and initial wake width for both models under different ambient turbulence intensity level conditions are tabulated in table 6.1. After subtracting the boundary layer profile, similar to passive grid cases, the wake growth rate and the initial wake width values are obtained using equation (3.2) and equation (3.3), and linear curve fitting is employed to wake velocity profiles started from x/D=4.

Table 4.1 $k*$ and ϵ for the wind turbine and the porous disc

Test Cases	Wake growth rate, k^*	Initial wake width, ϵ
PD-20	0.0320	0.2206
WT-20	0.0365	0.2144
PD-35	0.0299	0.2218
WT-35	0.0356	0.2159
PD-45	0.0236	0.2322
WT-45	0.0343	0.2116
PD-75	0.0137	0.2663
WT-75	0.0318	0.1999

Table 4.1 show that the wake growth rate values of the model wind turbine are higher compared to that of the porous disc at each z/δ position. On the other hand, similar to the passive turbulence cases, the difference between the model wind turbine and the porous disc in terms of wake growth rate value decreases as ambient turbulence intensity increases. For instance, at z/δ=1.12 the wake growth rate of the model wind turbine case is 132% higher than that of the porous disc case while the wake growth rate of the model wins turbine case is only 14% higher compared to the porous disc case at z/δ=0.30. Furthermore, initial wake width values of the porous disc under both ambient turbulence intensity conditions are higher than the model wind turbine cases, and the initial wake width of the wind turbine cases does not significantly alter, particularly after z/δ=0.52, as z/δ positions decrease while initial wake width of the porous disc cases decreases. In addition, one can observe that increasing ambient turbulence intensity has less influence on the initial wake width for the model wind turbine compared with the porous disc. To illustrate, although the initial wake width of the model wind turbine increases roughly 5%, the initial wake width of the porous disc cases decreases by 20% as they move from outside the boundary layer (z/δ=1.12) to the lowest measurement position in the boundary layer (z/δ=0.30)

which results in 16 times increase in ambient turbulence intensity. This implies the effect of inherent differences between the wake development characteristics of the wind turbine and the porous disc, especially in the near-wake region.

Figure 4.14 presents the variation of wake growth rate and initial wake width of the model wind turbine and the porous disc under boundary layer inflow conditions. Results reveal that the wake growth rate of the model wind turbine is higher compared with the porous disc under boundary layer inflow conditions similar to grid turbulence conditions. Furthermore, as z/δ increases (both model positions are elevated regarding the bottom wall within the boundary layer) and ambient turbulence intensity decrease the wake growth rate of both the model wind turbine and the porous disc decrease. On the other hand, the initial wake width of the porous disc increases as the model rise within the boundary layer, and ambient turbulent intensity decreases while the initial wake width of the model wind turbine slightly decreases. One can further observe that both parameters converge to a single profile as the ambient turbulent intensity increases (i.e. as one merges within the boundary layer).
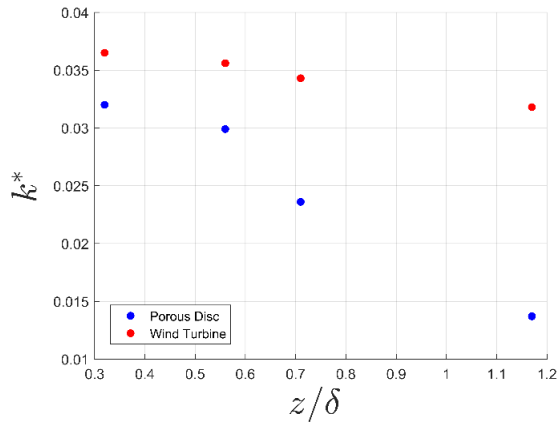
(a)
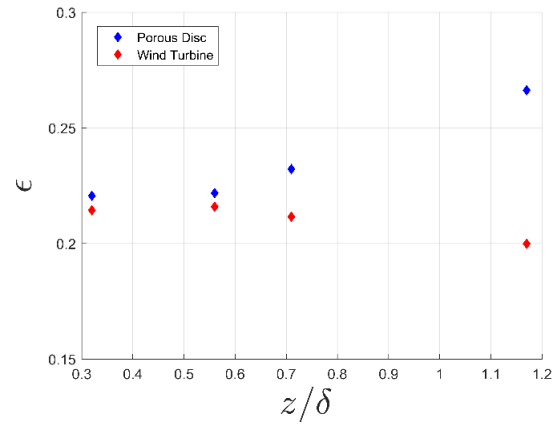
(b)
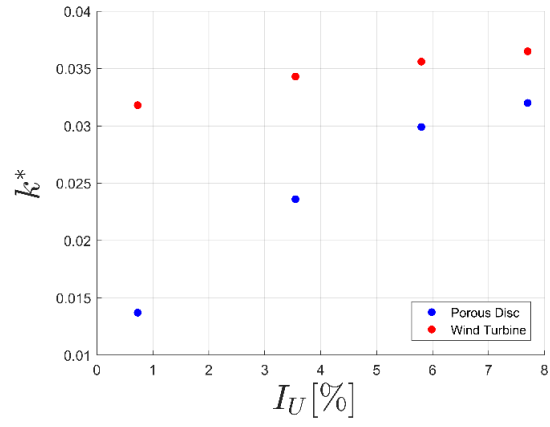
(c)
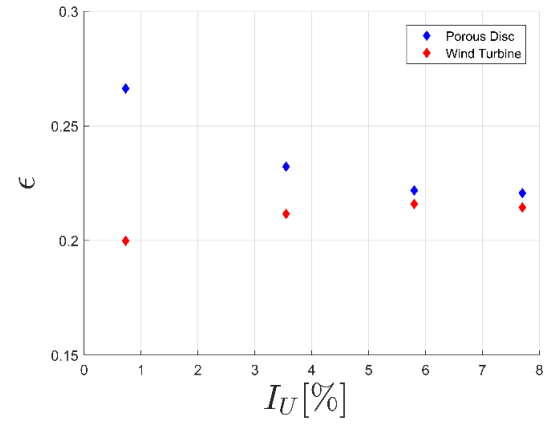
(d)

Figure 4.14. Variation of wake growth rate (a-c) and initial wake width (b-d) with vertical positions within the boundary layer and ambient turbulence intensity

4.5   Proper Orthogonal Decomposition (POD) Analysis

4.5.1   Results
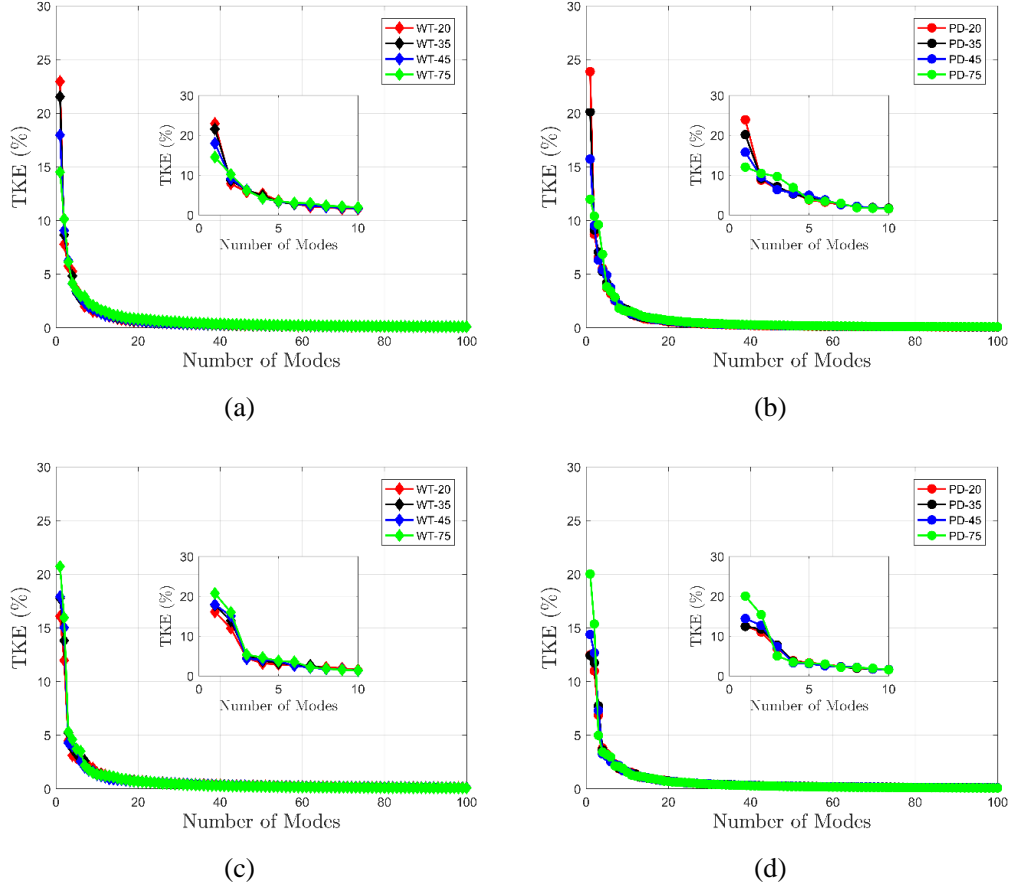
Figure 4.15. Comparison of percentage of turbulent kinetic energy (TKE) attributed to eigenvalues of first 100 modes in the near-wake of the model wind turbine and porous disc at various locations within the boundary layer: (a) the model wind turbine axial velocity (U), (b) the porous disc axial velocity (U), (c) the model wind turbine radial velocity (W), (d) the porous disc radial velocity

Figure 4.15 presents the comparison of the percentage of the TKE associated with eigenvalues of the first 100 modes based on streamwise (a-b) and radial (c-d) velocities in the near-wake region (0.5≤ x/D≤ 1.5) which are sorted from highest to lowest in magnitude obtained by Proper Orthogonal Decomposition (POD) analysis of the model wind turbine and the porous disc at different positions within the boundary layer. Results reveal that the cases at the lowest position within the boundary layer (WT-20 and PD-20) have the highest percentage of the first streamwise component of POD mode. In addition, one can observe that the percentage of the first mode decrease as the position within the boundary layer increase. However, the percentages of TKE become similar after 2th mode for the model wind turbines and 4th mode for the porous disc cases. However, the percentage of TKE of the first vertical component reduces as the model wind turbine and the porous disc merges within the boundary layer. Furthermore, the percentages of TKE become similar after 3th mode for the model wind turbines and 4th mode for the porous disc cases.
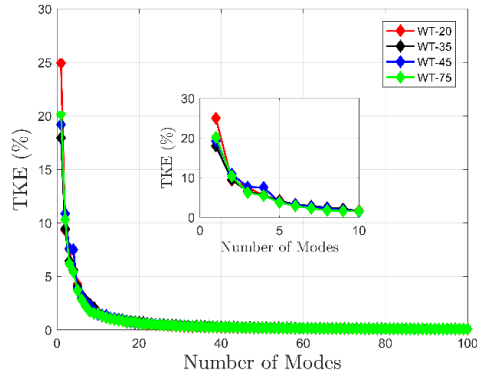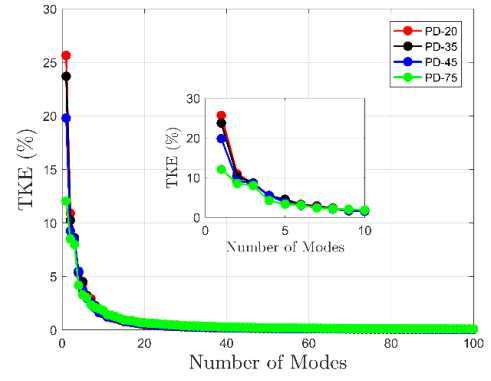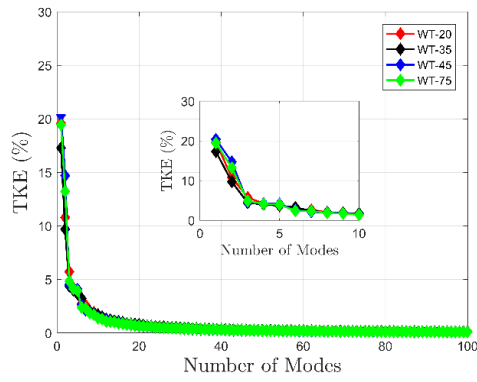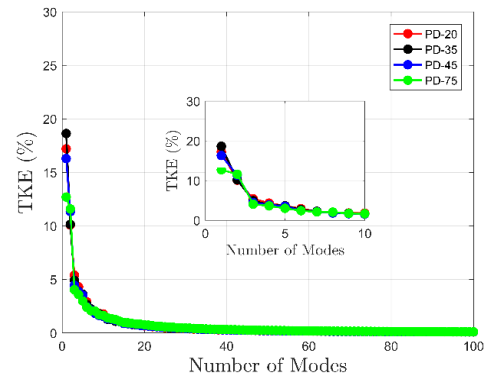
Figure 4.16. Comparison of percentage of turbulent kinetic energy (TKE) attributed to eigenvalues of first 100 modes in the far wake of the model wind turbine and porous disc at various locations within the boundary layer: (a) the model wind turbine axial velocity (U), (b) the porous disc axial velocity (U), (c) the model wind turbine radial velocity (W), (d) the porous disc radial velocity (W).

111

Figure 4.16 presents the comparison of the percentage of the TKE associated with eigenvalues of the first 100 modes based on streamwise (a-b) and radial (c-d) velocities in the far wake region (4.3≤x/D≤5.75) which are sorted from highest to lowest in magnitude obtained by Proper Orthogonal Decomposition (POD) analysis of the model wind turbine and the porous disc at different positions within the boundary layer. Results show that similar to near-wake analysis, the cases at the lowest position within the boundary layer (WT-20 and PD-20) have the highest percentage of the first streamwise component of POD mode. In addition, one can observe that the percentage of the first mode for the porous disc cases decrease as the position within the boundary layer increase. However, the percentages of the first streamwise component of POD modes for WT-35, WT-45, and WT-75 are similar. Furthermore, percentages of the vertical component of all POD modes are similar in model wind turbine cases while there are differences in the PD-75 case up to 3th the mode in the porous disc cases.
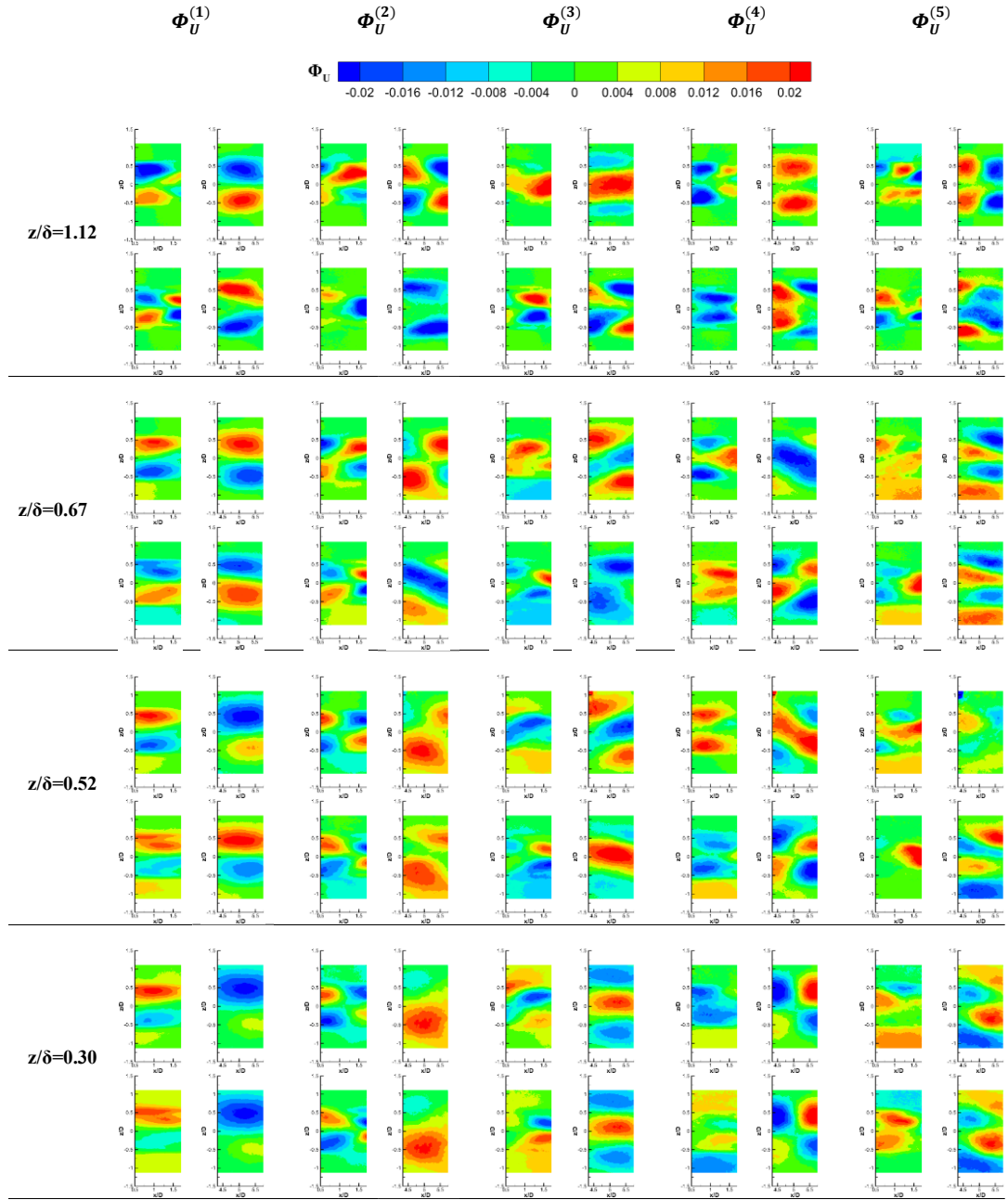
Figure 4.17. POD streamwise components (Φ_U) of first 5 modes in the near-wake (left plots on the column) and the far-wake (right plots on the column) of the model wind turbine (top) and porous disc (bottom) at different boundary layer height positions.
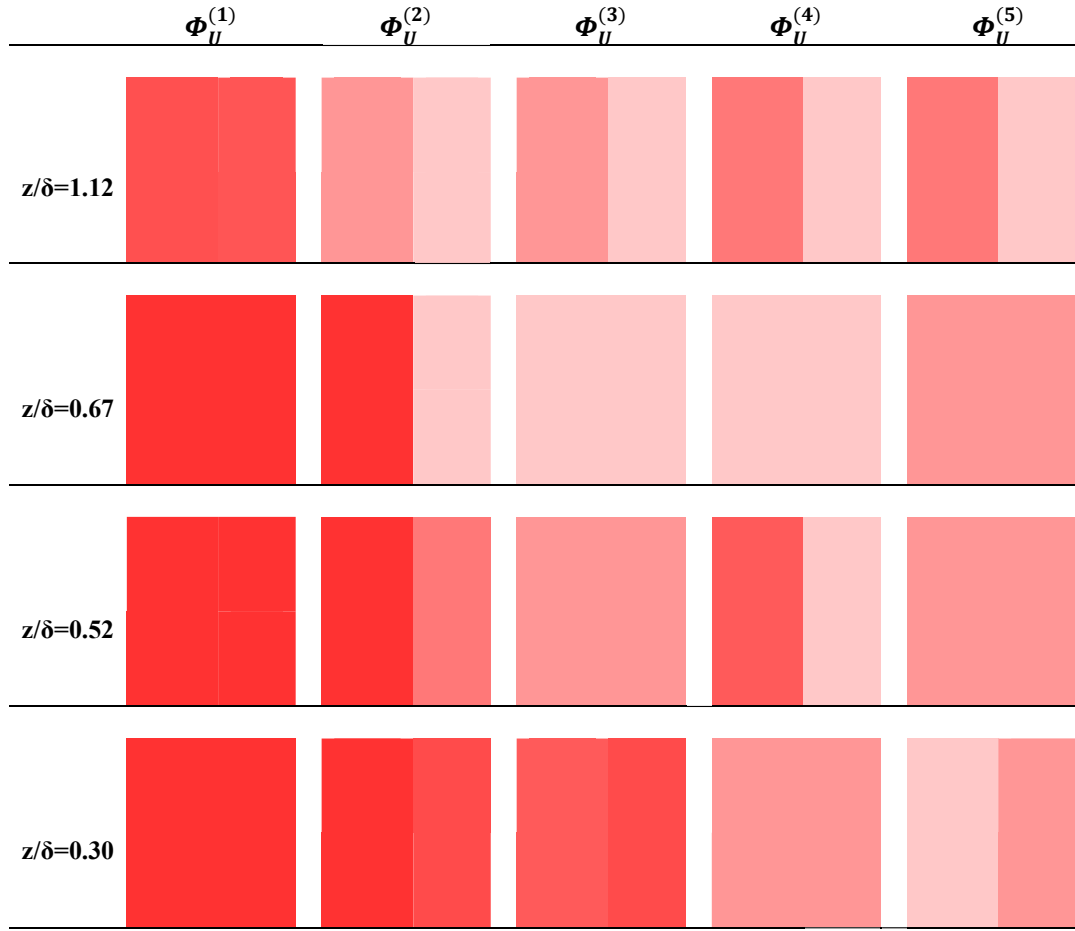
Figure 4.18. near-wakeSimilarity map based on the scaling of the absolute value of normalized cross-correlation of the streamwise components of the POD modes of model wind turbine and the porous disc at the same downstream positions.

Figure 4.17 presents streamwise components of the first five POD modes of both models in the near-wake region at different depths within the boundary layer. POD modes of the model wind turbine cases are represented by the top contour plots and that of porous disc cases are illustrated at the bottom plots on each row. Starting with the porous disc cases, one can observe that the first mode of the PD-75 case is different than that of the other porous disc cases. However, all first five streamwise components of the POD modes of the model wind turbine look similar regardless of sign and order changes. When comparing the first five modes of the model wind

114

turbine and the porous disc, it can be observed that coherent structures which are the parts of the mean turbulent flow cease to become similar as both the model wind turbine and the porous disc merge within the boundary layer results in increasing ambient turbulence intensity.

To illustrate the similarity of the components of the POD modes of the model wind turbine and porous disc cases at various boundary layer heights, absolute values of the inner products of corresponding modes are calculated. Figure 4.18 presents a similarity matrix that is generated using shades of red in which red corresponds to most similar modes and the color gets lighter as the similarity between the modes of both the model wind turbine and the porous disc reduces. Similarity between two modes are obtained by calculating absolute of normalized cross-correlation between modes of the model wind turbine and the porous disc. Results show that the similarity between the rotor and the porous disc cases increases as both models move lower locations within the boundary layer.
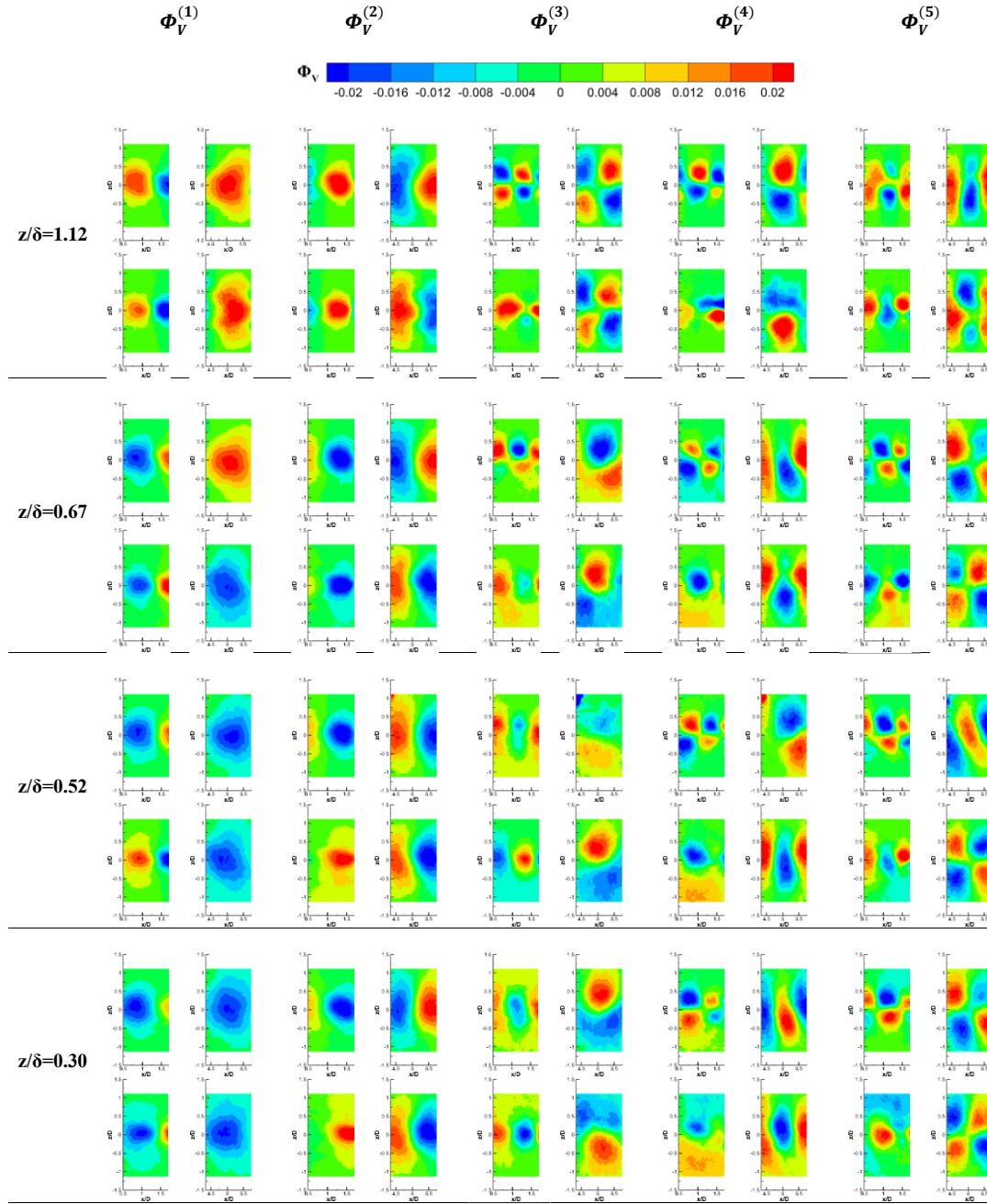
Figure 4.19. POD radial components (Φ_V) of first 5 modes in the near-wake (left) and the far-wake (right) of the model wind turbine (top) and the porous disc (bottom) at different boundary layer height positions.

116
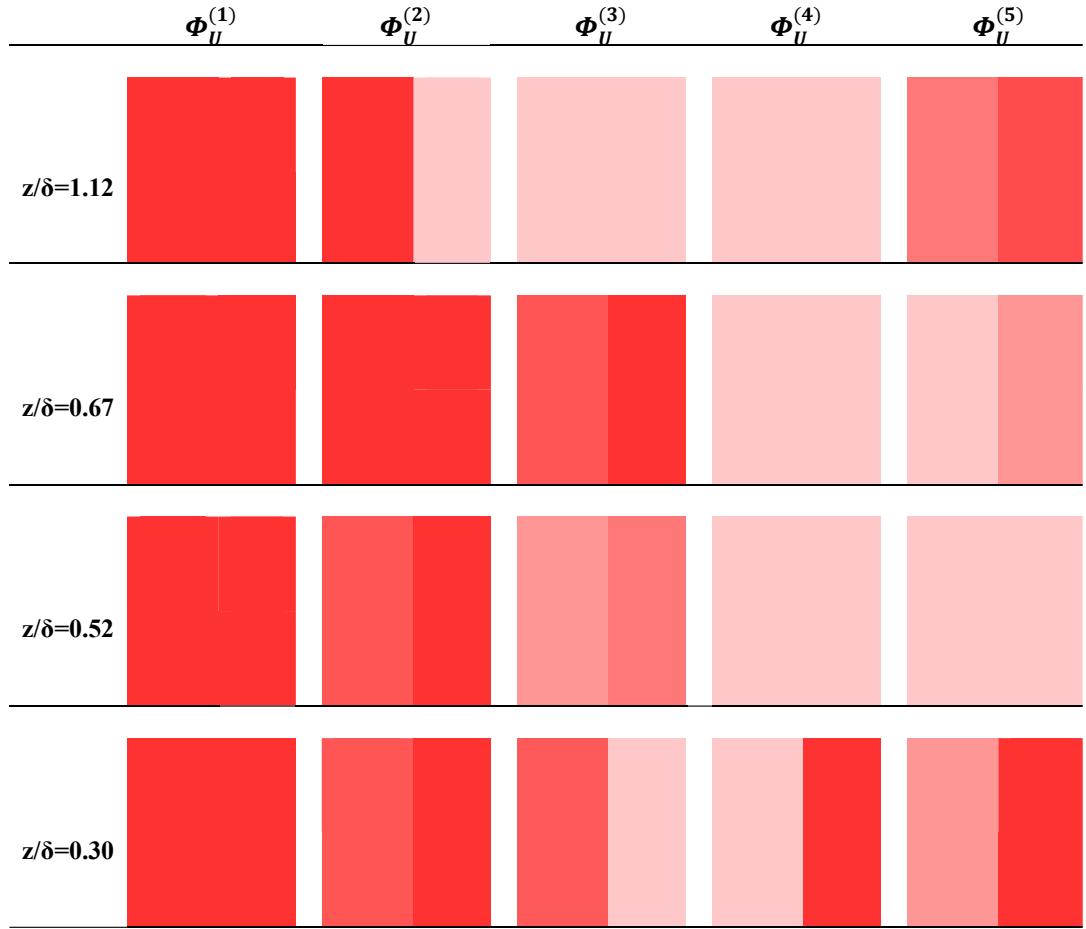
Figure 4.20. Similarity map based on the scaling of the absolute value of normalized cross-correlation of the radial components of the POD modes of model wind turbine and the porous disc at the same downstream positions. near-wake

Figure 4.19 presents streamwise components of the first five POD modes of the model wind turbine and the porous disc in the far wake region at different depths within the boundary layer. In the porous disc cases, it can be observed that the first five modes of all porous disc cases except 3th and 4th modes of the PD-75 case are fairly comparable. In addition, results show that the first two modes of the model wind turbine cases look similar while the ones of the WT-75 case are different after 2nd mode. Similar to streamwise components in the near-wake region, radial

components of the first five POD modes of both models become similar as they merge in the boundary layer.

Figure 4.20 presents the similarity of each mode at different heights in the boundary layer and compares them in terms of the inner products of the modes as described before. Similar to similarity results in the near-wake region, similarity increases as ambient turbulent intensity increases.

Both streamwise and radial components of POD modes also can be seen in Appendix A.

CHAPTER 5

CONCLUSIONS

In this study, wake measurements are conducted to investigate the ambient turbulence intensity effects on the wake development of the wind turbine in terms of the mean flow field, turbulence, wake decay characteristics, and wake spreading characteristics through 2D2C PIV. Furthermore, the wake development characters of the model wind turbine and a matched porous disc are compared under the same inflow conditions. In this respect, three different inflow conditions are simulated in the wind tunnel test section, namely uniform inflow with low turbulence intensity, passive grid turbulence inflow and boundary layer inflow.

The main conclusions can be listed below:

- Wake generation occurs immediately downstream of the model wind turbine and the porous disc due to momentum extraction from the inflow. Velocity distribution is axisymmetric around the centerline which passes through the hub level of both models (i.e. centerline of the test section) under the turbulence grid conditions. In addition, it is evident that wake velocity deficit is higher in the model wind turbine cases than in the porous disc cases at both ambient turbulence intensity levels. One can also observe that the rate of wake recovery is higher for the porous disc cases in the near-wake region; however, after tip vortices breakdown, the wake of the model wind turbine recovers faster compared to the one for the porous disc in the far-wake region. Outcomes further indicate that, for all cases, the rate of wake recovery increases as ambient turbulence intensity increases.

- Vorticity values in the wake of the model wind turbine at low ambient turbulence intensity are higher in terms of magnitude and extend to a larger area in the near-wake region. However, the vorticity field in the wake of the

119

porous disc is formed like a sheet at the tip locations and extends to a farther downstream distance. In addition, when ambient turbulence intensity is higher, differences in terms of vorticity magnitude are still evident but vorticity distributions become comparable, and the signature of the vorticity does not present after x/D=3.5 in the wake of both models.

- When comparing extracted velocity profiles at various downstream locations, one can conclude that similar results with obtained from the velocity distribution contours. In addition, particularly after x/D=4, it is easy to observe that the wake velocity profiles of the WT-ng and PD-g cases are almost identical. This indicates that to reproduce the far-wake characteristics of the model wind turbine at a low ambient turbulence intensity level, the porous disc should be operated at a high ambient turbulence intensity level under turbulence grid conditions.

- Due to the asymmetrical Reynolds shear stress distributions in the wake of both models, which are accountable for kinetic energy transport and entrainment process, the turbulence kinetic energy and its production distributions are asymmetrical with respect to the centerline which is not the case for the porous disc. In addition, the Reynolds shear stress levels increase as ambient turbulence intensity increases. Furthermore, due to differences between the wake development mechanisms especially in the near-wake region and the added turbulence, elevated levels of the Reynolds shear, the turbulent kinetic energy, and the production of the turbulent kinetic energy extend to larger regions in the model wind turbine cases. Furthermore, similar to wake velocity profiles, the the Reynolds shear, the turbulent kinetic energy, and the production of the turbulent kinetic energy distributions of WT-ng and PD-g are similar.

- In terms of wake decay characteristics, wake velocity deficit profiles of the WT-ng, the WT-g, and the PD-g cases along the centerline lay down between two trend lines proposed by Pope [73] and Johnson et al. [104] except for the PD-ng case. Similar observation can be obtained from the turbulent kinetic

energy profiles in the far-wake region which indicates that the turbulent kinetic energy distribution along the centerline in the PD-ng case is different from that of the other cases. Furthermore, it is also evident that the wake turbulence intensity and the added turbulence intensity profiles become comparable in the far-wake region except in the PD-ng case. Nevertheless, estimated wake half-width values for both the model wind turbine and the porous disc are comparable in the far-wake region.

- Predictions of the wake growth rate and the initial wake width of both models under grid turbulence inflow conditions reveal that increase in the ambient turbulence intensity results in increasing the wake growth rate of the model wind turbine wake, however, it does not have a significant influence on the initial wake width. On the other hand, the wake growth rate of the porous disc increases, and the initial wake width decreases significantly with increasing the ambient turbulence intensity.

- POD analysis reveals that both streamwise and vertical components of modes become more comparable as the ambient turbulence intensity levels increases in both the near-wake and the far-wake region. Furthermore, it is worth noting that the first streamwise components of the POD modes are quite similar in shape excluding color shift in the fifth mode.

- Under boundary layer inflow conditions, due to shear, velocity distribution becomes asymmetrical as both models are immersed in deeper positions within the boundary layer. In addition, it is evident that the wake velocity deficit is higher in the model wind turbine cases in comparison with the porous disc cases, especially in the near-wake, however, the wake velocity deficit reduces as both models move into lower positions where the effect of ambient turbulence intensity is more pronounced. Furthermore, one can observe that wake shifts down in the model wind turbine cases except the one outside the boundary layer which is not the case for the porous disc cases.

- Similar to turbulence grid cases, vorticity levels show elevated values in the near-wake of the model wind turbine compared to that of the porous disc. On

the other hand, the extent of the non-zero vorticity region is larger in the porous disc while which is not observable after the tip vortices breakdown in the model wind turbine case. As one moves toward lower positions within the boundary layer, results reveal that vorticity values at the top part of the wake become higher compared to the lower part due to inflow shear. In addition, vorticity distributions become comparable at the lowest position within the boundary layer of the current study where the ambient turbulence intensity is the highest.

- Velocity profiles at several downstream positions show that velocity distributions are similar for the porous disc cases in the near-wake region while noteworthy differences can be seen in the wind turbine cases. On the contrary, velocity profiles become similar in the far-wake region for the model wind turbine cases while which is not the case for the porous disc. Furthermore, minimum velocity positions shift down at the far-wake region resulting in skewed velocity profiles for the model wind turbine cases.

- The turbulent kinetic energy, the Reynolds shear stress, and the production of the turbulent kinetic energy distributions become highly asymmetrical as both the model wind turbine and the porous disc are immersed within the boundary layer. Moreover, these distributions become comparable in the far-wake region after $x/D=4$ as they move deeper to lower positions in the test section.

- Similar to the passive turbulence grid case, velocity deficit profiles along the centerline lay down between trend lines except for the porous disc case operates in the lower ambient turbulence intensity levels (outside the boundary layer). Furthermore, the wake turbulence intensity distribution of the porous disc case outside the boundary layer is different than that of the other cases in the far-wake region. Nevertheless, one can observe that the estimated wake half width and added turbulence intensity values of both models are comparable after $x/D=5$.

- The wake growth rate and the initial wake width estimations show that the wake growth rate increases as the positions within the boundary layer decrease. Moreover, it is evident that the ambient turbulence intensity effect is more pronounced on the initial wake width for the porous disc compared to the model wind turbine. Calculations further show that the wake growth rate of the model wind turbine operating at low ambient turbulence intensity is similar to that of the porous disc operating at the higher ambient turbulence intensity.

- Both vertical and streamwise components of POD modes become more comparable as both models immerse within the boundary layer both in the near-wake and the far-wake region.

To have deeper insight into the effects of ambient turbulence intensity level on wake development charateristics of both wind turbine and porous disc, it would be educatory to do experiments with various inflow conditions with different passive turbulence grids or active grid which results different inflow turbulence intensity levels and integral length scales at the model location. Moreover, it would be interesting to perform PIV measurements along the horizontal plane of the models.

REFERENCES

[1]   D. Henner and REN21, "Ren21," 2017. [Online]. Available: https://abdn.pure.elsevier.com/en/en/researchoutput/ren21(5d1212f6-d863-45f7-8979-5f68a61e380e).html

[2]   J. Lee and F. Zhao, "GWEC Global Wind Report," *Glob. Wind Energy Counc.*, p. 75, 2022.

[3]   R. J. Barthelmie, M. S. Courtney, J. Højstrup, and S. E. Larsen, "Meteorological aspects of offshore wind energy: Observations from the Vindeby wind farm," *J. Wind Eng. Ind. Aerodyn.*, vol. 62, no. 2–3, pp. 191–211, 1996, doi: 10.1016/S0167-6105(96)00077-3.

[4]   R. Barthelmie *et al.*, "Ten years of meteorological measurements for offshore wind farms," *J. Sol. Energy Eng. Trans. ASME*, vol. 127, no. 2, pp. 170–176, 2005, doi: 10.1115/1.1850489.

[5]   R. J. Barthelmie *et al.*, "Comparison of wake model simulations with offshore wind turbine wake profiles measured by sodar," *J. Atmos. Ocean. Technol.*, vol. 23, no. 7, pp. 888–901, 2006, doi: 10.1175/JTECH1886.1.

[6]   N. Zhou, J. Chen, D. E. Adams, and S. Fleeter, "Influence of inflow conditions on turbine loading and wake structures predicted by large eddy simulations using exact geometry," *Wind Energy*, vol. 19, no. 5, pp. 803–824, May 2016, doi: 10.1002/we.1866.

[7]   K. Thomsen and P. Sørensen, "Fatigue loads for wind turbines operating in wakes," *J. Wind Eng. Ind. Aerodyn.*, vol. 80, no. 1–2, pp. 121–136, 1999, doi: 10.1016/S0167-6105(98)00194-9.

[8]   S. Sarmast, "Numerical study on instability and interaction of wind turbine

wakes," 2013.

[9]   J. N. Sorensen, R. F. Mikkelsen, D. S. Henningson, S. Ivanell, S. Sarmast, and S. J. Andersen, "Simulation of wind turbine wakes using the actuator line technique," *Philos. Trans. R. Soc. A Math. Phys. Eng. Sci.*, vol. 373, no. 2035, 2015, doi: 10.1098/rsta.2014.0071.

[10]   B. Sanderse, "Aerodynamics of wind turbine wakes Literature review," Jan. 2009.

[11]   K. Mikkelsen, "Effect of free stream turbulence on wind turbine performance," NTNU, 2013. doi: http://hdl.handle.net/11250/235085.

[12]   L. J. Vermeer, J. N. Sørensen, and A. Crespo, "Wind turbine wake aerodynamics," *Prog. Aerosp. Sci.*, vol. 39, no. 6–7, pp. 467–510, 2003, doi: 10.1016/S0376-0421(03)00078-2.

[13]   T. Uchida, T. Yoshida, M. Inui, and Y. Taniyama, "Doppler Lidar Investigations of Wind Turbine Near-Wakes and LES Modeling with New Porous Disc Approach," no. i, pp. 1–33, 2021, doi: https://doi.org/10.3390/en14082101.

[14]   L. J. Vermeer, "A review of wind turbine wake research at TUDELFT," *20th 2001 ASME Wind Energy Symp.*, no. c, 2001, doi: 10.2514/6.2001-30.

[15]   L. E. M. Lignarolo, D. Ragni, C. Krishnaswami, Q. Chen, C. J. Simão Ferreira, and G. J. W. van Bussel, "Experimental analysis of the wake of a horizontal-axis wind-turbine model," *Renew. Energy*, vol. 70, pp. 31–46, 2014, doi: 10.1016/j.renene.2014.01.020.

[16]   D. Medici and P. H. Alfredsson, "Measurements on a wind turbine wake: 3D effects and bluff body vortex shedding," *Wind Energy*, vol. 9, no. 3, pp. 219–236, 2006, doi: 10.1002/we.156.

[17]   S. Aubrun, S. Loyer, P. E. Hancock, and P. Hayden, "Wind turbine wake properties: Comparison between a non-rotating simplified wind turbine model

and a rotating model," *J. Wind Eng. Ind. Aerodyn.*, vol. 120, pp. 1–8, 2013, doi: 10.1016/j.jweia.2013.06.007.

[18] L. E. M. Lignarolo, D. Ragni, C. J. Ferreira, and G. J. W. Van Bussel, "Experimental comparison of a wind-turbine and of an actuator-disc near wake," *J. Renew. Sustain. Energy*, vol. 8, no. 2, 2016, doi: 10.1063/1.4941926.

[19] E. H. Camp and R. B. Cal, "Mean kinetic energy transport and event classification in a model wind turbine array versus an array of porous disks: Energy budget and octant analysis," *Phys. Rev. Fluids*, vol. 1, no. 4, 2016, doi: 10.1103/PhysRevFluids.1.044404.

[20] I. Neunaber, "Stochastic investigation of the evolution of small-scale turbulence in the wake of a wind turbine exposed to different inflow conditions," Carl von Ossietzky University of Oldenburg, 2019.

[21] A. Abdulrahim, M. T. Akpolat, A. Hassanein, M. Perçin, and O. Uzol, "Effects of inflow boundary layer on the wake of a radially non-uniform porous disk," *J. Renew. Sustain. Energy*, vol. 13, no. 3, 2021, doi: 10.1063/5.0045404.

[22] S. Aubrun *et al.*, "Round-robin tests of porous disc models," *J. Phys. Conf. Ser.*, vol. 1256, no. 1, 2019, doi: 10.1088/1742-6596/1256/1/012004.

[23] F. Porté-Agel, M. Bastankhah, and S. Shamsoddin, *Wind-Turbine and Wind-Farm Flows: A Review*, vol. 174, no. 1. Springer Netherlands, 2020. doi: 10.1007/s10546-019-00473-0.

[24] F. C. Fuertes, C. D. Markfort, and F. Porté-Agel, "Wind turbine wake characterization with nacelle-mounted wind lidars for analytical wake model validation," *Remote Sens.*, vol. 10, no. 5, pp. 1–18, 2018, doi: 10.3390/rs10050668.

[25] G. V. Iungo, "Experimental characterization of wind turbine wakes: Wind

tunnel tests and wind LiDAR measurements," *J. Wind Eng. Ind. Aerodyn.*, vol. 149, pp. 35–39, 2016, doi: 10.1016/j.jweia.2015.11.009.

[26] L. M. Bardal, L. R. Sætran, and E. Wangsness, *Performance test of a 3MW wind turbine - Effects of shear and turbulence*, vol. 80. Elsevier B.V., 2015. doi: 10.1016/j.egypro.2015.11.410.

[27] M. B. Christiansen and C. B. Hasager, "Wake effects of large offshore wind farms identified from satellite SAR," *Remote Sens. Environ.*, vol. 98, no. 2–3, pp. 251–268, 2005, doi: 10.1016/j.rse.2005.07.009.

[28] C. B. Hasager *et al.*, "Offshore wind resource estimation from satellite SAR wind field maps," *Wind Energy*, vol. 8, no. 4, pp. 403–419, 2005, doi: 10.1002/we.150.

[29] A. M. AbdelSalam and V. Ramalingam, "Wake prediction of horizontal-axis wind turbine using full-rotor modeling," *J. Wind Eng. Ind. Aerodyn.*, vol. 124, pp. 7–19, 2014, doi: 10.1016/j.jweia.2013.11.005.

[30] N. Sedaghatizadeh, M. Arjomandi, R. Kelso, B. Cazzolato, and M. H. Ghayesh, "Modelling of wind turbine wake using large eddy simulation," *Renew. Energy*, vol. 115, pp. 1166–1176, 2018, doi: 10.1016/j.renene.2017.09.017.

[31] P. G. Regodeseves and C. S. Morros, "Unsteady numerical investigation of the full geometry of a horizontal axis wind turbine: Flow through the rotor and wake," *Energy*, vol. 202, p. 117674, 2020, doi: 10.1016/j.energy.2020.117674.

[32] X. Cai, R. Gu, P. Pan, and J. Zhu, "Unsteady aerodynamics simulation of a full-scale horizontal axis wind turbine using CFD methodology," *Energy Convers. Manag.*, vol. 112, pp. 146–156, 2016, doi: 10.1016/j.enconman.2015.12.084.

[33] W. Miao, C. Li, G. Pavesi, J. Yang, and X. Xie, "Investigation of wake

characteristics of a yawed HAWT and its impacts on the inline downstream wind turbine using unsteady CFD," *J. Wind Eng. Ind. Aerodyn.*, vol. 168, no. May, pp. 60–71, 2017, doi: 10.1016/j.jweia.2017.05.002.

[34] J. M. Wilson, C. J. Davis, S. K. Venayagamoorthy, and P. R. Heyliger, "Comparisons of horizontal-axis wind turbine wake interaction models," *J. Sol. Energy Eng. Trans. ASME*, vol. 137, no. 3, pp. 1–8, 2015, doi: 10.1115/1.4028914.

[35] N. Stergiannis, C. Lacor, J. V. Beeck, and R. Donnelly, "CFD modelling approaches against single wind turbine wake measurements using RANS," *J. Phys. Conf. Ser.*, vol. 753, no. 3, 2016, doi: 10.1088/1742-6596/753/3/032062.

[36] D. Mehta, A. H. van Zuijlen, B. Koren, J. G. Holierhoek, and H. Bijl, "Large Eddy Simulation of wind farm aerodynamics: A review," *J. Wind Eng. Ind. Aerodyn.*, vol. 133, pp. 1–17, 2014, doi: 10.1016/j.jweia.2014.07.002.

[37] F. Porté-Agel, Y. T. Wu, H. Lu, and R. J. Conzemius, "Large-eddy simulation of atmospheric boundary layer flow through wind turbines and wind farms," *J. Wind Eng. Ind. Aerodyn.*, vol. 99, no. 4, pp. 154–168, 2011, doi: 10.1016/j.jweia.2011.01.011.

[38] Y. T. Wu and F. Porté-Agel, "Large-Eddy Simulation of Wind-Turbine Wakes: Evaluation of Turbine Parametrisations," *Boundary-Layer Meteorol.*, vol. 138, no. 3, pp. 345–366, 2011, doi: 10.1007/s10546-010-9569-x.

[39] Y. T. Wu and F. Porté-Agel, "Atmospheric turbulence effects on wind-turbine wakes: An LES study," *Energies*, vol. 5, no. 12, pp. 5340–5362, 2012, doi: 10.3390/en5125340.

[40] Y. T. Wu and F. Porté-Agel, "Modeling turbine wakes and power losses within a wind farm using LES: An application to the Horns Rev offshore wind farm," *Renew. Energy*, vol. 75, pp. 945–955, 2015, doi: 10.1016/j.renene.2014.06.019.

[41] M. Abkar and F. Porté-Agel, "Influence of atmospheric stability on wind-turbine wakes: A large-eddy simulation study," *Phys. Fluids*, vol. 27, no. 3, p. 035104, Mar. 2015, doi: 10.1063/1.4913695.

[42] S. Ivanell, J. N. Sørensen, and D. Henningson, "Numerical Computations of Wind Turbine Wakes," *Wind Energy*, pp. 259–263, 2007, doi: 10.1007/978-3-540-33866-6_48.

[43] N. Troldborg, J. N. Sorensen, and R. Mikkelsen, "Numerical simulations of wake characteristics of a wind turbine in uniform inflow," *Wind Energy*, vol. 13, no. 1, pp. 86–99, Jan. 2010, doi: 10.1002/we.345.

[44] N. Troldborg, J. N. Sørensen, R. Mikkelsen, and N. N. Sørensen, "A simple atmospheric boundary layer model applied to large eddy simulations of wind turbine wakes," *Wind Energy*, vol. 17, no. 4, pp. 657–669, Apr. 2014, doi: 10.1002/we.1608.

[45] N. Troldborg, F. Zahle, P.-E. Réthoré, and N. N. Sørensen, "Comparison of wind turbine wake properties in non-sheared inflow predicted by different computational fluid dynamics rotor models," *Wind Energy*, vol. 18, no. 7, pp. 1239–1250, Jul. 2015, doi: 10.1002/we.1757.

[46] D. Cabezón, E. Migoya, and A. Crespo, "Comparison of turbulence models for the computational fluid dynamics simulation of wind turbine wakes in the atmospheric boundary layer," *Wind Energy*, vol. 14, no. 7, pp. 909–921, Oct. 2011, doi: 10.1002/we.516.

[47] M. Calaf, C. Meneveau, and J. Meyers, "Large eddy simulation study of fully developed wind-turbine array boundary layers," *Phys. Fluids*, vol. 22, no. 1, p. 015110, 2010, doi: 10.1063/1.3291077.

[48] C. Sicot, P. Devinant, T. Laverne, S. Loyer, and J. Hureau, "Experimental study of the effect of turbulence on horizontal axis wind turbine aerodynamics," *Wind Energy*, vol. 9, no. 4, pp. 361–370, 2006, doi: 10.1002/we.184.

[49] L. P. Chamorro and F. Porté-Agel, "Effects of Thermal Stability and Incoming Boundary-Layer Flow Characteristics on Wind-Turbine Wakes: A Wind-Tunnel Study," *Boundary-Layer Meteorol.*, vol. 136, no. 3, pp. 515–533, 2010, doi: 10.1007/s10546-010-9512-1.

[50] W. Zhang, C. D. Markfort, and F. Porté-Agel, "Wind-Turbine Wakes in a Convective Boundary Layer: A Wind-Tunnel Study," *Boundary-Layer Meteorol.*, vol. 146, no. 2, pp. 161–179, 2013, doi: 10.1007/s10546-012-9751-4.

[51] L. P. Chamorro, R. E. . Arndt, and F. Sotiropoulos, "Reynolds number dependence of turbulence statistics in the wake of wind turbines," *Wind Energy*, vol. 15, no. 5, pp. 733–742, Jul. 2012, doi: 10.1002/we.501.

[52] R. B. Cal, Z. Wilson, E. Camp, and M. Melius, "A 3×3 wind turbine array under stratified conditions," *50th AIAA Aerosp. Sci. Meet. Incl. New Horizons Forum Aerosp. Expo.*, no. January, pp. 1–8, 2012, doi: 10.2514/6.2012-539.

[53] T. Maeda *et al.*, "Wind tunnel study on wind and turbulence intensity profiles in wind turbine wake," *J. Therm. Sci.*, vol. 20, no. 2, pp. 127–132, 2011, doi: 10.1007/s11630-011-0446-9.

[54] A. Al-Abadi, Y. J. Kim, Ertunç, and A. Delgado, "Turbulence Impact on Wind Turbines: Experimental Investigations on a Wind Turbine Model," *J. Phys. Conf. Ser.*, vol. 753, no. 3, 2016, doi: 10.1088/1742-6596/753/3/032046.

[55] Y. Jin, H. Liu, R. Aggarwal, A. Singh, and L. P. Chamorro, "Effects of freestream turbulence in a model wind turbine wake," *Energies*, vol. 9, no. 10, pp. 1–12, 2016, doi: 10.3390/en9100830.

[56] M. Talavera and F. Shu, "Experimental study of turbulence intensity influence on wind turbine performance and wake recovery in a low-speed wind tunnel," *Renew. Energy*, vol. 109, pp. 363–371, 2017, doi: 10.1016/j.renene.2017.03.034.

[57] P. E. J. Vermeulen, P. J. H. Builtjes, H. M. T. TNO., N. C. O. voor Toegepast-Natuurwetenschappelijk Onderzoek. Hoofdafdeling Maatschappelijke Technologie, and N. C. O. voor Toegepast-Natuurwetenschappelijk. Division of Technology for Society, *Turbulence Measurements in Simulated Wind-turbine Clusters*. Netherlands Organization for Applied Scientific Research, Division of Technology for Society, 1982. [Online]. Available: https://books.google.com.tr/books?id=E9GgHAAACAAJ

[58] S. de J. Helvig, M. K. Vinnes, A. Segalini, N. A. Worth, and R. J. Hearst, "A comparison of lab-scale free rotating wind turbines and actuator disks," *J. Wind Eng. Ind. Aerodyn.*, vol. 209, no. November 2020, p. 104485, 2021, doi: 10.1016/j.jweia.2020.104485.

[59] N. O. Jensen, "A note on wind generator interaction," *Risø-M-2411 Risø Natl. Lab. Roskilde*, pp. 1–16, 1983, [Online]. Available: http://www.risoe.dk/rispubl/VEA/veapdf/ris-m-2411.pdf

[60] I. Katic, J. Højstrup, and N. O. Jensen, "A Simple Model for Cluster Efficiency," in *EWEC'86. Proceedings. Vol. 1*, 1987, pp. 407–410.

[61] S. Frandsen *et al.*, "Analytical modelling of wind speed deficit in large offshore wind farms," *Wind Energy*, vol. 9, no. 1–2, pp. 39–53, 2006, doi: 10.1002/we.189.

[62] G. C. Larsen, "A Simple Wake Calculation Procedure," *Risø-M*, vol. No. 2760, p. 58, 1988, [Online]. Available: http://orbit.dtu.dk/ws/files/55567186/ris_m_2760.pdf

[63] G. C. Larsen, "A simple stationary semi-analytical wake model," *Denmark. Forskningscenter Risoe. Risoe-R*, vol. 1713, no. August, pp. 1–21, 2009.

[64] T. Ishihara and G. W. Qian, "A new Gaussian-based analytical wake model for wind turbines considering ambient turbulence intensities and thrust coefficient effects," *J. Wind Eng. Ind. Aerodyn.*, vol. 177, no. April, pp. 275–292, 2018, doi: 10.1016/j.jweia.2018.04.010.

[65]   M. Bastankhah and F. Porté-Agel, "A new analytical model for wind-turbine wakes," *Renew. Energy*, vol. 70, pp. 116–123, 2014, doi: 10.1016/j.renene.2014.01.002.

[66]   X. Gao, H. Yang, and L. Lu, "Optimization of wind turbine layout position in a wind farm using a newly-developed two-dimensional wake model," *Appl. Energy*, vol. 174, pp. 192–200, 2016, doi: 10.1016/j.apenergy.2016.04.098.

[67]   T. Göçmen, P. Van Der Laan, P. E. Réthoré, A. P. Diaz, G. C. Larsen, and S. Ott, "Wind turbine wake models developed at the technical university of Denmark: A review," *Renew. Sustain. Energy Rev.*, vol. 60, pp. 752–769, 2016, doi: 10.1016/j.rser.2016.01.113.

[68]   M. F. Polster, "Comprehensive comparison of analytical wind turbine wake models with wind tunnel measurements and wake model application on performance modelling of a downstream turbine," no. July, 2017, [Online]. Available: https://brage.bibsys.no/xmlui/bitstream/handle/11250/2454926/17955_FULLTEXT.pdf?sequence=1&isAllowed=y

[69]   S. M. Mohsen and J. C. Larue, "The decay power law in grid-generated turbulence," *J. Fluid Mech.*, vol. 219, pp. 195–214, 1990, doi: 10.1017/S0022112090002919.

[70]   W. K. George, "Asymptotic effect of initial and upstream conditions on turbulence," *J. Fluids Eng. Trans. ASME*, vol. 134, no. 6, pp. 1–27, 2012, doi: 10.1115/1.4006561.

[71]   P. A. Davidson, *Turbulence: An Introduction for Scientists and Engineers*. OUP Oxford, 2004. [Online]. Available: https://books.google.com.tr/books?id=rkOmKzujZB4C

[72]   "Corrsin_s_1942.pdf."

[73]   S. B. Pope, "Turublent Flows." p. 773, 2001.

[74] G. I. Taylor, "Statistical theory of turbulenc," *Proc. R. Soc. London. Ser. A - Math. Phys. Sci.*, vol. 151, no. 873, pp. 421–444, 1935, doi: 10.1098/rspa.1935.0158.

[75] G. Comte-Bellot and S. Corrsin, "The use of a contraction to improve the isotropy of grid-generated turbulence," *J. Fluid Mech.*, vol. 25, no. 4, pp. 657–682, 1966, doi: 10.1017/S0022112066000338.

[76] P. Lavoie, L. Djenidi, and R. A. Antonia, "Effects of initial conditions in decaying turbulence generated by passive grids," *J. Fluid Mech.*, vol. 585, pp. 395–420, 2007, doi: 10.1017/S0022112007006763.

[77] P.-Å. KROGSTAD and P. A. DAVIDSON, "Is grid turbulence Saffman turbulence?," *J. Fluid Mech.*, vol. 642, pp. 373–394, 2010, doi: 10.1017/S0022112009991807.

[78] W. D. Baines and E. G. Peterson, "AN INVESTIGATION OF FLOW THROUGH SCREENS," *Trans. Am. Soc. Mech. Engrs.*, [Online]. Available: https://www.osti.gov/biblio/4401650

[79] B. J. Vickery, "Fluctuating lift and drag on a long cylinder of square cross-section in a smooth and in a turbulent stream," *J. Fluid Mech.*, vol. 25, no. 3, pp. 481–494, 1966, doi: 10.1017/S002211206600020X.

[80] P. E. Roach, "The generation of nearly isotropic turbulence by means of grids," *Int. J. Heat Fluid Flow*, vol. 8, no. 2, pp. 82–92, 1987, doi: 10.1016/0142-727X(87)90001-4.

[81] A. Laneville, "Effects of turbulence on wind induced vibrations of bluff cylinders," University of British Columbia, 1973. doi: http://dx.doi.org/10.14288/1.0101058.

[82] P. W. Bearman and T. Morel, "Effect of free stream turbulence on the flow around bluff bodies," *Prog. Aerosp. Sci.*, vol. 20, no. 2, pp. 97–123, 1983, doi: https://doi.org/10.1016/0376-0421(83)90002-7.

[83] Y. Nakamura, Y. Ohya, and S. Ozono, "The effects of turbulence on bluff-body mean flow," *J. Wind Eng. Ind. Aerodyn.*, vol. 28, no. 1, pp. 251–259, 1988, doi: https://doi.org/10.1016/0167-6105(88)90121-3.

[84] R. W. Stewart, *The Atmospheric Boundary Layer*. World Meteorological Organization, 1979. [Online]. Available: https://books.google.com.tr/books?id=D6cJAQAAIAAJ

[85] J. R. Garratt, *The Atmospheric Boundary Layer*. Cambridge University Press, 1994. [Online]. Available: https://books.google.com.tr/books?id=xeEVtBRApAkC

[86] P. R. Owen and H. K. Zienkiewicz, "The production of uniform shear flow in a wind tunnel," *J. Fluid Mech.*, vol. 2, no. 6, pp. 521–531, 1957, doi: 10.1017/S0022112057000336.

[87] J. C. Phillips, N. H. Thomas, R. J. Perkins, and P. C. H. Miller, "Wind tunnel velocity profiles generated by differentially-spaced flat plates," *J. Wind Eng. Ind. Aerodyn.*, vol. 80, no. 3, pp. 253–262, 1999, doi: https://doi.org/10.1016/S0167-6105(98)00207-4.

[88] J. Counihan, "Further measurements in a simulated atmospheric boundary layer," *Atmos. Environ.*, vol. 4, no. 3, pp. 259–275, 1970, doi: 10.1016/0004-6981(70)90061-2.

[89] J. Counehan, "Wind tunnel determination of the roughness length as a function of the fetch and the roughness density of three-dimensional roughness elements," *Atmos. Environ.*, vol. 5, no. 8, pp. 637–642, 1971, doi: 10.1016/0004-6981(71)90120-X.

[90] J. Counihan, "Simulation of an adiabatic urban boundary layer in a wind tunnel," *Atmos. Environ.*, vol. 7, no. 7, pp. 673–689, 1973, doi: 10.1016/0004-6981(73)90150-9.

[91] N. M. Standen, "A spire array for generating thick turbulent shear layers for

natural wind simulation in wind tunnels."

[92] H. P. A. H. Irwin, "The design of spires for wind simulation," *J. Wind Eng. Ind. Aerodyn.*, vol. 7, no. 3, pp. 361–366, 1981, doi: 10.1016/0167-6105(81)90058-1.

[93] C. Farell and A. K. S. Iyengar, "Experiments on the wind tunnel simulation of atmospheric boundary layers," *J. Wind Eng. Ind. Aerodyn.*, vol. 79, no. 1–2, pp. 11–35, 1999, doi: 10.1016/S0167-6105(98)00117-2.

[94] T. Balendra, D. A. Shah, K. L. Tey, and S. K. Kong, "Evaluation of flow characteristics in the NUS-HDB wind tunnel," *J. Wind Eng. Ind. Aerodyn.*, vol. 90, no. 6, pp. 675–688, 2002, doi: 10.1016/S0167-6105(01)00223-9.

[95] H. W. Teunissen, "Simulation of the planetary boundary layer in a multiple-jet wind tunnel," *Atmos. Environ.*, vol. 9, no. 2, pp. 145–174, 1975, doi: https://doi.org/10.1016/0004-6981(75)90065-7.

[96] S. Cao, A. Nishi, H. Kikugawa, and Y. Matsuda, "Reproduction of wind velocity history in a multiple fan wind tunnel," *J. Wind Eng. Ind. Aerodyn.*, vol. 90, no. 12, pp. 1719–1729, 2002, doi: https://doi.org/10.1016/S0167-6105(02)00282-9.

[97] J.-B. Pang and Z.-X. Lin, "Development and experimental study on the active simulation device in boundary layer wind tunnel," *Shiyan Liuti Lixue/Journal Exp. Fluid Mech.*, vol. 22, pp. 80–85, 2008.

[98] A. Abdulrahim, "EFFECTS OF INFLOW BOUNDARY LAYER ON THE WAKE CHARACTERISTICS OF A RADIALLY NON-UNIFORM POROUS DISC," Middle East Technical University, 2022.

[99] A. Sciacchitano, "Uncertainty quantification in particle image velocimetry," *Meas. Sci. Technol.*, vol. 30, no. 9, 2019, doi: 10.1088/1361-6501/ab1db8.

[100] L. H. Benedict and R. D. Gould, "Towards better uncertainty estimates for turbulence statistics," *Exp. Fluids*, vol. 22, no. 2, pp. 129–136, 1996, doi:

10.1007/s003480050030.

[101] A. Sciacchitano and B. Wieneke, "PIV uncertainty propagation," *Meas. Sci. Technol.*, vol. 27, no. 8, 2016, doi: 10.1088/0957-0233/27/8/084006.

[102] B. Öztürk, A. Hassanein, M. Tuğrul Akpolat, A. Abdulrahim, M. Perçin, and O. Uzol, "Effects of freestream turbulence on the wake growth rate of a model wind turbine and a porous disc," *J. Phys. Conf. Ser.*, vol. 2265, no. 2, p. 022042, 2022, doi: 10.1088/1742-6596/2265/2/022042.

[103] Q. Li, J. Murata, M. Endo, T. Maeda, and Y. Kamada, "Experimental and numerical investigation of the effect of turbulent in fl ow on a Horizontal Axis Wind Turbine (part II : Wake characteristics)," vol. 113, pp. 1304–1315, 2016, doi: 10.1016/j.energy.2016.08.018.

[104] P. B. Johnson, C. Jonsson, S. Achilleos, and I. Eames, "On the spread and decay of wind turbine wakes in ambient turbulence," *J. Phys. Conf. Ser.*, vol. 555, no. 1, 2014, doi: 10.1088/1742-6596/555/1/012055.

[105] A. Niayifar and F. Porté-Agel, "A new analytical model for wind farm power prediction," *J. Phys. Conf. Ser.*, vol. 625, no. 1, 2015, doi: 10.1088/1742-6596/625/1/012039.

[106] N. Hamilton, M. Tutkun, and R. B. Cal, "Wind turbine boundary layer arrays for Cartesian and staggered configurations: Part II, low-dimensional representations via the proper orthogonal decomposition," *Wind Energy*, vol. 18, no. 2, pp. 297–315, 2015, doi: https://doi.org/10.1002/we.1719.

[107] N. Hamilton, M. Tutkun, and R. B. Cal, "Low-order representations of the canonical wind turbine array boundary layer via double proper orthogonal decomposition," *Phys. Fluids*, vol. 28, no. 2, p. 025103, 2016, doi: 10.1063/1.4940659.

[108] M. Bastankhah and F. Porte-Agel, "Wind tunnel study of the wind turbine interaction with a boundary-layer flow: Upwind region, turbine performance,

and wake region," *Phys. Fluids*, vol. 29, no. 6, 2017, doi: 10.1063/1.4984078.

[109] J. L. Lumley, "The structure of inhomogeneous turbulent flows," in "Atmospheric turbulence and radio wave propagation," 1967.

[110] J. L. Lumley, "Coherent Structures in Turbulence," in *Transition and Turbulence*, R. E. MEYER, Ed. Academic Press, 1981, pp. 215–242. doi: https://doi.org/10.1016/B978-0-12-493240-1.50017-X.

[111] L. SIROVICH, "TURBULENCE AND THE DYNAMICS OF COHERENT STRUCTURES PART I: COHERENT STRUCTURES," *Q. Appl. Math.*, vol. 45, no. 3, pp. 561–571, 1987, Accessed: Jun. 30, 2022. [Online]. Available: http://www.jstor.org/stable/43637457

[112] D. Bastine, B. Witha, M. Wächter, and J. Peinke, "POD analysis of a wind turbine wake in a turbulent atmospheric boundary layer," *J. Phys. Conf. Ser.*, vol. 524, no. 1, 2014, doi: 10.1088/1742-6596/524/1/012153.

[113] G. De Cillis, S. Cherubini, O. Semeraro, S. Leonardi, and P. De Palma, "POD-based analysis of a wind turbine wake under the influence of tower and nacelle," *Wind Energy*, vol. 24, no. 6, pp. 609–633, 2021, doi: 10.1002/we.2592.

[114] G. De Cillis, S. Cherubini, O. Semeraro, S. Leonardi, and P. De Palma, "Stability and optimal forcing analysis of a wind turbine wake: Comparison with POD," *Renew. Energy*, vol. 181, pp. 765–785, 2022, doi: 10.1016/j.renene.2021.09.025.

[115] M. Debnath, C. Santoni, S. Leonardi, and G. V. Iungo, "Towards reduced order modelling for predicting the dynamics of coherent vorticity structures within wind turbine wakes," *Philos. Trans. R. Soc. A Math. Phys. Eng. Sci.*, vol. 375, no. 2091, 2017, doi: 10.1098/rsta.2016.0108.

[116] C. VerHulst and C. Meneveau, "Large eddy simulation study of the kinetic energy entrainment by energetic turbulent flow structures in large wind

farms," *Phys. Fluids*, vol. 26, no. 2, 2014, doi: 10.1063/1.4865755.

[117] E. H. Camp and R. B. Cal, "Low-dimensional representations and anisotropy of model rotor versus porous disk wind turbine arrays," *Phys. Rev. Fluids*, vol. 4, no. 2, p. 24610, 2019, doi: 10.1103/PhysRevFluids.4.024610.

[118] L. E. M. Lignarolo, D. Ragni, C. J. SimãO Ferreira, and G. J. W. Van Bussel, "Turbulent mixing in wind turbine and actuator disc wakes: An experimental analysis," *33rd Wind Energy Symp.*, no. January, pp. 1–9, 2015.

[119] L. P. Chamorro and F. Porté-Agel, "A wind-tunnel investigation of wind-turbine wakes: Boundary-Layer turbulence effects," *Boundary-Layer Meteorol.*, vol. 132, no. 1, pp. 129–149, 2009, doi: 10.1007/s10546-009-9380-8.

A. POD Modes of the Second Experiment Campaign
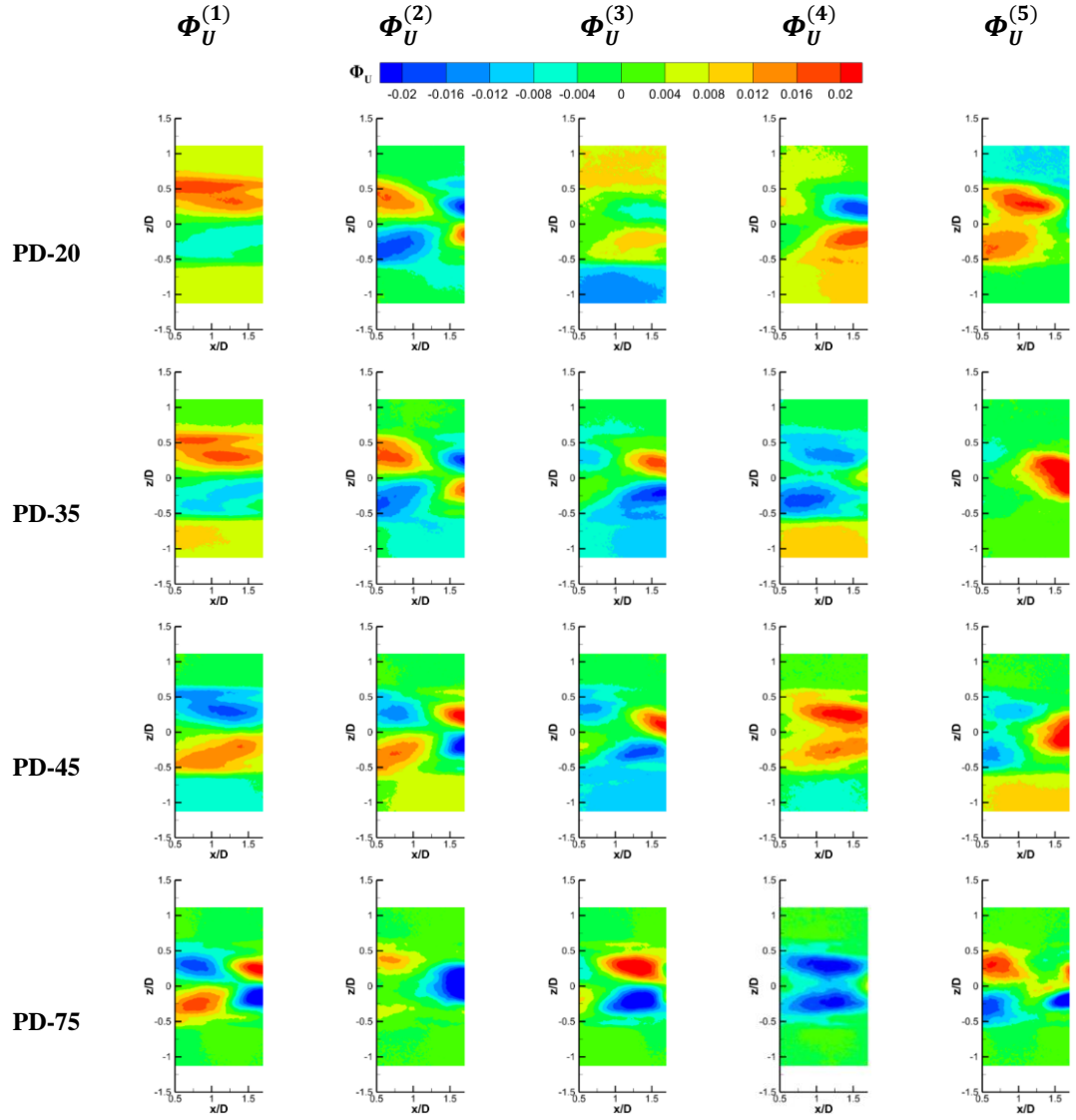
Figure A.1. POD streamwise components (Φ_U) of first 5 modes in the near wake of the porous disc at different boundary layer height positions.
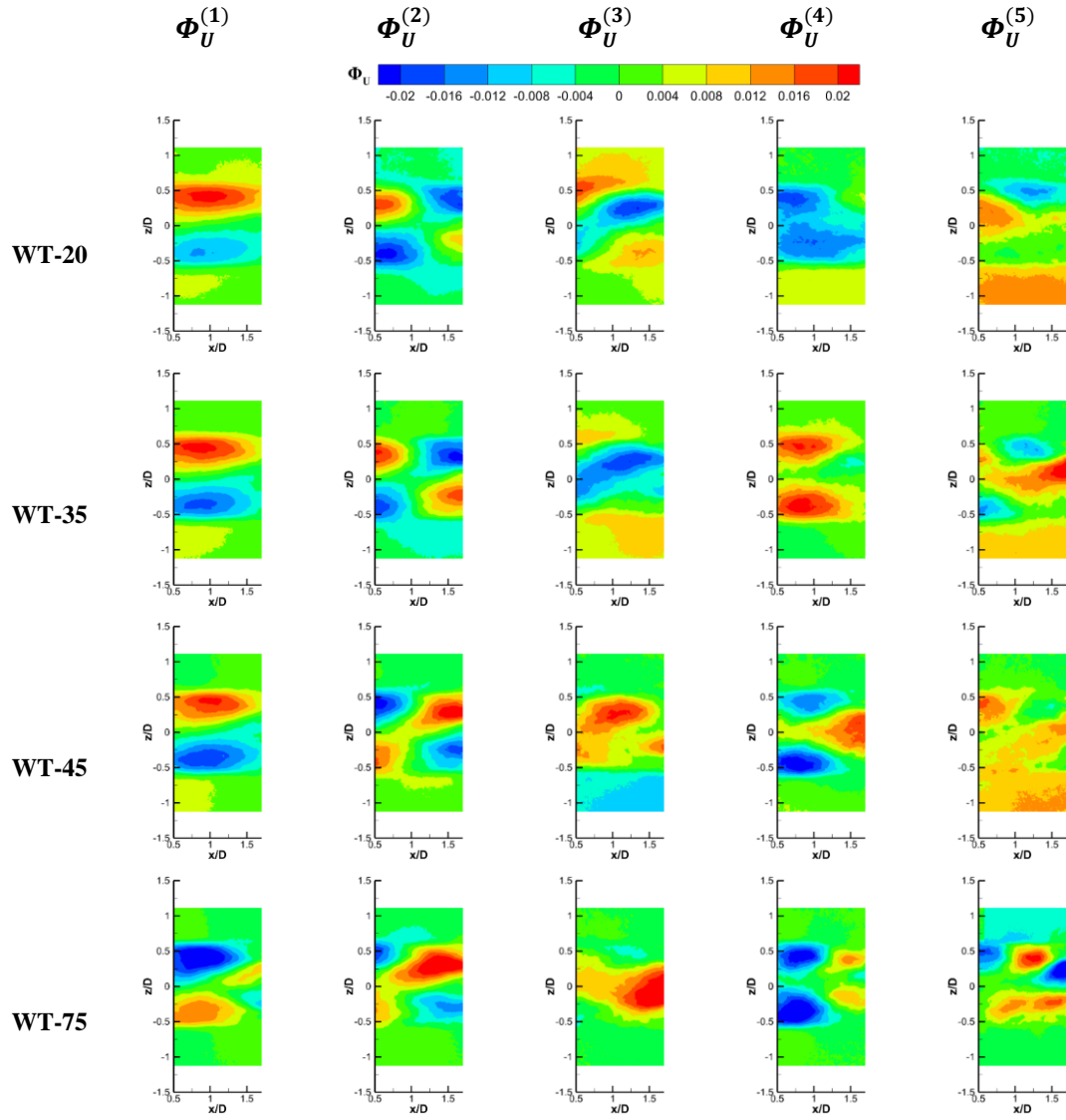
Figure A.2. POD streamwise components (Φ_U) of first 5 modes in the near wake
of the model wind turbine at different boundary layer height positions.
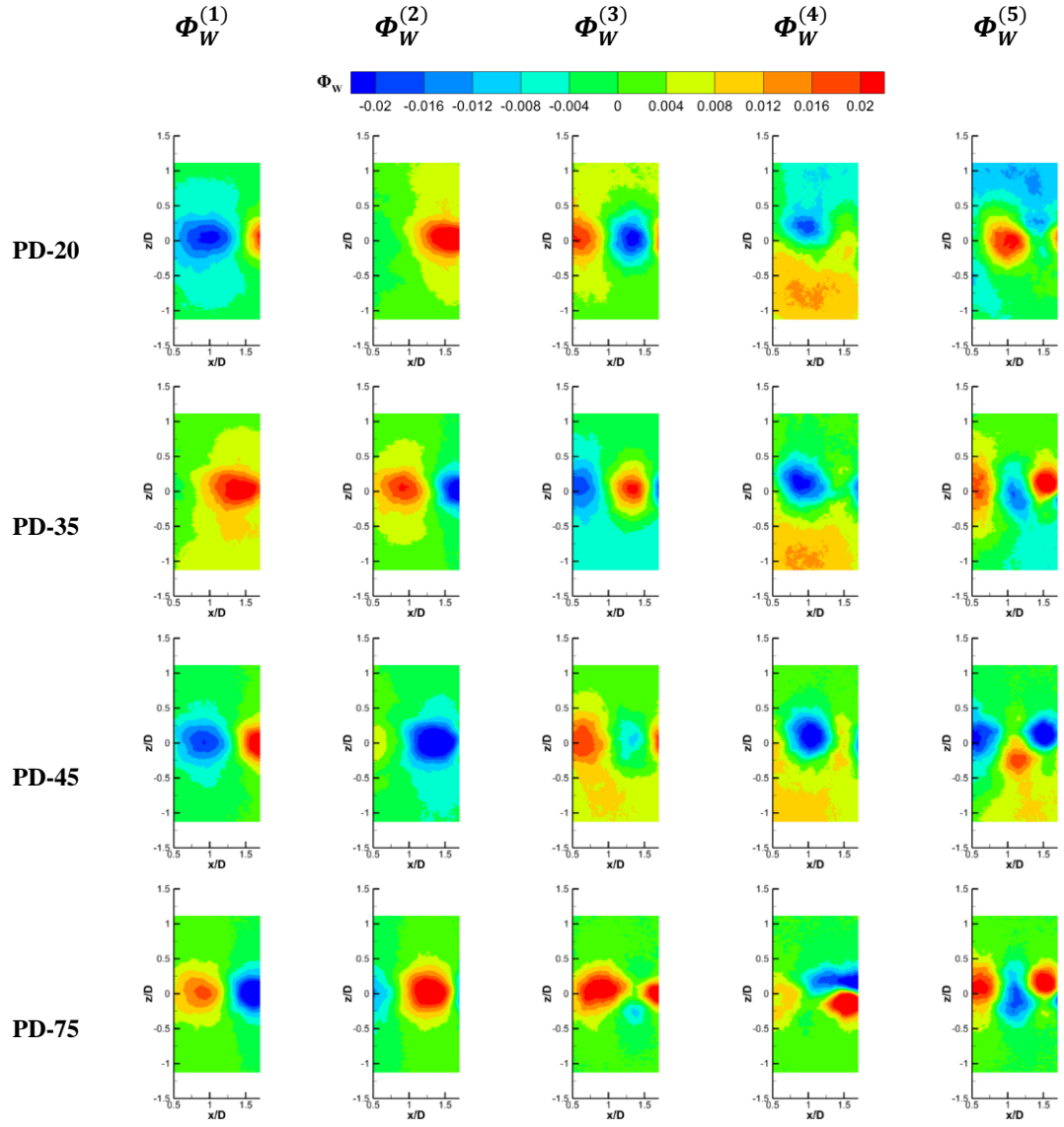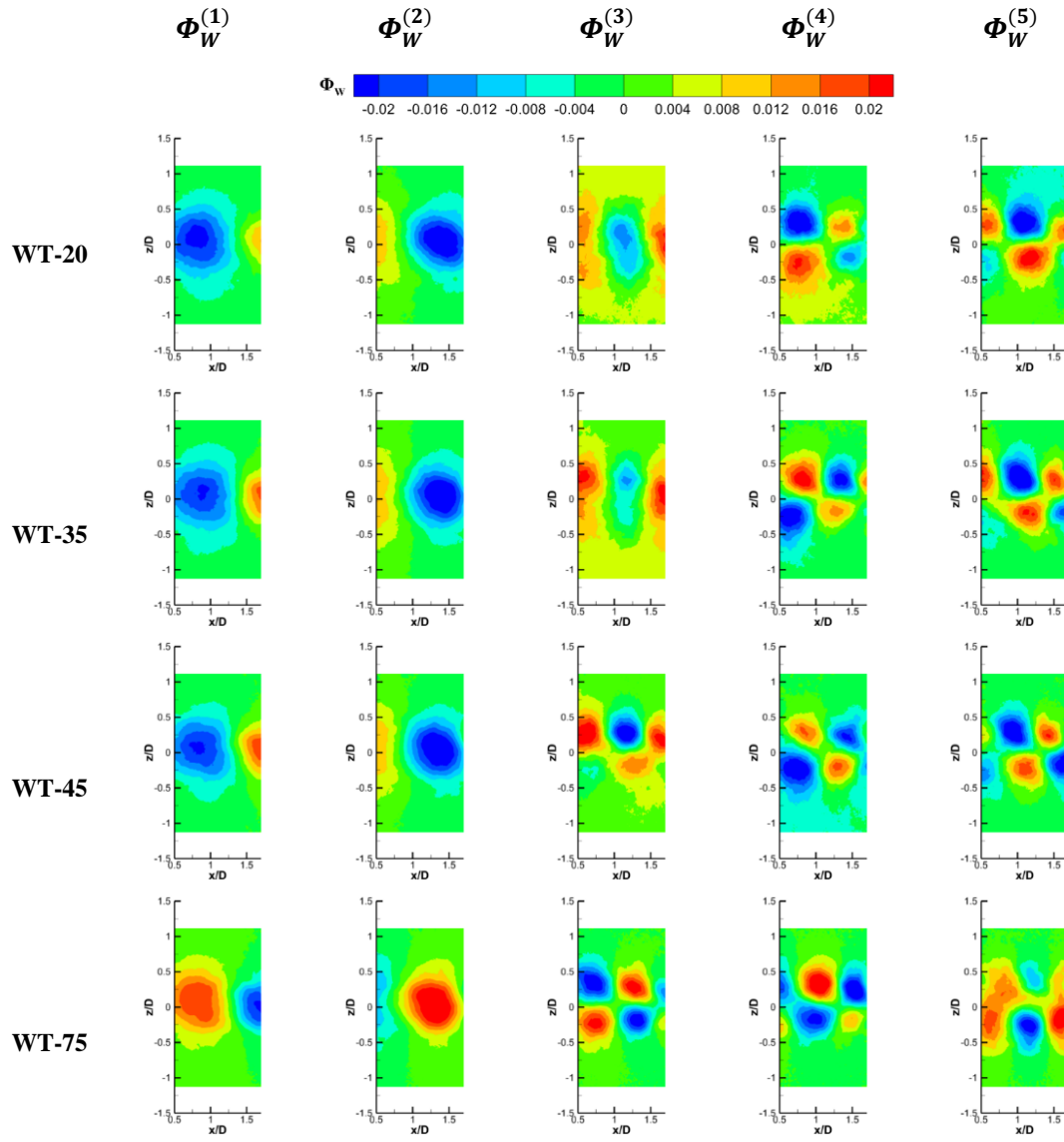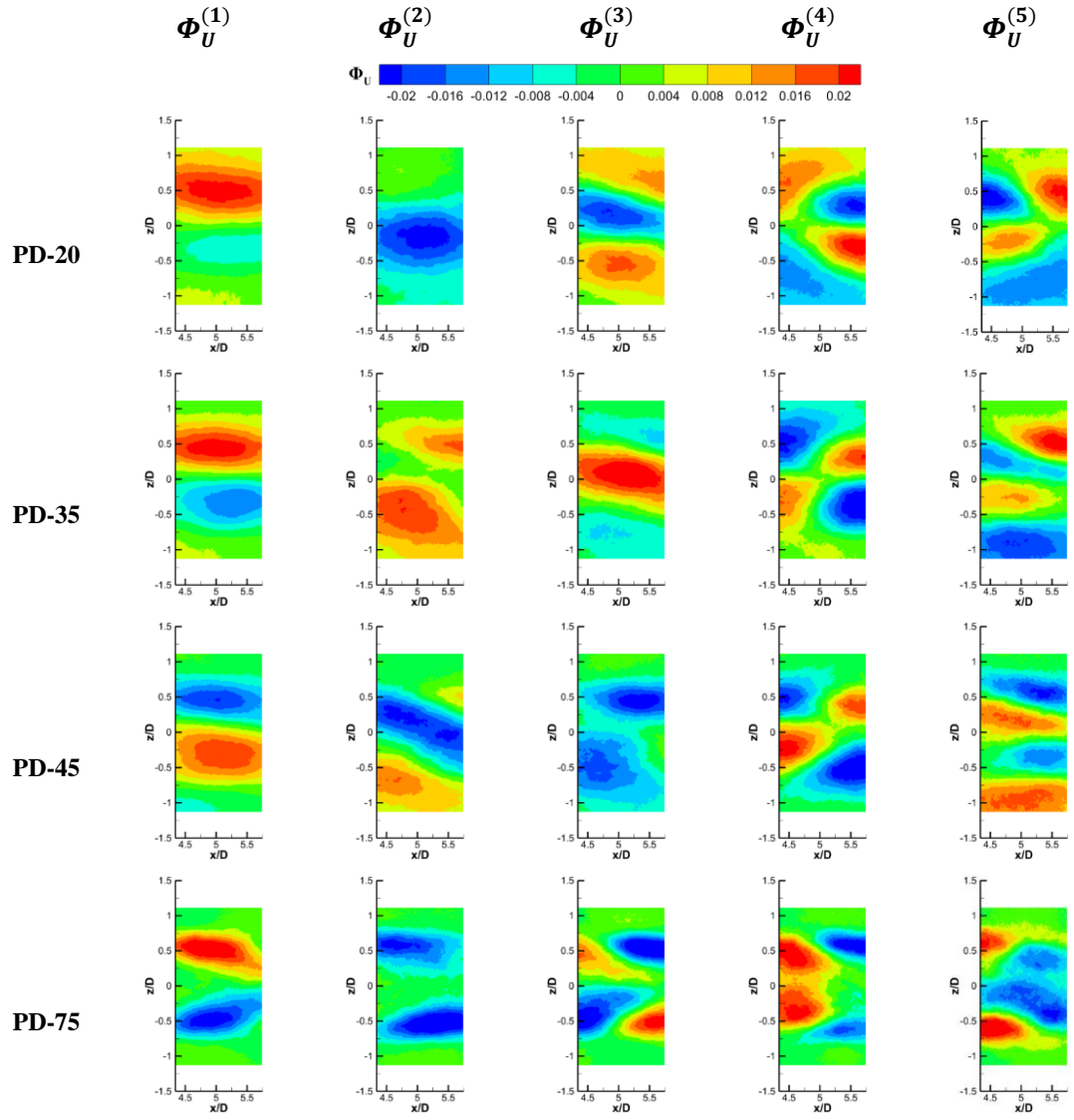
Figure A.3. POD radial components (Φ_V) of first 5 modes in the near wake of the porous disc at different boundary layer height positions.

Figure A.4. POD radial components (Φ_V) of first 5 modes in the near wake of the model wind turbine at different boundary layer height positions.

Figure A.5. POD streamwise components (Φ_U) of first 5 modes in the far wake of the porous disc at different boundary layer height positions.
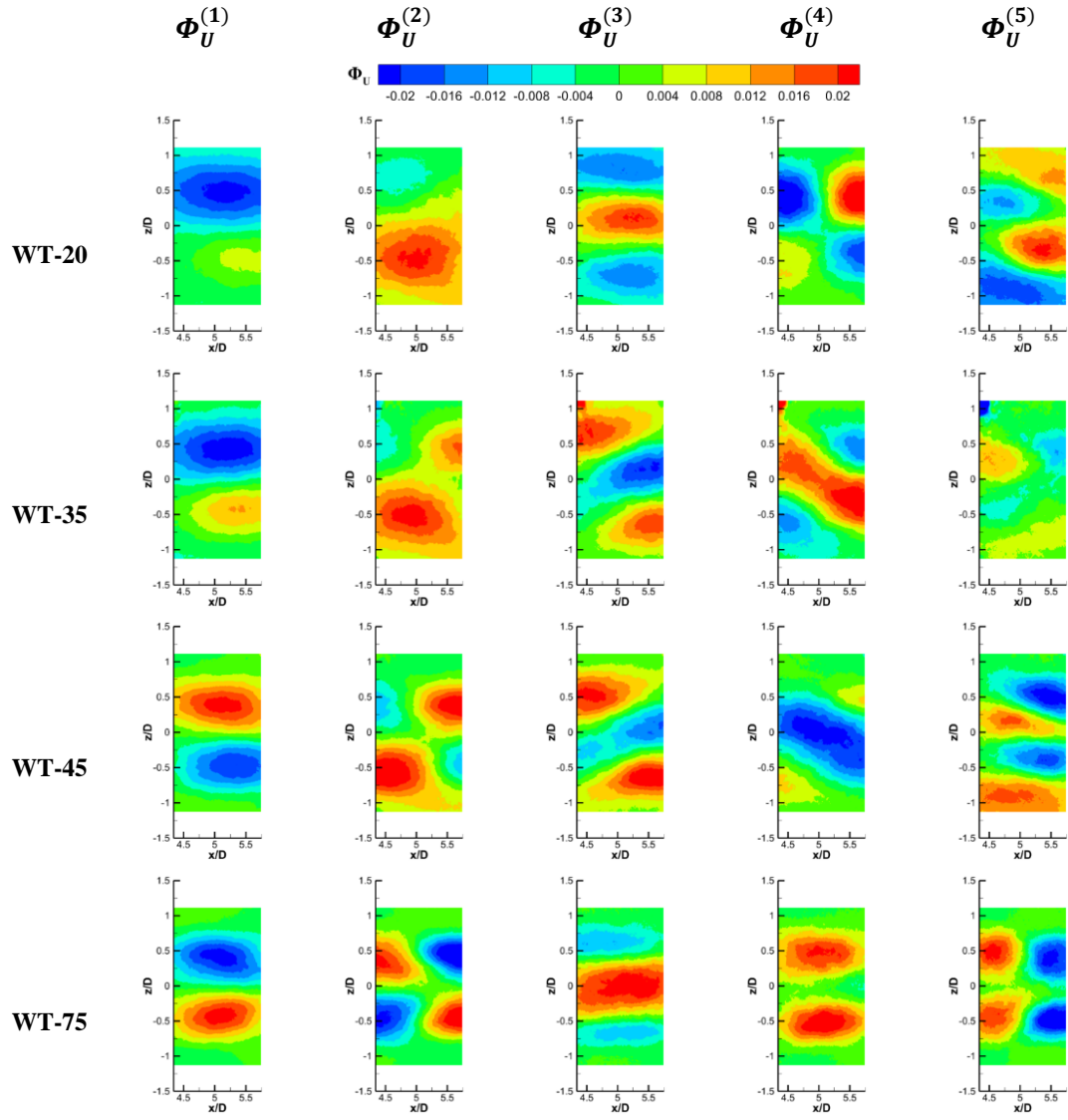
Figure A.6. POD streamwise components (Φ_U) of first 5 modes in the far wake of the model wind turbine at different boundary layer height positions.
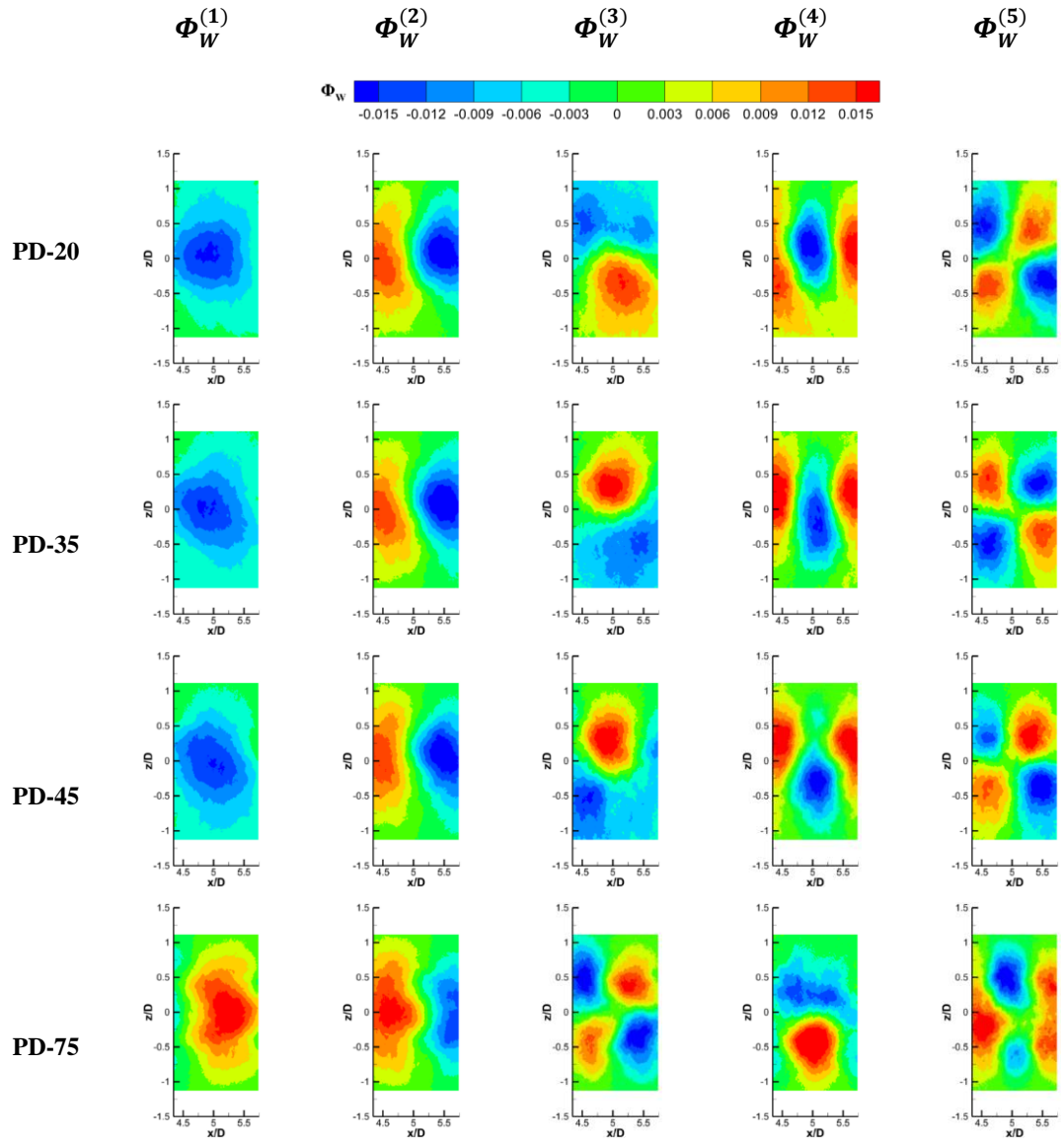
Figure A.7. POD streamwise components (Φ_V) of first 5 modes in the far wake of the porous disc at different boundary layer height positions.
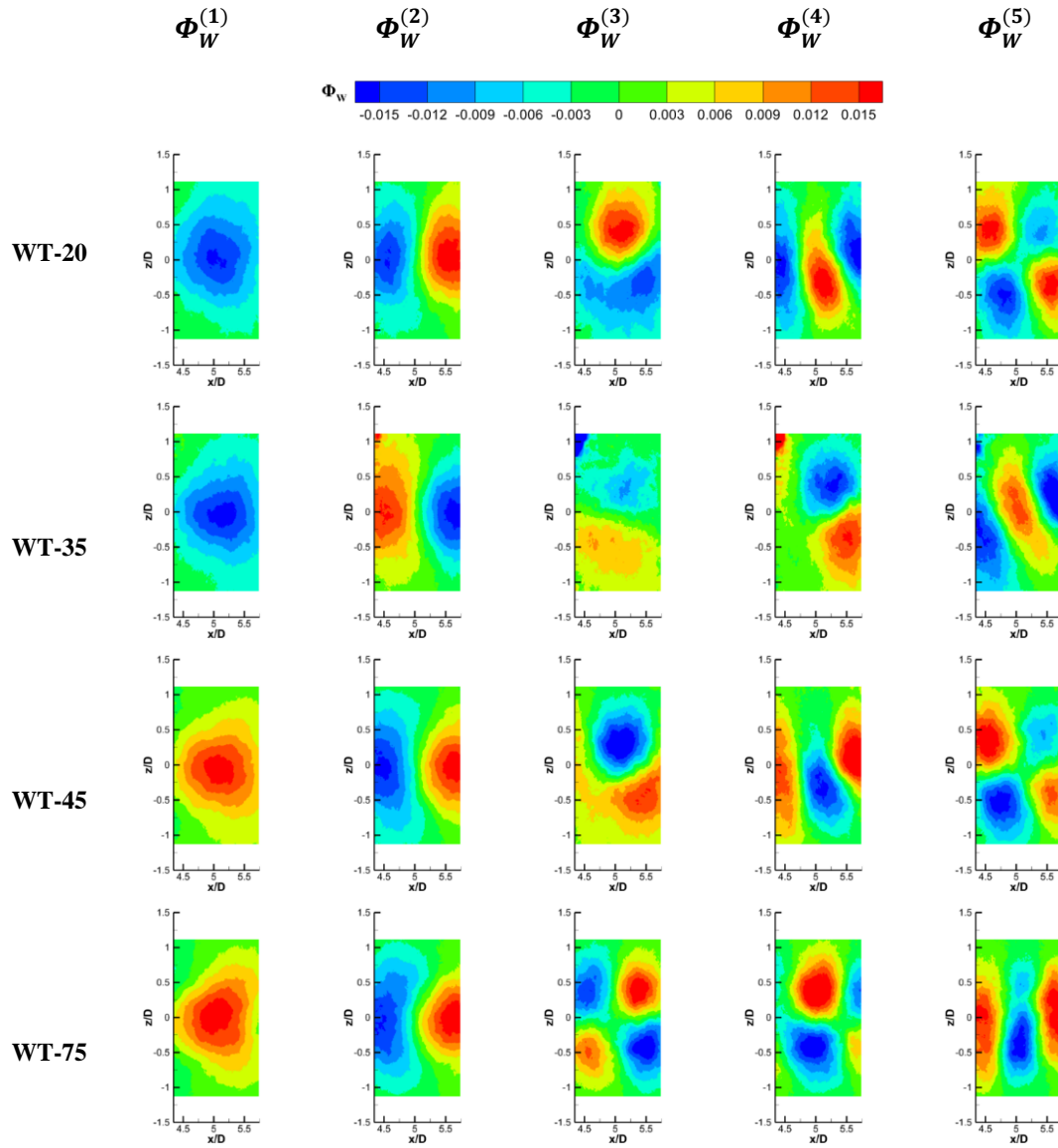
Figure A.8. POD streamwise components (Φ_V) of first 5 modes in the far wake of the model wind turbine at different boundary layer height positions.